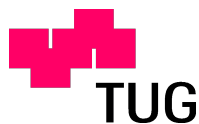# Steady And Unsteady CFD Simulation Of A Two-Stage Turbine With A Turning Mid Turbine Frame

made for the purpose of obtaining the
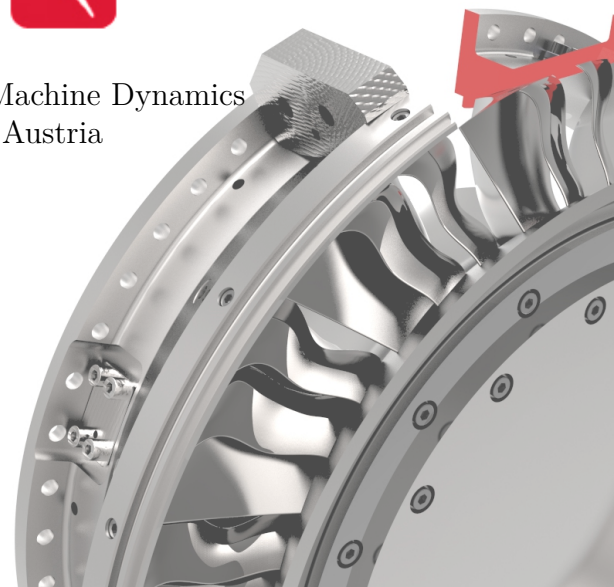academic degree *Diplom Ingenieur* by

Pascal Bader, BSc

under the supervision of
Ao.Univ.-Prof. Dipl.-Ing. Dr.techn. W. Sanz
and Dott.-Mag. R. Spataro

Institute for Thermal Turbomachinery and Machine Dynamics
at Graz University of Technology, Austria

Graz, 2014

Abstract

The modern aviation represents one of the most important means of transportation of the modern society. The comfort of a modern aircraft comes together with some disadvantages: Air pollution, noise emissions and fuel consumption are only the biggest influences on the environment caused by aircrafts. It is vital to reduce theses impacts as well as the energy consumption. Hence it is important to improve the efficiency of jet planes to enable a more sustainable air traffic.

This master thesis analyses the flow through a two-stage counter-rotating turbine operated at the *Institute for Thermal Turbomachinery and Machine Dynamics, Graz University of Technology* for flow research.

From the high pressure stage a duct, so called mid turbine frame (MTF) guides the flow towards the downstream low pressure stage. In this work, a special MTF is analysed, connecting the two stages is equipped with turning struts with additional splitters. This turning mid turbine frame (TMTF) with embedded design replaces the low pressure vane row.

The flow study has been made by a CFD-simulation with two different codes: The commercial code CFX® and Linars, a code developed by the institute. With both programs a steady state simulation and additionally an unsteady calculation have been performed with Linars. The validation and verification has been carried out with a previously performed measurement.

The investigations showed the evolution of the secondary flow structures in the duct and the improvements by the splitters.

Kurzfassung

Die moderne Luftfahrt stellt eine der wichtigsten Transportmöglichkeiten unserer modernen Gesellschaft dar. Der Komfort, der mit diesem Verkehrsmittel einhergeht, hat allerdings auch seine Kehrseiten: Luftverschmutzung, Lärmbelästigung und Kraftstoffverbrauch sind lediglich die größten Nachteile. Es ist überaus wichtig die Einflüsse auf die Umwelt so gering wie möglich zu halten. Daher ist es unerlässlich die Effizienz der Triebwerke und Flugzeuge zu steigern, um einen nachhaltigen Flugverkehr zu ermöglichen.

Diese Masterarbeit analysiert die Strömung durch eine zweistufige, gegenläufige Turbine, welche am *Institut für thermische Turbomaschinen und Maschinendynamik* der *Technischen Universität Graz* zu Forschungszwecken betrieben wird.

Von der Hochdruckturbine führt ein Übergangskanal die Strömung zu der stromabwärtsgelegenen Niederdruckturbine. In dieser Arbeit wird ein spezieller übergangs Kanal behandelt, welcher umlenkende Stützschaufeln mit zusätzlichen Splitter-Schaufeln besitzt. Dieser umlenkende Zwischenkanal ersetzt die Niederdruckleitschaufeln.

Die Strömungsuntersuchungen in dieser Arbeit wurden mit einer CFD-Simulation durchgeführt. Zwei verschiedene Codes wurden dafür verwendet: Der kommerzielle Code CFX® und der institutseigene Code LINARS. Mit beiden Codes wurde eine stationäre Rechnung und mit LINARS zusätzlich eine instationäre Rechnung durchgeführt. Die Ergebnisse der Simulation wurden mit Messdaten verglichen und validiert.

Die Untersuchungen zeigen die Entwicklung der Sekundärströmungen im Kanal und die Verbesserungen durch die Splitter-Schaufeln.

„The important thing is not to stop questioning. Curiosity has its own reason for existing."

- ALBERT EINSTEIN, theoretical physicist

STATUTORY DECLARATION

I declare that I have authored this thesis independently, that I have not used other than the declared sources/resources, and that I have explicitly marked all material which has been quoted either literally or by content from the used sources.

EIDESSTATTLICHE ERKLÄRUNG

Ich erkläre an Eides statt, dass ich die vorliegende Arbeit selbstständig verfasst, andere als die angegebenen Quellen/Hilfsmittel nicht benutzt, und die den benutzten Quellen wörtlich und inhaltlich entnommenen Stellen als solche kenntlich gemacht habe.

Graz, am/at 06. Jan. 2014

_____
Pascal Bader, BSc

Danksagung

Während meines Studiums habe ich viele Vorlesungen besucht, manche interessanter als andere. Diese Lehrveranstaltungen sowie auch die Professoren haben mich geprägt und mein Interesse für gewisse Bereiche geweckt und mich damit in die Richtung gebracht, in der ich mich heute befinde. Deswegen danke ich vor allem **Univ.-Prof. Dr.-Ing. F. Heitmeir** und **Ao.Univ.-Prof. Dipl.-Ing. Dr.techn. W. Sanz**, die mich für thermische Turbomaschinen und CFD-Simulationen begeistern konnten.

Ich danke meinen Betreuern **Ao.Univ.-Prof. Dipl.-Ing. Dr.techn. W. Sanz** und **Dott.-Mag. R. Spataro** für ihre tatkräftige Unterstützung und für den Beistand bei der Erstellung dieser Diplomarbeit.

Ich danke auch unserem Studiendekan **Univ.-Prof. Dr.-Ing. habil. G. Brenn** für die Unterstützung bei der Beantragung meines Individualstudiums. Außerdem will ich sagen, dass er ein kompetenter, hilfsbereiter und professioneller Studiendekan ist, der sich die Anliegen und Bedürfnisse der Studenten anhört und sich für diese einsetzt.

Ich möchte meiner Familie danken für die Unterstützung, die ich während meines Studiums bekommen habe. Allen voran meiner Mutter **Gertrude**, die mich und meinen Bruder jederzeit mental und finanziell unterstützt hat uns weiterzubilden, auch wenn das bedeutet hat, dass sie in Tirol alleine bleibt. Sie hat uns immer den Rücken gestärkt und ohne ihre Hilfe und Opferbereitschaft wäre unser Studium in diesem Maße wohl nicht möglich gewesen. Ich werde ihr ewig dafür dankbar sein!

Auch will ich meiner restlichen Familie danken, dabei vor allem **Inge & Viktor** und **Eva**, denn durch ihre mentale Fürsprache aber auch finanziell Unterstützung konnte ich mein Studium erfolgreich beenden. Auch danke ich meinem Bruder **Kevin** und meinem Cousin **Thomas** für die Unterstützung bei der Erstellung dieser Diplomarbeit.

Ich möchte auch noch meiner Freundin **Caro** danken, die mich immer unterstützt und uns auch während des Auslandssemesters nicht aufgegeben hat. Ich danke ihr dafür, dass sie mein Leben so wunderbar bereichert und dass sie bei all meinen Entscheidungen hinter mir steht. Ich weiß, dass ich mich auf sie verlassen kann und ich werde sie immer lieben.

Zu guter letzt danke ich allen, die mich bei meinem Studium unterstützt haben und meine Studienzeit zu einer so wunderbaren Zeit gemacht haben: meinen Freunden und meinen Mitstudenten, vor allem meinem langjährigen Freund und Mitbewohner **David**.

Graz, am 06. Jan. 2014   **Pascal Bader**

Nomenclature

Symbol		Unit
α	Yaw angle	$^\circ$
Δh	Specific enthalpy difference	$^\mathrm{J}/_\mathrm{kg}$
$\Delta h_{\text{In to Out}}$	Overall specific enthalpy difference through all stages	$^\mathrm{J}/_\mathrm{kg}$
Δp	Pressure change	Pa
Δs	Specific entropy change	$^\mathrm{J}/_{\mathrm{K}\cdot\mathrm{kg}}$
Δu	Change of the specific inner energy	$^\mathrm{J}/_\mathrm{kg}$
δ	Boundary layer thickness	m
δ_1	Displacement thickness	m
$\dot{m}$	Mass flow	$^\mathrm{kg}/_\mathrm{s}$
$\dot{m}_{Air,out}$	Mass flow of air leaving the engine	$^\mathrm{kg}/_\mathrm{s}$
$\dot{m}_{Fuel}$	Fuel mass flow	$^\mathrm{kg}/_\mathrm{s}$
ϵ	Dissipation of the turbulent kinetic energy	$^{\mathrm{m}^2}/_{\mathrm{s}^3}$
η_i	Inner thermal efficiency	-
η_{is}	Isentropic efficiency	-
γ	Intermittency	-
κ	Isentropic exponent	-
Ω	Circumferential spacing between two blades	$^\circ$
ω	Angular velocity	$^\circ/_\mathrm{s}$
ω	Vorticity	-
ψ	Load coefficient	-
ρ	Density	$^\mathrm{kg}/_{\mathrm{m}^3}$
σ	Standard deviation	-
ν_t	Turbulent viscosity	$^\mathrm{kg}/_{\mathrm{s}\cdot\mathrm{m}}$
$\widetilde{\nu}$	Spalart-Allmaras variable	$^\mathrm{kg}/_{\mathrm{s}\cdot\mathrm{m}}$
c_{ax}	Axial velocity	$^\mathrm{m}/_\mathrm{s}$
c_d	Drag coefficient	-
c_m	Meridional component of the velocity	$^\mathrm{m}/_\mathrm{s}$
c_{out}	Jet velocity	$^\mathrm{m}/_\mathrm{s}$
C_P	Non-dimensional static pressure coefficient	-
C_{P_T}	Non-dimensional total pressure coefficient	-

Symbol		Unit
c_{rad}	Radial velocity	$\mathrm{m/s}$
c_{tan}	Tangential velocity	$\mathrm{m/s}$
e_{abs}	Absolute Error	-
e_{rel}	Relative Error	-
F_T	Thrust of the engine	N
H_u	Lower calorific value	$\mathrm{J/kg}$
k	Turbulent kinetic energy	$\mathrm{J/kg}$
l_m	Mixing length	m
Ma	Mach number	-
p	Static pressure	Pa
$\overline{p_i}$	Averaged static pressure, position i	Pa
$\overline{p_{T,i}}$	Averaged total pressure, position i	Pa
p_{stat}	Static pressure	Pa
$p_{stat,out}$	Static pressure, outlet	Pa
P_{TMTF}	Pitch angle between two struts	°
p_{tot}	Total pressure	Pa
r	Resolution	-
T	Temperature	K
T_{is}	Isentropic temperature	K
T_{tot}	Total temperature	K

Abbr.	Meaning
ACI	Airports Council International
ADI	Alternating direction implicit (Method)
AMG	Algebraic multigrid
Ansys	Analysis system
BL	Baseline
BL	Boundary layer
BPF	Blade passing frequency
BPP	Blade passing period
BPR	Bypass ratio
CFD	Computational fluid dynamics
CFX	Computational Fluid DynamiX
DNS	Direct Navier Stokes
DOE	(U.S.) Department of Energy
ED	Embedded design (splitter design)
FAS	Geometric Full-Approximation Storage Multigrid
GUI	Graphical user interface
HP	High pressure
IATA	International air transport association
ICAO	International Civil Aviation Organization
ITTM	Institute for Thermal Turbomachinery and Machine Dynamics
Linars	Linars is not a roe solver
LP	Low pressure
LPV	Low passage vortex
MG	Multigrid
mid	Midspan
ML	Mixing length
PS	Pressure Side
SFC	Specific fuel consumption
SS	Suction side
TEC	Turbine exit casing
TEV	Trailing edge vortex
TKE	Turbulent kinetic energy
TLV	Tip leakage vortex
$(T)MTF$	Turning mid turbine frame
TTTF	Transonic Turbine Test Facility
UPV	Upper passage vortex
VLV	Vane passage vortex

Contents

CHAPTER

Introduction And Motivation

Mobility is the pivotal point of modern society. Not only the current fast economy, but also people need to be flexible and first of all mobile. Today, airplanes represent one of the most important means of transportation and they are also one of the fastest available, while still economically efficient. Nowadays it is possible to travel in every corner of the world within 24 hours (Figure 1.1). Nearly every second a plane departs somewhere on the planet (see ICAO [1]). According to the *Airports Council International (ACI)* [2] 158 passengers travel by plane every second. The *ACI* reported in 2010 more than five billion passengers a year. In addition to the passenger flights, the aviation also transports masses of cargo. All this results in a total fuel consumed by planes of more than one billion litres of kerosine every day, according to the *U.S. Government of Energy (DOE)* [3]. And since the number of planes in service is sill rising, also the total fuel consumption rises. The graph in Figure 1.2 shows this continuous rise of the fuel consumption over the years. According to the *International air transport association (IATA)* [4] this used fuel leads to an CO_2 emission of about 650 million tons of CO_2 per year.

The fuel consumption, the CO_2 emission as well as noise emission are the most important issues in the development of modern airplanes. In this context, Matthew L. Wald [5] (New York Times) wrote

"JET engines are now so reliable that a pilot can go an entire career without seeing one fail. Autopilots are so good that some airlines have set up their cockpits to emit a loud beep every few

minutes, to make sure the crew is still awake. And navigation is so accurate that landings can be timed to the second.

So what's left to worry about in aviation?

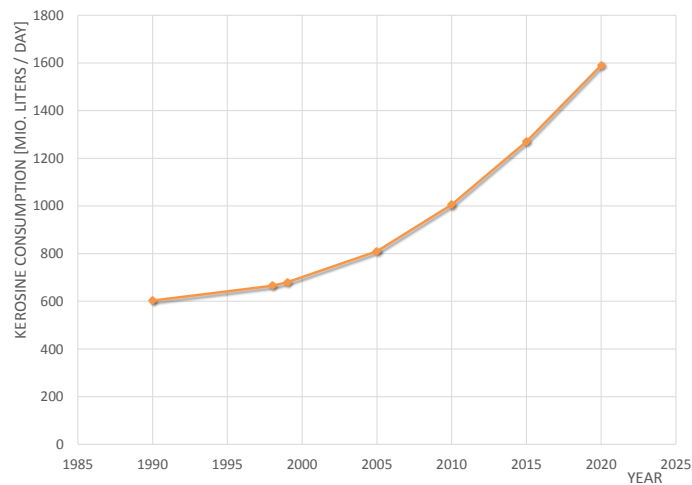*In a word, fuel.* "

Figure 1.1: World's sky ways [6].

Figure 1.2: Development of the kerosine consumption in million litres per day over the years [3].

This article describes, that in order to reduce costs, it is important to increase the efficiency of engines. In the last decades much effort has been

made to develop and improve jet engines. The industrial development of the engines has started with piston engines which were equipped with a propeller. Over the years a need for more and more power to drive the heavier and faster planes has emerged. The wish for higher speed led between 1930 and 1960 [7] to the development of piston engines with up to 4000 HP. With this engines a travelling speed of up to 600 $^{km}/h$ was reachable. But with this power output the limitation for piston engines was reached. To reach even higher aircraft speeds, even more power is required. This high power output can hardly be delivered by piston engines without reaching an excessively high weight of the engine, thus turbomachines were used to power the propeller. Although these turboprop engines would be capable in delivering more power compared to the piston engines, the propeller also reaches its flight-speed-limit at about 600 $^{km}/h$. This circumstance made the turbojet and turbo-fan engines the engines of choice for modern airplanes, although the efficiencies of turboprop engines would be higher. Such turboprop engines are still used in smaller airplanes or heavy cargo planes where a high speed is not the main target. An important value for the evaluation of engines is the ratio [7]

$$\frac{\text{Power output (or Thrust)}}{\text{Weight of the engine}} \tag{1.1}$$

It is the aim of the development of modern engines to reach small ratios. This means that it is necessary to reach a high power output out of low-weight engines. This is the main reason, why piston engines are not powering planes of higher performance classes.

Initially mainly the military industry had the desire to develop and build fast fighter jets, thus the development of jet engines was vital. As already mentioned, the traditional propeller engine is not capable of reaching such high flight speeds. This led to the development of turbo jet engines. An illustration of a turbojet engine is given in Figure 1.4(a). With such engines, high flight speeds are possible, also supersonic speeds (Ma>1). A disadvantage of such engines is the high fuel consumption. This high usage of fuel is not only a problem of cost, it also limits the range. But it is desired to reach far destinations with a non-stop flight. Fan turbo engines can reduce the fuel consumption of the engine compared to jet engines. The reason for this can be explained with the following two equations (simplified formula) [7]:

$$F_T = \dot{m}_{Air} \cdot (c_{in} - c_{out}) \tag{1.2}$$

$$\dot{m}_{Fuel} = \frac{c_{out} \cdot F_T}{\eta_i \cdot H_u} \tag{1.3}$$

In these equations F_T is the thrust of the engine, $\dot{m}_{Air}$ is the mass flow through the engine ($\dot{m}_{Fuel}$ is neglected), c_{in} is the speed of the air flowing into the engine (approximately the flying speed), c_{out} is the jet velocity, $\dot{m}_{Fuel}$ is the fuel mass flow, η_i is the inner thermal efficiency and H_u is the lower calorific value of the burned fuel. Equation (1.2) shows, that there are two options to reach the desired thrust: One is the increase of the air mass flow, the other is the raise of the jet velocity. As Equation (1.3) shows, the burned fuel mass is proportional to the jet velocity. Hence the fuel consumption can be decreased when using a higher mass flow instead of a higher velocity to reach the desired thrust. Fan engines use this method to reach lower fuel consumptions, thus higher ranges with the same amount of fuel.
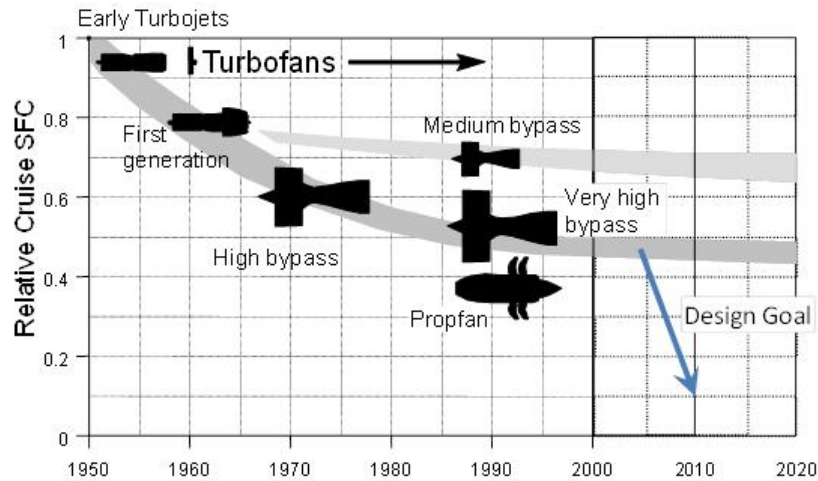
Figure 1.3: Decreasing specific fuel consumption (SFC) over the years with an increasing bypass ratio (BPR) [8].

In Figure 1.3 the evolution of different types of engines is shown over the years. It can be seen, that the bypass ratio increases with the years and the specific fuel consumption drops.

Up to a specific border the efficiency increases with a rising bypass-ratio. The higher the mass flow bypassing the core engine is, the larger the fan has to be. The size of the fan is limited by the maximum allowed tip velocity of the fan. Too high tip velocities would lead to a high stress of the fan blades as well as increasing noise emissions, since the tips of the blades approach supersonic speed. In Figures 1.4(b) and (c) two engines with two different bypass ratios are shown. Both engines have two spools. The advantage of a multi-spool engine concept is the result of the discrepancy

(a) Turbojet engine [9].

(b) Turbofan engine - Bypass ratio 6 [10].

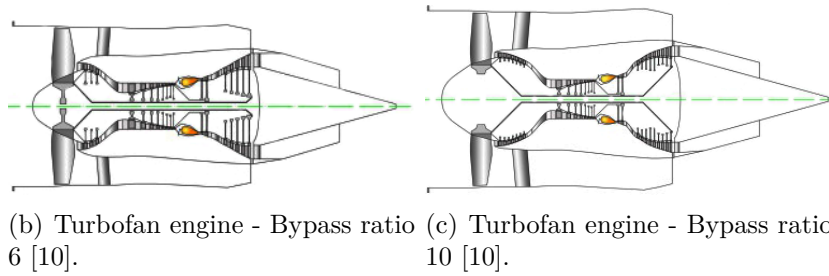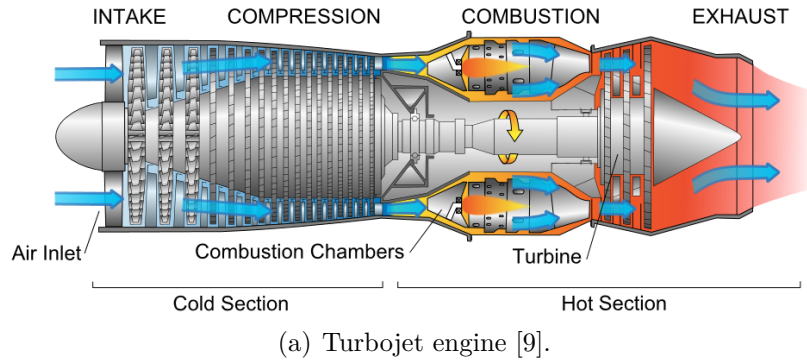(c) Turbofan engine - Bypass ratio 10 [10].

Figure 1.4: Illustration of different turbo-engine types.

of the rotation speed needs of the low and the high pressure spool: On one hand the necessity of a high bypass ratio combined with the limited tip velocity lead to a large, therefore slow rotating fan, thus a slow rotating low pressure spool.

The high pressure rotor should have a high tangential velocity c_{tan}. This can be reached by two ways: One is to increase the radius of the stage, but this would result in a larger, heavier engine. The second possibility is to increase the rotational speed. So the LP stage should have a low rotational speed and on the other hand the high pressure rotor should have a high rotational speed in order to reach a higher pressure rise Δp per stage. This relation can be explained with:

$$\psi = \frac{2 \cdot \Delta h}{c_{tan}^2} \tag{1.4}$$

where ψ represents the load coefficient, Δh the specific enthalpy drop in the stage and c_{tan} the circumferential velocity. If we assume ψ as constant (this assumption is valid, if the blades have geometric similarity), Δh has to increase due to the fact, that the circumferential speed c_{tan} is higher. A higher enthalpy difference per stage results in less stages to reach the same

overall enthalpy difference $\Delta h_{\text{In to Out}}$. This is volitional to reduce weight as well as the overall length of the engine.

The statement above shall be explained with the enthalpy, thus we express Δh with equation [11]:

$$\Delta h = \Delta u + \Delta(p \cdot v) = T \cdot \Delta s - p \cdot \Delta v + v \cdot \Delta p + p \cdot \Delta v \qquad (1.5)$$

$$\Delta h = T \cdot ds + v \cdot dp \qquad (1.6)$$

If Equation (1.6) is inserted into Equation (1.4) and the expansion through the turbine stage is considered as isentropic, equation ψ_{is} (a similar result can be found in [12]) is formulated as:

$$\psi_{is} = \frac{\Delta p}{\frac{\rho}{2} \cdot c_{tan}{}^2} \text{ with } \rho = \frac{1}{v} \qquad (1.7)$$

where Δp is the pressure drop in a turbine stage. This relation shows, that if ψ_{is} is kept constant, the pressure drop per stage is proportional to the square of the tangential velocity: $\Delta p \sim c_{tan}^2$ (Note, that the density ρ is also influenced by the pressure, but this is neglected in this approximation). The higher the rotation speed of the spool is (therefore a higher c_{tan}) the higher Δp. This gives the opportunity to reduce stages to reach the same pressure drop. The possibility to reduce the number of stages offers the possibility to cut down the weight of the engine.

The relation between the specific power and the pressure ratio Π, as well as the relation between the efficiency and the pressure ratio, is plotted in Figure 1.5. The graph shows that for a given peak temperature a higher pressure ratio leads to a higher power output, and in turn to a higher efficiency. At this point it has to be mentioned, that there is a different optimum value in both curves, thus the ideal pressure ratio for the best power output and for the best efficiency, differs.

The above made statements are valid for the turbine as well as for the compressor. To sum up, this means that the HP Compressor/Turbine spool should have a high, while the fan should have a low rotational speed.

Another possibility to reduce weight can be explained with a change of the flow area. Equation (1.8) shows the relation between the flow area A, the mass flow $\dot{m}$ and the meridional, axial velocity $c_{ax,m}$. The velocity triangles are assumed to be similar in this comparison between a one and a three-spool engine. Thus the higher tangential velocity c_{tan} (due to the higher rotation speed) results in a higher axial velocity $c_{ax,m}$ (see Figure 1.6). Because the mass flow is considered as being constant, the flow area A can be reduced, which leads to a smaller engine.

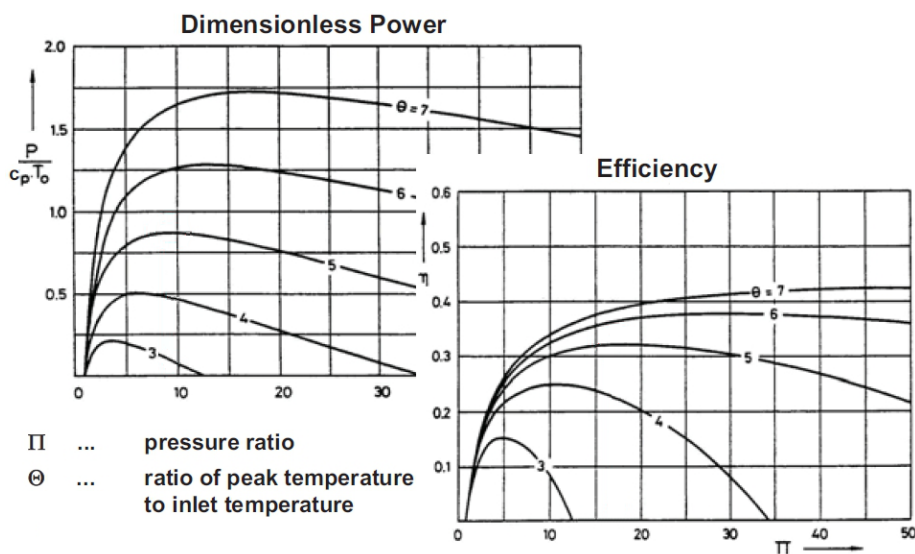$$A = \frac{\dot{m}}{\rho \cdot c_{ax,m}} \qquad (1.8)$$

Figure 1.5: Plots of efficiency η to pressure ratio Π and specific work P to Π [13].

But the change of the speed does not only affect the flow area of the high pressure stages. Obviously the same relations are also valid for the low pressure stage. The variation in the flow area A due to the change of density ρ and velocity $c_{ax,m}$ can be verified with Equation (1.8), since the mass flow $\dot{m}$ stays constant through the stages (except negligible losses through seals and gaps). This change of the area could be managed with a continuously rising of the area from the first high pressure stage towards the low pressure stage. But as said before, the radial dimensions of the engine should be kept as low as possible. The change of the flow section between the HP and LP stages is done with an S-shaped intermediate duct. This connection is called **M**id **T**urbine **F**rame (MTF). There are several different ways to design this frame. For example, the PW6000 aero engine by *Pratt & Whitney* is shown in Figure 1.7(a). This engine has a clean duct, which means, that there is no blade or strut situated within the duct. On the other hand there are engines like the GP7200 by *Engine Alliance*, which is shown in Figure 1.7(b). This engine has a strutted duct. The bearing of the GP7200 is situated in beneath the MTF to reduce axial length and weight. The struts are used to guide the force from the bearing to the engine mount. With this solution, the conventional strut blades at the low pressure exit (the turbine exit casing (TEC)) are not necessary, because the bearing is not situated there anymore (compare for example

7
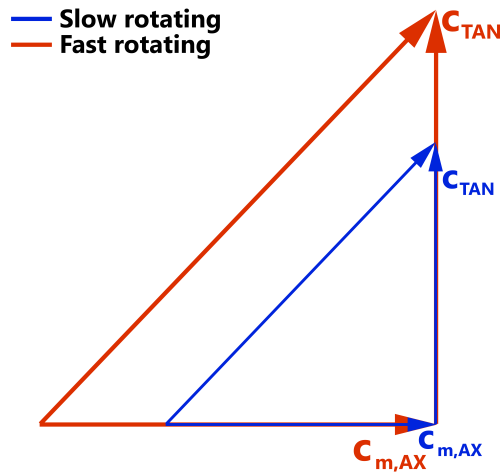
Figure 1.6: Velocity vectors of two similar velocity triangles with different rotational speeds.

(a) Pratt & Whitney PW6000
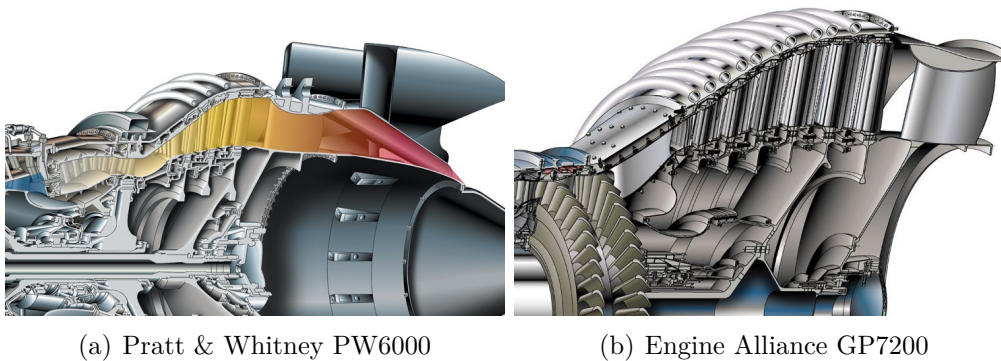
(b) Engine Alliance GP7200

Figure 1.7: The PW6000 with a clean duct and the GP7200 with a strutted duct with different bearing positions [15].

the patent of GE [14]). Hence, the unstressed low pressure housing can be designed much thinner to reduce weight. Further reduction of the weight can be achieved when replacing the low pressure vane blade row behind the duct with aerodynamically optimized strut blades in the MTF. This design is called **T**urning **M**id **T**urbine **F**rame (TMTF), since the strut blades are used as vane blades and guide the flow towards the downstream low pressure rotor. [16]

Main object of this master thesis is the analysis of such a TMTF, but with an embedded design: As mentioned before, the strut blades in a TMTF

are aerodynamically optimized and are used as vane blades. A disadvantage is, that the large spacings between the blades are characterized by large secondary effects like wakes, secondary flows and others. Therefore, split blades are attached in the large spaces between the struts to reduce these secondary effects.

The basic idea of this is to merge the low pressure vane row and the struts in one multi-splitter component. Such a concept was investigated at VKI (e.g. Lavagnoli et al. [17]) and at ITTM. At ITTM Spataro et al. [18, 19] analysed such an embedded design. They performed steady state and unsteady measurements and concluded that the design homogenizes the flow and reduces pressure fluctuations which would effect the subsequent low pressure rotor. [20]

Spataro et al. [19] discussed, analysed and validated the design of such a turbine frame. This frame consists of 16 strut blades with additional 32 zero-incidence split blades, with two split blades between two strut blades. The design was experimental analysed at the **T**ransonic **T**est **T**urbine **F**acility (TTTF) which is situated at the *Institute for Thermal Turbomachinery and Machine Dynamics* (ITTM), *Graz University of Technology*. This rig has a two stage, two-spool turbine in a counter-rotating setup. A CAD illustration of the rig is given in Figure 1.8. More detailed information of the setup and the specification of the operation can be found in references [21–23].

The design of the splitter blades should not only decrease the secondary effects of the mid turbine frame itself, but it should also effect the oncoming vortices. These vortices are coming from the upstream HP stage, transported, even enhanced by the MTF and passed towards the downstream LP stage. It has been analysed in [24], that the vortices are not decaying like in a co-rotating HP-LP stage setup. Therefore the splitter blades should decrease secondary vortices and thus homogenize the flow, so that the following low pressure turbine does have an uniform oncoming flow, reducing the rotor-rotor interaction. To reach these goals, the splitters have been designed very complex, which results in a three dimensional design. The strut with the splitters can be seen in Figure 1.9.

To understand the flow in the mentioned design it is vital to analyse the effects triggered by the endwalls as well as by the blades. Fundamental work has been done by Dominy et al. [25] about the secondary flows in such swan neck diffusers. Many different studies have been performed on mid turbine frames with non-lifting strut blades, for example Norris et al. [26], Wallin et al. [27] or Arroyo Osso et al. [28] performed experimental and/or numerical investigations. A study on different TMTF designs has been done by Santner et al. [29]. Researches have been performed about the flow
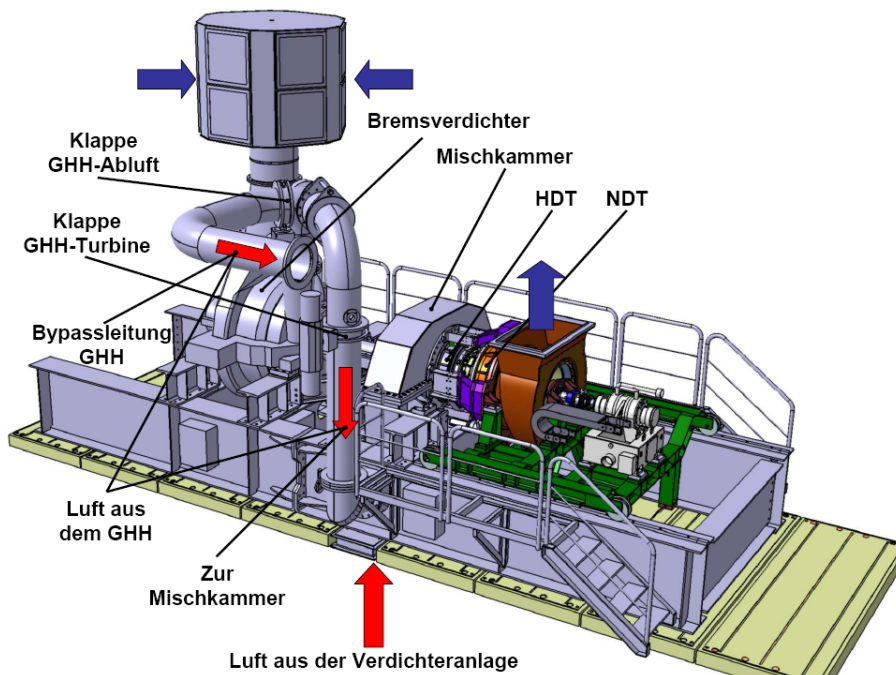
Figure 1.8: The Transonic Turbine Test Facility at the ITTM, Graz.

through the MTF, as example by Pullan et al. [30, 31], Marn et al. [32] or Miller et al. [33]. Studies about the effect of endwall contouring have been made by Harvey et al. [34] or Wallin and Ericsson [35].

All these studies have been performed without a downstream LP stage. Intensive experimental work on the flow in a TMTF was performed at the ITTM in the two-spool, two-stage counter-rotating Transonic Test Turbine Facility. This facility is unique, because it allows to analyse the low and high pressure stage together in one rig. In the frame of the DREAM project Santner et al. [29] investigated the flow on the one hand for a three-dimensionally designed strut blade in an axis-symmetric channel and on the other hand for straight strut blades and contoured endwalls. Wallin et al. [36] performed a numerical CFD study about the TTTF. The operating conditions together with the blade setup of this unique test bench are listed in Table 1.1. In Figure 1.11 a meridional cross-section of the two stages is given. In this illustration also the measurement planes A to F are shown.

State of the art engines are equipped with non-lifting strut blades with subsequent low pressure vane blades. The design of the TMTF with the split blades of the ITTM is replacing the low pressure vane blades, and therefore decreasing the overall length and the weight of an engine. An upstream view

10
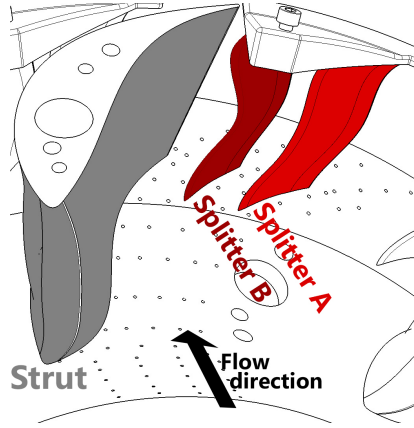
Figure 1.9: The design of strut blades with splitters [19].

of the TMTF can be seen in Figure 1.10. Additional information about the design consideration can be found in [19].

Summing up this section of the work, it is indispensable to reach a more sustainable and efficient air traffic. Therefore it is important to increase the efficiency of engines while reducing the weight of the whole jet. To do so, it is necessary to analyse every part of the engine and to optimize it to reach the best result. As written before, the secondary effects are transported through the MTF from the HP to the LP stage, hence it is vital to analyse this part of the engine. These rotor-rotor interactions are even bigger with reduced length of the MTF, but to reduce weight, this size reduction is volitional in modern jet engines [19].

Table 1.1: Blading parameters and operating conditions [20, 24].

Blading parameters				
	HP vane	HP blade	TMTF	LP blade
Vane/ blade no.	24	36	16	72
h/c_{ax}	1.15	1.37	0.53	2.94
Re(10^{-6})	2.38	1.1	1.86	0.46
Tip gap	-	unshrouded	-	shrouded
Operating conditions				
		HP stage		LP stage
$n_{r,in}$ $[rpm/\sqrt{K}]$		524.4		195.3
$m_{r,in}$ $[kg/s \cdot \sqrt{K}/(bar)]$		81.2		214.6
Stage p_t ratio		3		1.3
Power [kW]		1710		340
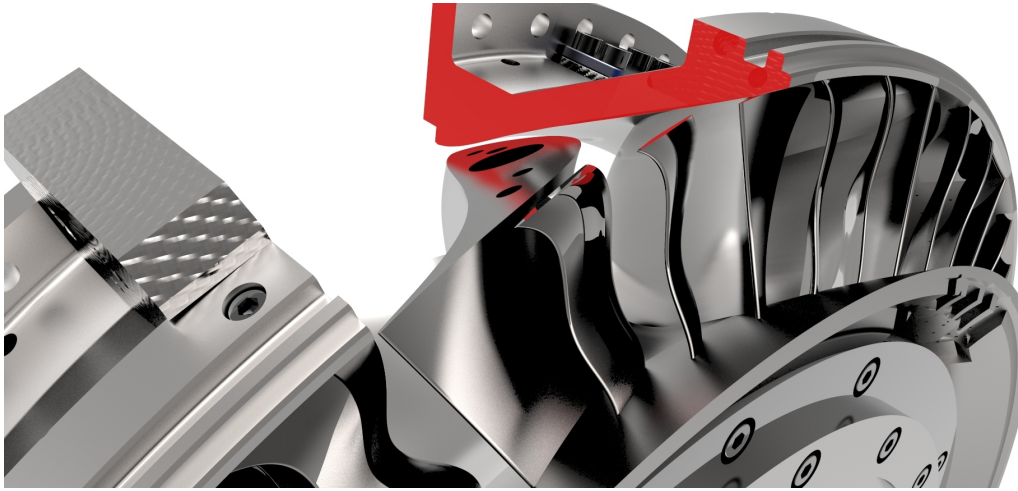
Figure 1.10: View from downstream on the TMTF installed at the rig.

All this effort should lower the losses, result in an efficiency increase and also in a reduction of the weight, and therefore a decrease in the overall dimensions of future jet engines.

1.1 Approach

The object of this thesis is the simulation and the analysis of a TMTF. One part covers a comparison of the simulation of the embedded design and compares the result with the simulated baseline. The second part is the comparison of the results of two different codes. These codes are: CFX® and LINARS. To validate the results, the simulations are compared to previously performed measurements. The following structure has been chosen for this work:

The first part (Chapter 2) of this thesis should inform the reader about the basic theories and methods used in this work. This section explains some key flow features through a TMTF as well as properties of the simulation setup.

The next chapter (Chapter 3) describes the setup of the simulation. It deals with the mesh design as well as other considerations which have been used for the setup of the CFD simulation.

The following section (Chapter 4.1) discusses the results of the embedded design simulation and compares it to the simulated baseline case (without splitters). Both simulations have been performed with CFX®. The simulation of the baseline has already been discussed by Spataro et al.

in [24]. In addition to that new flow features triggered by the embedded design are discussed.

In Chapter 4.2 the main differences between the two observed codes, CFX® and Linars are presented. These differences are analysed with respect to the measurement data. Additionally comparisons of the influence of several key parameters are covered in this section. Also the unsteady simulation done by Linars is discussed.

The last section (Chapter 5) of this thesis contains the conclusions and a brief summary of the work performed in the course of this thesis.
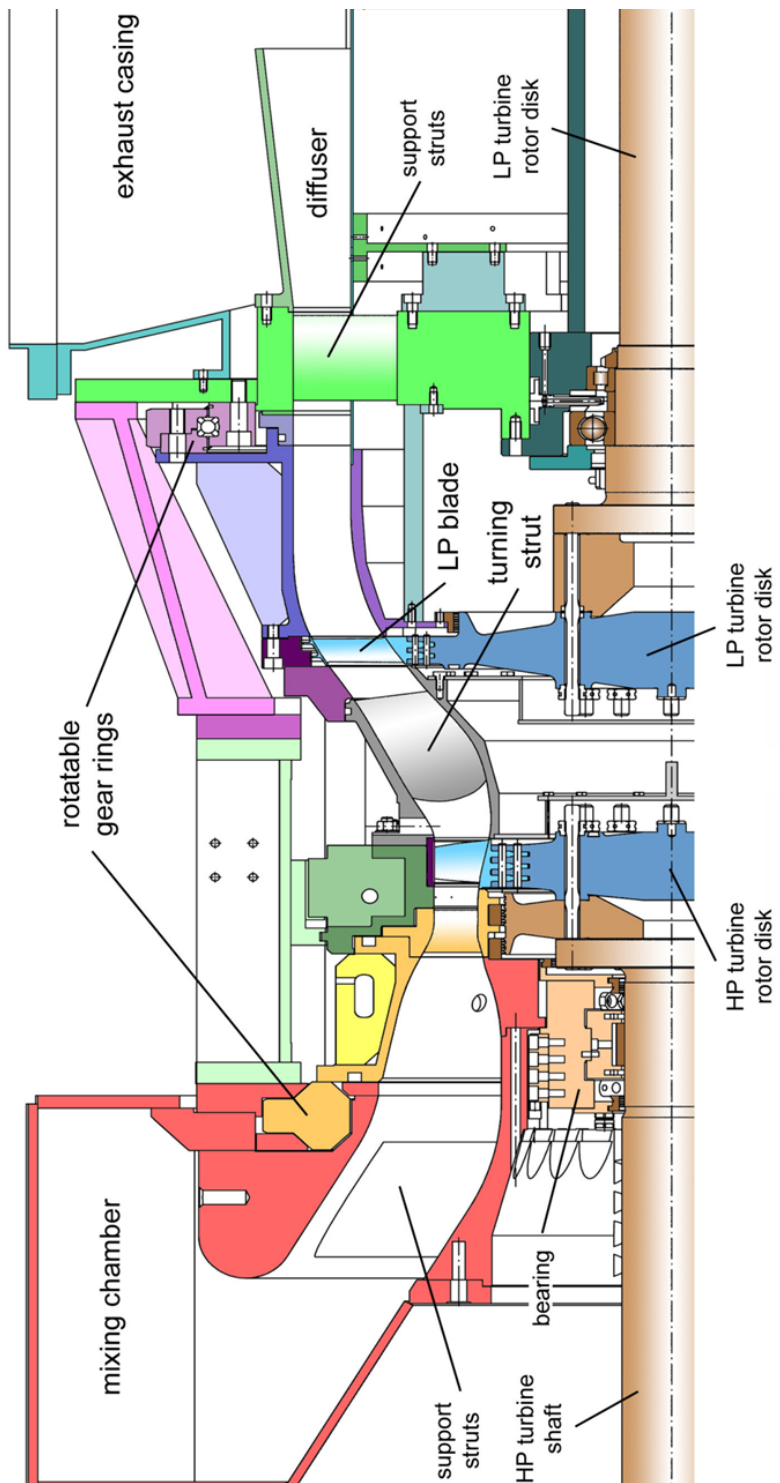
Figure 1.11: Meridional cross-section of the rig at *ITTM*.

CHAPTER 2

Theory And Methods

2.1 What Is And Why CFD?

In this study a *Computational Fluid Dynamics* (CFD)-Simulation has been
carried out. Previous to this work measurement data have been acquired.
However, it is useful to carry out a CFD analysis, since with this procedure
it is possible to get a detailed "look" into the flow field. The measurement
data are taken at specific locations and/or planes and explain the change
from one location to the other, but they do not give an exact explanation
what is really happening between such measurement planes. The behaviour
of the fluid between two planes can be observed with a simulation. To get
a result which is close to the reality the premise is, that the data from the
simulation corresponds with the experimental data.

In the last 40 years the CFD simulation technique has become more
and more popular. This is because it is nearly impossible to get an analytic
result for complex flow problems. Advantages of the simulation in compar-
ison to the experiment are, that the simulation is quite easy to use, quick,
cheap and variant investigations are easy to make simply by changing some
values. [37]

It is interesting that the predecessor of CFD was already devised in
1916 by L.F. Richardson. In his book *Weather Prediction by Numerical
Process* [38] he already talked about the possibility to predict the weather
by solving numerical equations. The amazing thing about his vision was,
that he imagined a kind of factory, he called it the forecast-factory, where
many people were calculating the solutions of the equation. He calculated,
that 64.000 individuals were needed to predict the global weather with a
three hour timestep. The final work was published in 1922 and he called the

human beings which were part of this forecast-factory already computers, about 15 years before the first programmable computer (see Copeland [39]) was invented.

Overall, CFD is a relatively easy tool to get a solution of the pretty difficult fluid mechanic equations. As already mentioned, a CFD simulation also allows to analyse the flow at every possible position, which gives view inside the flow field. With the more and more powerful computers the calculation time is also deceasing rapidly. But it should be kept in mind, that the simulation results are still only approximations to the reality. However, the accuracy of the simulation is very high. The measurement data is always an important evidence of the correctness of the simulation result.

To predict the behaviour of the flow, two different main simulation types can be used: A steady state simulation, where time-averaged values are calculated or an unsteady simulation, where the time-resolved values are computed. In this thesis both types have been applied.

2.2 CFD

Nowadays there are dozens of different CFD codes available. Beside commercial codes (e.g. *Ansys* CFX® and Fluent®, *Flow Science* FLOW-3D®, etc.), there are also OpenSource codes (e.g. OpenFOAM, SU², OpenFlower, etc.) as well as in-house codes programmed by companies for their own use (e.g. *MTU* TRACE, *Siemens* PLM Software CFD, etc.). The differences between the codes lies in their purpose, complexity or user-friendliness. Most of the commercial software packages consist of a solver, a grid generator and a visualization tool. In this thesis two different codes have been used for the simulation:

- *Ansys* CFX® (**C**omputational **F**luid Dynami**X**)
- Linars (**L**inars **is n**ot **a r**oe **s**olver)

The CFX® code is a commercial code distributed by the company *Ansys* (**An**alysis **sys**tems). This code is capable of calculating many different models, like laminar and turbulent flows, heat transfer, rotating and stationary frames, chemical reactions, combustion and much more [40]. For turbulence modelling there are also a big variety of different methods available. For further information see the *Ansys* technical specification [41].

The Linars code on the other hand is an in-house code of the *ITTM*. It has been developed at the institute to make accurate and precise calculations for turbomachinery flows. Linars is a solver without a graphical user

interface (GUI). This code is also capable of different calculation techniques. Some features are [42]

- structured grids in multiblock alignment
- finite volume spatial high order upwind scheme
- fully implicit treatment of the equation system (ADI) with multigrid techniques (FAS)
- various eddy viscosity turbulence models

Like CFX®, Linars has also the possibility to choose between different turbulence models. The entire specification can be found in [42].

Both codes have been used for the steady state simulation performed in this thesis, but only the Linars solver has been used for the unsteady simulation.

Although the two codes solve problems in different ways, the theory behind the calculations is the same. In the following, this theory as well as general methods are reviewed. This part is not a complete discussion about equilibrium rules, balances or differential equations, but a short review, which does not represent all the know-how applied in the course of this work. For more information, however, the reader is encouraged to study additional literature like [43–46].

Turbulence Modelling

In nearly all practical fluid flows, turbulence effects are present. Turbulence is in terms of location and time highly fluctuating. To solve this turbulence, a very fine mesh and very small timesteps are necessary. An option for the solutions is the *Direct Numerical Simulation* (DNS), but this calculation requires substantial calculation time and is practically only applicable for low Reynolds number flows. Therefore modelling methods have been developed to close the time-averaged equation system of a CFD calculation. [47] The closure techniques can be classified as follows [48]:

- **Zero equation or Algebraic eddy viscosity models:** These models use an algebraic form to find the necessary closure terms.
- **One-Equation Models:** Such models use an additional transport equation to find the closure terms.
- **Two and more-equation Models:** These models use additional transport equations to find the closure therms, e.g. equations for the turbulent intensity and dissipation rate.

17

(a) Chart of several closure techniques.

(b) The accuracy of the modelling compared with the computational effort of several methods.
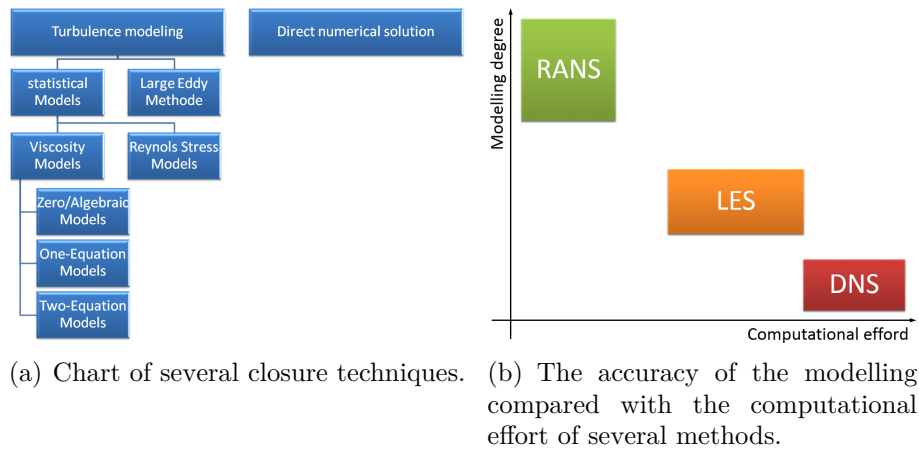
Figure 2.1: Overview of different turbulence modelling methods.

- **Reynolds Stress Models:** These models involve several (usually seven) transport equations to solve the closure problem.

- **Large Eddy Method:** This model applies a low-pass filter on the structures and solves the larger structures directly, while modelling the smaller vortices.

- **Direct Numerical Simulation:** The Navier-Stokes equations are solved instationary. This method does not model the turbulence, it solves the structures directly!

An overview of the described methods can be found in Figure 2.1(a) and a comparison of the computational efforts plotted over the modelling degree in Figure 2.1(b). In this Figure the illustration shows, that the used technique is a compromise between the computational effort (calculation time) and the modeling degree (accuracy). In this thesis a one-equation model (Spalart-Allmaras) and a two-equation model (Shear Stress Transport) have been used.

Spalart-Allmaras Model

One of the models used in this thesis is the *Spalart-Allmaras (SA) model*. The Spalart-Allmaras model is a one-equation model and simulates an additional transport equation for a turbulent viscosity ν_t. SA solves the transport equation for a variable $\widetilde{\nu}$, which matches ν_t except in areas close to a wall. It is a viscosity-like variable, often called Spalart-Allmaras-variable. [46]

18

In this thesis the SA model is only used with LINARS in order to compare the result with the SST model (see Chapter 4.2).

Shear Stress Transport Model
The *Shear Stress Transport (SST) model* is a two-equation eddy viscosity model. There are two groups of two-equation models: The k-ϵ and the k-ω-model, where k represents the turbulent kinetic energy, ϵ the isentropic rate of dissipation and ω the frequency of the energy-dissipation swirl. k-ω has advantages close to the wall while k-ϵ has advantages in the wall-far field. The combination of the advantages of these two two-equation models is the *Menter k-ω-SST model*. This SST formulation has a switch to a k-ϵ behaviour in a free stream, hence it can reduce common k-ω-model problems. A characteristic is, that it generates a bit too much turbulence at flow field, where shear stress is already applied, like in accelerated flows. [43, 44, 47]

In this thesis the SST model by Menter is used with CFX® and LINARS for the steady, as well for the unsteady simulation.

Interfaces

If a domain changes, e.g. rotating to stationary, or liquid to gas, an interface is needed. In the simulation performed in this work, only interfaces between rotating and stationary parts are necessary. There are several methods to manage such a domain change.

Mixing Plane
One possibility to model this domain change is the *Mixing Plane* (or *stage* (CFX)). An alternative is the *frozen rotor* interface.

The mixing plane was introduced by Denton and Singh [49] in 1979 and is a useful interface for a steady state simulation. It circumstantially averages the values of the oncoming and outgoing stream and passes these averaged values to the neighbouring domains. Obviously, it does not transport vortices or other fluctuations directly and it "blurs out" rotor-stator interactions. Still, the mixing plane allows accurate results as well as interpretations of structures transported through the stages. [49]

Frozen Rotor
The *Frozen Rotor* interface is an alternative to the mixing plane. Every particle passes the interface unchanged from one frame to the other. The frame of reference is changed, but the relative position between the stator and the rotor is kept. This model is useful, if there are major circumferen-

tial differences of the values. A disadvantage is, that the transient effects are not modelled. Due to the method of the frozen rotor interface, effects like rotating wakes, secondary flows, etc. will always stay on the same position. This makes the model very dependently on the rotor-stator position of the mesh. This model is often used as an initialization calculation for a following unsteady simulation. [50, 51]

Unsteady sliding-mesh stator-rotor
This interface is for transient simulations only and gives the best result, since it represents a real machine. Every timestep the domain is rotated a small amount $\Delta\omega$ (see Equation (3.8) on page 43) and all values are transported to their neighbouring elements, hence there is no averaging. A disadvantage of the unsteady simulation is, that the computational resources necessary are very high, but it is the best way to represent a real machine. [51]

In real engines there is not always the same number of blades at every stage, mainly to suppress unwanted resonance effects. Hence, to simulate the full rotor-stator interactions, it is necessary to simulate the full wheel. Since this would require high computational resources, this is not easily possible. Therefore it is required to find the smallest common denominator. In the present work, the smallest angle for all stages is 90 degrees.

As an alternative phase-lagged can be often used.

MultiGrid

One main factor of a CFD simulation is the convergence rate. Studies have shown, that the convergence rate is a function of the error field frequency or the gradient of the errors from node to node. The multigrid procedure uses this finding to reach higher convergence rates with the help of coarse grids. Low frequency errors at a fine grid level are high frequency errors at a coarse grid level, hence the convergence rate is higher. This fact accelerates the simulation and reduces the time needed to get a convergent result. [45] The Multigrid method is done in three steps (see Figure 2.2):
Agglomeration: This step produces the coarser grid out of the finer grid.
Restriction: The interpolation method to transport the errors from the fine to the coarse mesh.
Prolongation: This is the inverse Restriction, which means that this step applies the residuals from the coarse to the fine grid level.

There are two classifications: The geometric (FAS) and the algebraic (AMG) multigrid method. The geometric MG is used by Linars.

20
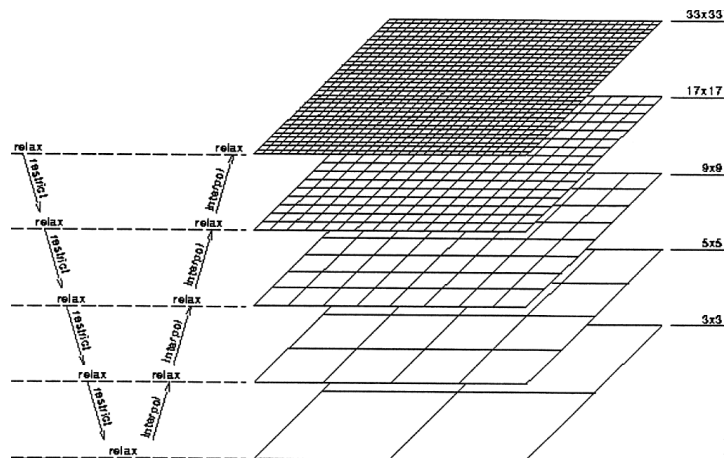
Figure 2.2: Schematic of an V-style multigrid method [45].

Reflection At Boundaries

Boundaries (Inlet, Outlet and Interfaces) have the characteristic that they reflect incoming/outgoing modes (e.g. pressure, velocity, entropy). These reflections result in non-physical behaviour at the boundaries. Therefore it is essential to reduce these errors and have boundaries with far-field qualities. Giles formulated non-reflecting boundary conditions in 1990, which allows to have smaller computational domains, since the boundaries have far-field qualities although they are close to the analysed structure. [52]

Mixing Length Model

The mixing length model describes a method to explain the transfer of momentum by the Reynolds shear stress. After a defined length, the original momentum is dissipated. In other words: A particle, which has defined characteristics will keep these characteristics a specified distance (the mixing length l_m) before dispersing them towards the surrounding medium. In Figure 2.3 this idea is illustrated. The top bar is the mixing length. The particle has its "yellow" characteristics. When passing through the border towards the rear part of the channel it keeps its characteristics until changing to the "blue" characteristics when reaching the mixing length. At this point, the original characteristics have been completely dispersed to the surrounding medium. The model was developed by Ludwig Prantl. [53]

21
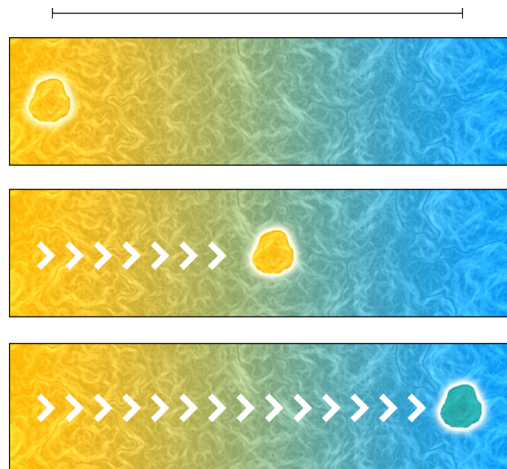
Figure 2.3: A schematic illustration of the mixing length model. [53]

Transition

When a free stream approaches a wall a boundary layer is developed. First, this flow is laminar, but if the Reynolds number Re is large enough fluctuations starts along the wall and the flow becomes turbulent. The change from laminar to turbulent is called transition. Further on the boundary layer is fully turbulent except a small layer very close to the wall, called the viscous sub-layer with the buffer zone between the sub-layer and the turbulent layer.

The transition zone is the region between the laminar and turbulent area of the boundary layer. The structure of the boundary layer is illustrated in Figure 2.4.

Codes, which do not calculate the transition of the boundary layer mainly assume the boundary layer as fully turbulent. Thus the BL is not laminar at the beginning of a wall. But why is it important to differ between a laminar and a turbulent boundary layer? Why is it important to simulate the transition behaviour? The differences between a turbulent and a laminar boundary layer lead to a different drag. This relation should be explained with the help of a smooth ball and a golf ball. At lower Reynolds numbers the smooth ball has a laminar boundary layer, while the golf ball has due to its structured surface a turbulent layer. This difference in the BL leads to a different separation point, which can be observed in Figure 2.5(a). In Figure 2.5(b) the drag coefficient c_d is plotted depending on the Re number. In this graph it is observable, that the drag of the golf ball is lower, if the Re number is low, while a higher Re number leads to a
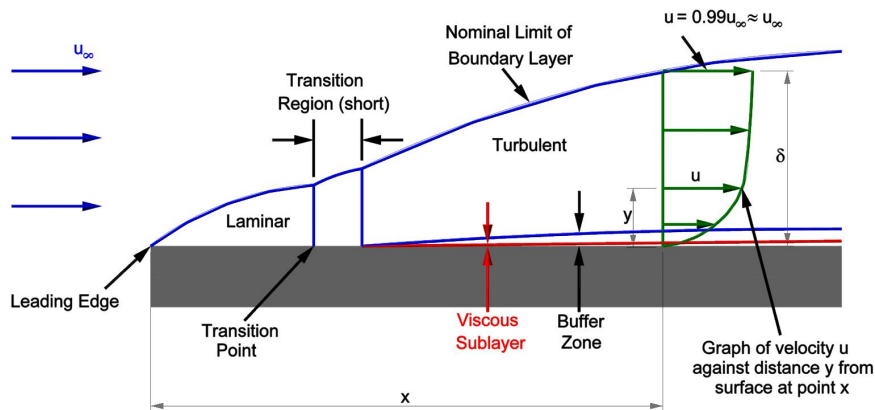
Figure 2.4: The development within the boundary layer [54].
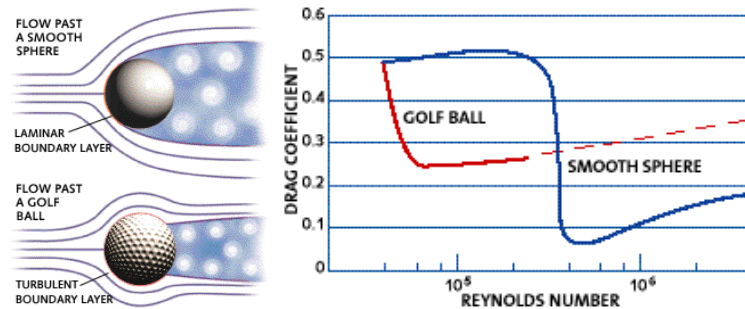
(a) Illustration of the flow field.

(b) Comparison of the drag coefficient at different Reynolds numbers.

Figure 2.5: Comparison of a smooth ball and a golf ball [55].

higher drag. The reason for this is the flow separation at the rear part of the ball. The laminar BL can not follow the contour of the ball as long as the turbulent layer does. Thus, the separation zone behind the ball is larger with the laminar BL and this results in a higher drag. If the *Re* number increases on the other hand, this effect plays a minor role and the higher friction of the turbulent layer leads to the higher drag of the golf ball.

For turbomachines these findings mean, that a laminar BL will separate earlier compared to a turbulent layer. Hence, the turbulent layer is preferred in this case. On the other hand, since the Reynolds numbers in TTM can reach high values, the drag coefficient c_d of a turbulent BL of higher *Re* number is higher due to friction effects, which results in higher losses. The qualitative differences of these two cases can be observed in Figure 2.6. The red line (upper line) in this graph shows the loss coefficient due to

the flow separation, while the blue one (lower line) shows the losses due to friction. It can clearly be seen, that the losses due to friction are lower, if the boundary layer is laminar, while the losses due to a flow separation are higher with a laminar BL.
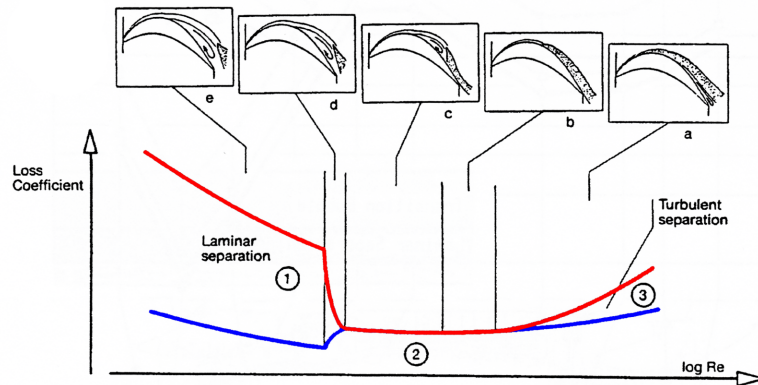
Figure 2.6: Influence of different boundary layers and *Re* numbers on the losses in a turbine cascade [7].

The boundary layer in a turbomachine differs from an ideal layer as shown in Figure 2.4, since the flow in a turbine is effected by [48]:

- strong three-dimensional effects due to curvature, sweep design, rotating blades, etc.
- high free-stream turbulence
- the interaction of different boundary layers (e.g. suction and pressure side BL)
- wakes
- shocks and compressibility effects (at higher Mach numbers)

Lakshminarayana [48] pointed out, that the flow through a turbine stage may laminar, at least up to a specific chord length. This laminar flow may be followed by a laminar separation bubble. Such bubble is illustrated in Figure 2.7. Such bubbles can grow and thus results in increased losses of the turbine stage. Also the bubble can initiate the transition of the boundary layer when reattaching to the blade surface.

All these effects make it difficult to understand the exact behaviour of the boundary layer within a turbo-machine. Therefore it is helpful to perform simulations including the laminar-turbulent transition.
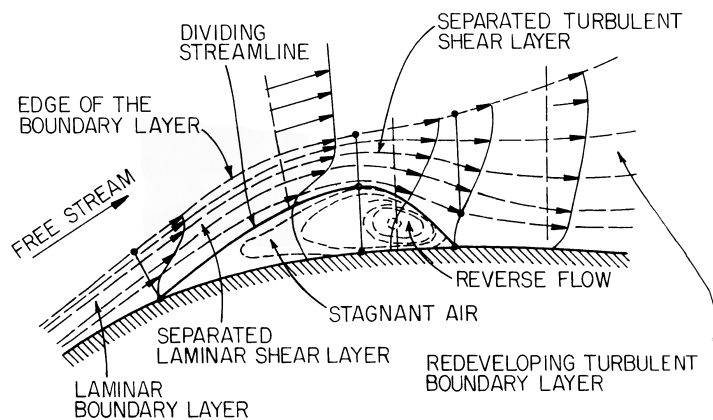
Figure 2.7: The development of a laminar separation bubble [48].
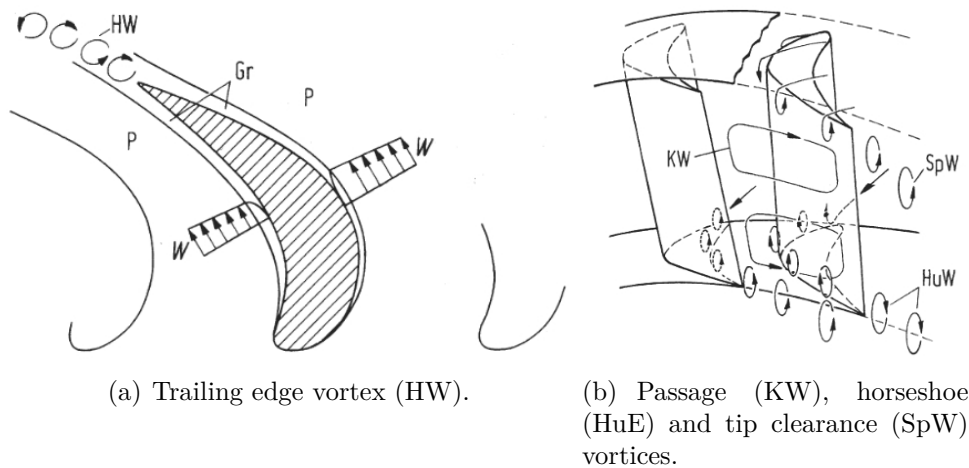
(a) Trailing edge vortex (HW).

(b) Passage (KW), horseshoe (HuE) and tip clearance (SpW) vortices.

Figure 2.8: Schematic illustration of secondary vortices in a blade row [56].

2.3 Flow Effects

First, it is important to understand the physics behind the flow in the mid turbine frame. In this section the effects which take place in the S-shaped duct are discussed. Generally, the flow through a stage, whether rotating or stationary, leads to secondary flows. These effects result in thermal turbomachines in several different types of secondary vortices. Four of these effects are explained in the following [48, 56]. A schematic illustration of these effects is pictured in Figure 2.8.

Generally, the velocities at the suction and at the pressure side of blades are not the same. At the trailing edge of a blade, this fact combined with

25

effects of the boundary layer lead to a velocity gradient, so called wake depression and to the development of the trailing edge vortex (TEV) (HW in Figure 2.8(a)). These vortices have an alternating sense of rotation.

Due to boundary layer and friction effects, the velocity near the wall is different to the velocity in the far field. This is valid for all near wall flows in the turbine, so also for the casing upstream of a blade. When this velocity profile hits the leading edge of a blade, it comes to a "rolling up" of the boundary layer. This leads to vortices, the so called horseshoe vortices (HuE in Figure 2.8(b)). These vortices are separated by the leading edge in suction and pressure side horseshoe vortices (also called horseshoe vortex leg). This mechanism is illustrated in Figure 2.9 with the help of a cylinder.
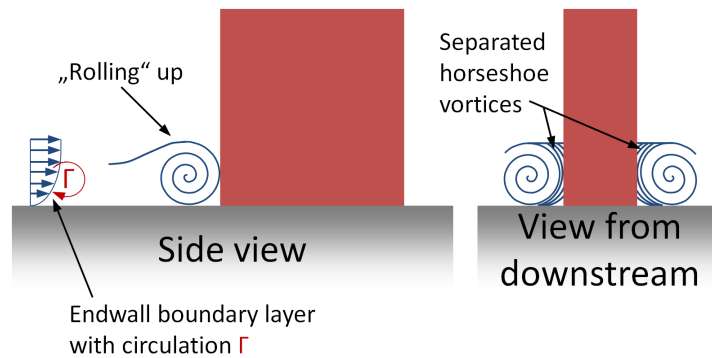
Figure 2.9: Rolling op of an endwall boundary layer forming horseshoe vortices cylinder.

Close to the hub and shroud endwalls, the flow cannot not follow the turning of the blades, since the velocities at the walls are zero. Due to this fact it will follow the pressure gradient (pressure to suction side). The fluid flows from the pressure to the suction side at the endwalls and a balance flow in the middle of the channel appears to fulfil the continuity of mass. These three gradients induce two vortices, so called passage vortices (KW in Figure 2.8(b)). The balance flow at midspan splits the channel in a lower and an upper part, thus the vortices can be distinguished as a lower (LPV) and an upper passage vortex (UPV).

If a rotating blade has no shroud, a gap between the blade tip and the stationary endwall has to be designed. This gap avoids the contact of the blade and the endwalls. In this gap, the flow is not guided by the blade, thus the flow passes through the gap from the pressure to the suction side. This flow leads to the tip leakage vortexes (SpW in Figure 2.8(b)).

These four effects in a turbine stage generate losses, hence it is important to minimize these secondary effects and most important, avoid that these vortices will be transported or even enhanced from one stage to the downstream stage. In the TMTF such a transport and enhancement takes place, hence it is vital to analyse this part.

In addition to the traditional vortices, some other effects can be observed in an S-shaped duct. As Göttlich published in [16], the pressure distribution in the mid turbine frame is not only the result of the change in the flow-area which can be found in not-S-shaped ducts too but is also effected by the curvature of the channel. These effects were simulated by Göttlich and can be seen in Figure 2.10. In Figure 2.10(b) the static pressure coefficient C_p is plotted at the ordinate. C_p is calculated with

$$C_p = \frac{p - \overline{p_{inlet}}}{\overline{p_{t,inlet}} - \overline{p_{inlet}}} \qquad (2.1)$$

The first bend away from a machine-axis-parallel flow-path results in a positive pressure gradient from the casing (low pressure) to the hub (high pressure) due to the guiding of the flow by the endwalls. This effect superimposes with the pressure gradient, which is created by the diffusion of the expansion of the flow area. At the end of the duct, the flow has to be guided back to an axis-parallel stream to match the inlet of the subsequent low pressure stage. This bend causes a reverse pressure gradient, so from the hub to the shroud. The differences in the pressure also effect the distribution of the Mach number which can be observed in the contour plot of Figure 2.10(a).

Göttlich [16] also summarized and analysed the outcomes of several studies performed at the University of Durham Swan Neck Duct Facility (see [57–62]). Theses studies presented several influences on the flow through an S-shaped duct. The outcomes are presented in the following [16]:

Influence Of Wakes

The boundary layer has an important influence on the losses of the flow, due to the velocity gradients. The already discussed secondary effects of the high pressure rotor have an influence on the development of the BL in the downstream MTF duct. The first bend leads to a transport of the flow from the hub toward the casing. This radial gradient is the strongest in areas, where the wakes of the HP rotor appears. Obviously, the pitch angle changes due to the radial displacement. The boundary layer also shows an evidence of this effect: While the BL at the hub remains circumferentially
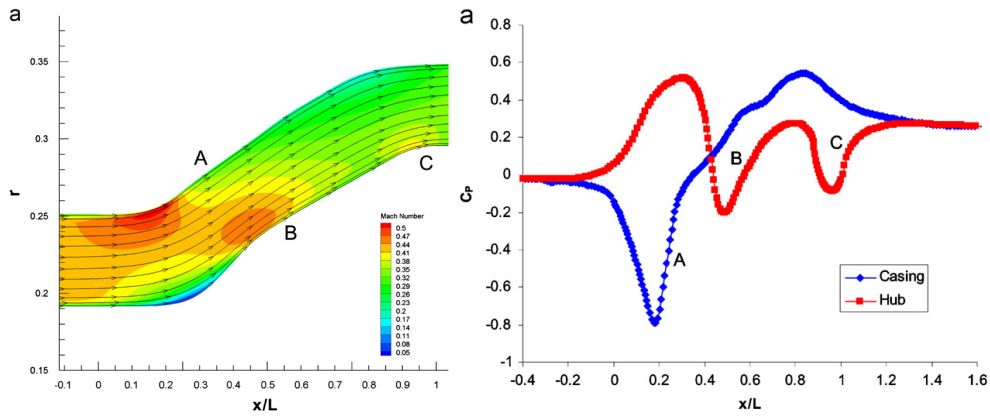
(a) Distribution of the Mach number (b) The pressure distribution at the endwalls.
through the duct.

Figure 2.10: Simulation results in an S-shaped duct [16].
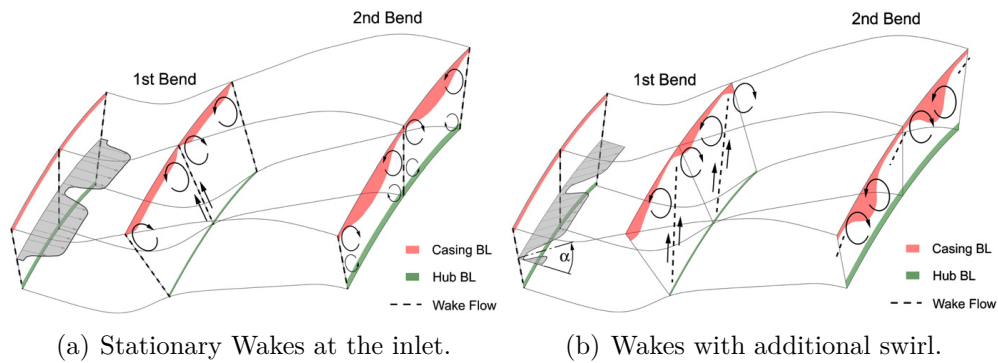
(a) Stationary Wakes at the inlet. (b) Wakes with additional swirl.

Figure 2.11: Schematic flow through the duct [16].

uniform, the thickened boundary layer at the shroud shows an influence
of the gradient mainly at the regions of the wakes. These flows are given
schematically in Figure 2.11(a). The second bend leads to a reverse pressure
gradient, but the expected change in the boundary layer is missing. A result
of the radial flow are vortices, which can be observed at the hub, as well as at
the casing. Due to these swirls, the yaw and the pitch angle are influenced.
One major outcome of [16] is, that no change of surface static pressure can
be observed compared to a wake-free duct, only a redistribution of the losses
takes place. [16]
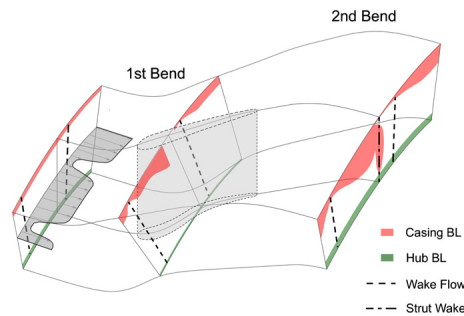
Figure 2.12: Schematic flow through the duct: Wakes and strut blades [16].

Influence Of Swirl

In addition to the wakes discussed before, swirl influences the change of the flow field even more. The swirl causes a pressure gradient which is opposite to the gradient induced by the first bend of the duct and is additive to the gradient by the second bend. The influence of the swirl is given in Figure 2.11(b). The wakes are skewing towards the shroud which leads to an accumulation of high loss fluid there. Consequently, the swirls at the hub and shroud move to each other and vortices with the same sense of rotation will merge together. However, the vortices at the casing are still the dominant structures. [16]

Influence Of The Diffusion Rate

Norris and Dominy [60] analyzed two ducts, both with the same area change as well as the same radial dimensions, but with different axial length. The outcome was, that a shorter duct leads to a higher acceleration and hence to a larger diffusion due to the smaller bending radius of the curvature. This means, that the axial length has a significant influence on the loss of total pressure. [16]

Influence Of Struts

It was mentioned in Chapter 1 that strut blades will become very useful in future multi-shaft engine designs. These struts have a very significant influence on the pressure distribution through the duct. It is obvious, that the strut blades lead to a blockage effect within the duct, since the flow area decreases, hence to an acceleration of the flow. The overall pressure recovery is reduced which leads to a lower energy extraction on the subsequent low pressure turbine stage. As example, the outcomes of [62] will be given. In

this analysed case, the loss in the duct is nearly doubled in comparison to a clean duct. One reason for this is the massive flow separation close to the shroud. In Figure 2.12 a schematic distribution of the flow is shown. Compared to the figures above (2.11(a) and (b)), the inlet wake is shifted circumferentially to avoid a wake-leading edge interaction with the blade. At the pressure side of the strut, where the wake contacts the blade, no separation and therefore no return-flow can be observed. On the suction side of the strut, however, very low pressure regions can be found with negative velocities, so return-flow takes place. At the casing, low energy zones are lifting off the casing and form loss cores. An outcome of the investigation is that it is necessary to consider the flow separation as well as the blockage effect in the design process. However, a change in the channel shape to reach a higher flow area can compensate the blockage effect of the struts. [16]

CHAPTER 3

Simulation Setup

In this section the setup of the simulation should be explained. First, an overview is given followed by the used mesh for the different simulations. After this, the calculation setup is explained.

As already mentioned, this thesis covers different simulations. The simulations are steady-state simulations of the low-pressure stage and the two-stage turbine as well as an unsteady simulation of the two-stage turbine. In Figure 3.1 the computational domains of the rig are illustrated. Also some mesh structures are shown.

First, a steady state simulation of the low pressure stage has been set up. The first target is to verify the inlet and outlet conditions of the simulation in respect to the measurement data acquired by Spataro [64]. To perform this verification with the low pressure stage only has the advantage that the simulation time is lower and the simulation is easier controllable, hence adjustments can be realized faster. Also this simulation is used to compare the data with the simulation performed by Spataro et al. [24], who analysed the baseline without splitters.

After finding the right conditions, these conditions are used for the two-stage, two spool turbine simulation. The results of this steady state simulation are mainly used to compare the two used codes with each other.

Last but not least an unsteady simulation of the two-stage turbine has been performed with LINARS.
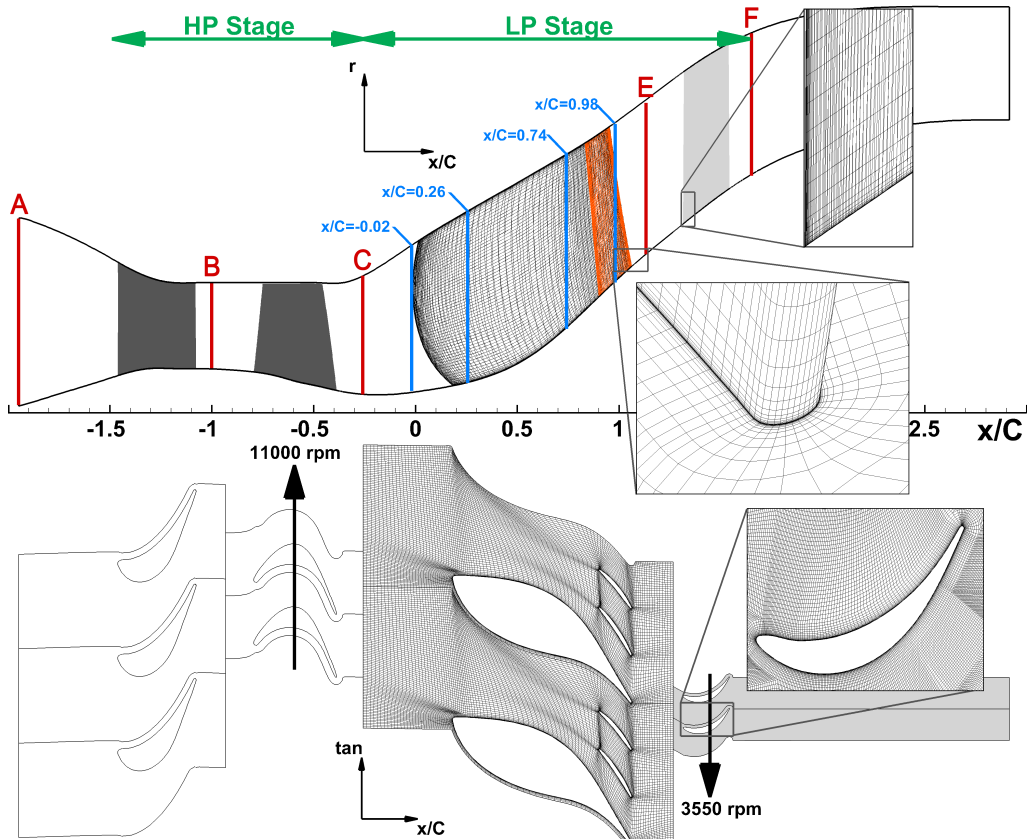
Figure 3.1: The turbine test facility at the ITTM, also showing computational domains (based on [63]).

3.1 Mesh

The mesh for the simulation has been created with the program AIGrid. This program has been written by Pieringer [65] under the supervision of the *ITTM*. AIGrid constructs a structured grid and is especially used to set up meshes for turbomachinery.

Although the CFX® package comes along with its own mesh generator, named TurboGRID®, AIGrid has been used to construct the grid for CFX® as well as for LINARS. The reason is, that the mesh generator by *Ansys* is very general. The AIGrid generator on the other hand gives the opportunity to adjust the mesh in detail and configure for instance the point positions at the walls, the number of nodes or the relaxation factor. A second reason is, that the calculations are better comparable when the different codes use the same grids.

(a) IndexFac 1, no relax.   (b) IndexFac 4, no relax.   (c) IndexFac 4, relax.
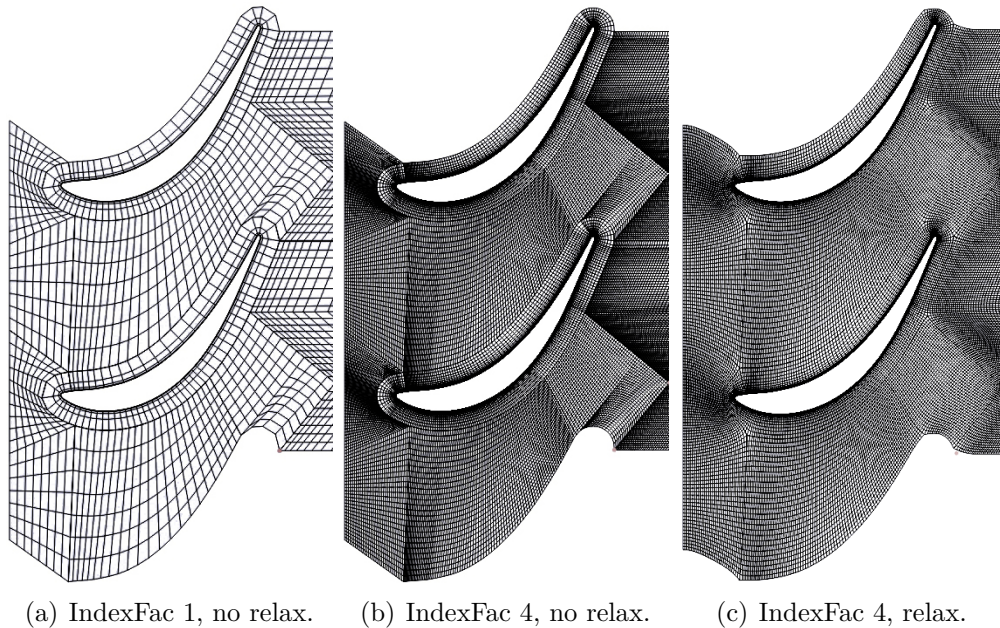
Figure 3.2: Comparison of the generated mesh with IndexFac 1 and 4 with or without relaxation

Figure 3.2 illustrates two out of many adjustment opportunities of the AIGrid generator. Figures 3.2(a) and (b) show the differences between IndexFac 1 and 4. The IndexFac describes how coarse or fine the mesh is. A mesh generated with IndexFac 4 has 4^3 more nodes compared to a mesh with IndexFac 1. The differences between Figures 3.2(b) and (c) is the relaxation. The relaxation is a method to reduce hard edges and rough passages and replace them with a smooth constructed mesh. The changes lead to a more accurate solution and a faster convergence rate.

Steady State - Low Pressure Stage

As mentioned before, the first step of the simulation was the analysis of the low pressure stage only. The mesh used for this simulation consists of two parts: The stationary mid turbine frame and the rotating low pressure rotor. The LP rotor has a rotation speed of 3550 rpm. The TMTF inlet is plane C (see Figure 3.1). The outlet boundary has been placed at the axial distance of $(x_{out} - x_{LP_{rotor},TE})/C_{LP_{rotor}} = 6$ downstream of the LP rotor trailing edge. At this position also the pressure has been measured in the previous baseline study performed by Spataro [64].

33

Table 3.1: Steady state simulation mesh statistic of both stages.

Domain	Nodes	Elements
S1 HP	*1.046.196*	*1.004.800*
R1 HP	*2.136.360*	*2.069.760*
S2 MTF	*1.070.334*	*1.026.560*
R2 LP	*2.287.764*	*2.218.240*
All Domains	***6.540.654***	***6.319.360***

Between the rotating and the stationary parts of the mesh, there has to be an interface connecting the two domains. In this simulation, a mixing plane (in CFX® called stage) is used to connect the two parts.

The mesh of the low pressure rotor of midspan can be seen in Figure 3.2(c). The statistics is listed in Table 3.1 together with the HP stage. The low pressure stage consists of about 3.2 million elements.

Steady State - Low And High Pressure Stage

The second simulation computed the whole two stages of the turbine facility. Therefore, the mesh of the LP stage calculation has been extended. Two additional parts, a high pressure vane row and rotor has been added to the mesh. The grid of the HP stage has been generated with the same fineness as the LP stage mesh. The mesh consists of about 6.3 million elements. Statistic of the grid can be found in Table 3.1.

The high pressure rotor has a rotational speed of -11000 rpm[1]. Also mixing planes have been used as an interface between the different domains.

Unsteady Simulation

The unsteady simulation also computes the two-stage turbine, but the mesh differs a little from the mesh used for the steady state simulation: The exit wake behind the low pressure rotor has been modelled as an independent stationary part. One main reason to perform an unsteady simulation is to resolve unsteady rotor-stator interactions. Thus it would be necessary to simulate the whole engine, which means that the mesh should cover 360°. To reduce calculation time and memory usage, also the smallest denominator can be used for the mesh setup. In the analysed turbine, this smallest denominator is a 90 degree angle. The resulting number of domains can be found in Table 3.2 together with the number of elements. The unsteady

---

[1] The minus indicates that the rotor is counter-rotating.
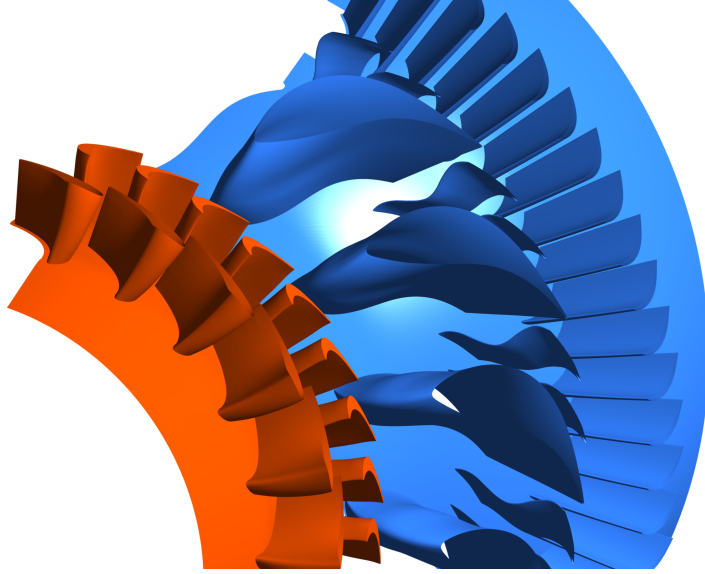
Figure 3.3: The rendered computational domain showing the 90 degree mesh (HP stage in orange and LP stage in blue).

Table 3.2: Unsteady mesh statistics: Number of blades and elements.

Domain	Number	Elements
S1 HP	6	6.028.800
R1 HP	9	18.627.840
S2 MTF	4	16.424.960
R2 LP	18	5.667.840
Exit Wake	18	2.903.040
All Domains		49.652.480

mesh has more than 49 million elements. A three-dimensional illustration of the grid can be found in Figure 3.3.

First, an initialization is necessary to have an accurate convergent result to start the unsteady calculation. This flow field initialization has been calculated with a mesh using mixing planes as interfaces. For the actual unsteady simulation Transient Rotor-Stator interfaces have been used. The used timestep was set to $t_{step} = 0.05050505 \cdot 10^{-6}$ s. The calculation of the timestep is explained in Chapter 3.3 (Page 41).
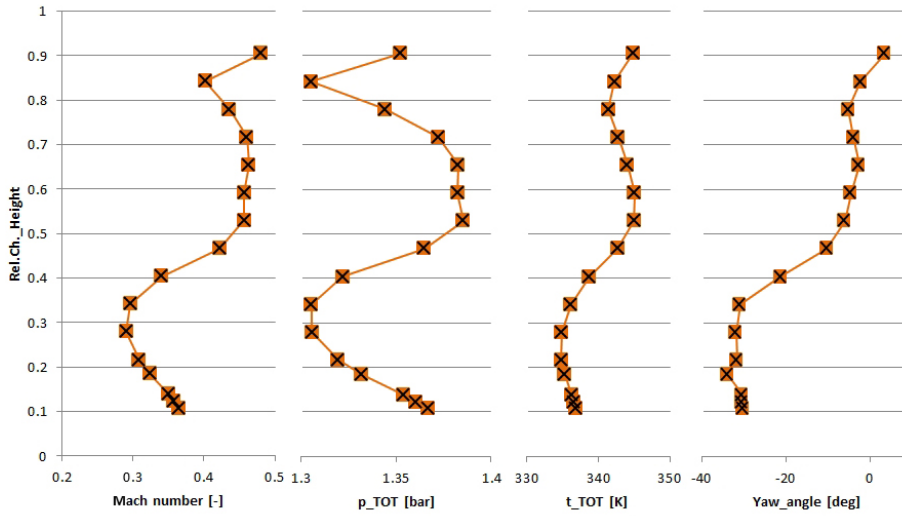
Figure 3.4: Radial distribution of the boundary conditions at the inlet (Plane C) taken from the experiment.

3.2 Steady State Simulation

As mentioned at the beginning of Chapter 3, the first step of the simulation was a steady-state calculation of the low pressure stage. To perform a CFD simulation, several inlet and/or outlet conditions are necessary as input parameters. In this simulation, four main parameters have been set at the inlet and one parameter at the outlet. The inlet values are the direction of the velocity, the total pressure, the total temperature and the turbulence values and at the outlet the static pressure is set. First, measurement results at plane C (location see Figure 3.1 at page 32) have been used as inlet conditions for the CFD simulation. The boundary condition include

- p_{tot}
- T_{tot}
- c_{ax}, c_{rad} and c_{tan} to define the flow angle

These inlet conditions are shown in Figure 3.4 as radial distributions. The three velocity components c_{ax}, c_{rad} and c_{tan} have been combined in the
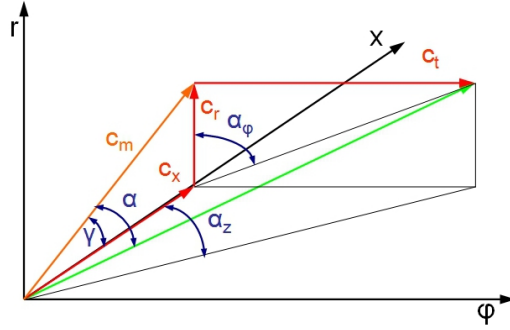
Figure 3.5: Angle definition in a circular coordinate system with α is the yaw angle.

yaw angle α. This angle is calculated with

$$\alpha = \arctan\left(\frac{c_{tan}}{c_m}\right) \tag{3.1}$$

$$c_m = \sqrt{c_{rad}^2 + c_{ax}^2} \tag{3.2}$$

An illustration of the yaw angle α is given in Figure 3.5.

In addition to these three values, the turbulence has to be defined. In this simulation the turbulence intensity and the mixing length are set with 10 % and 0.001 m, respectively. The static outlet pressure is still left to define. To find this pressure three main targets have been chosen to reach a comparability with the experiment. These targets are as follows:

- The blade loading of the strut blade in the mid-turbine frame
- The mass flow through the turbine
- The pressure behind the low-pressure turbine (Plane F)

With theses defined targets, the static outlet pressure/mass flow at the exit plane of the mesh has been varied to reach these aims. For a better understanding it should be pointed out, that the static pressure at the outlet is not equal to the static pressure at plane F! Several outlet pressures (and one mass flow) have been implied. In Table 3.3 the used pressures are listed together with an explanation, why the pressure was chosen.

The results of these four simulations have been compared to find the optimum static pressure $p_{stat,out}$ for the simulation. The comparison has only been performed with CFX®, only the best result has been simulated with LINARS as well.

Table 3.3: Chosen pressures (mass flow) for the optimization.

	Code	$p_{stat,out}/\dot{m}$	Reason
I	CFX®	0.98 bar	First Shot. Expected $p_{stat,out}$ at the test facility.
II	CFX®	15.5 kg/s	Mass flow in the experiment.
III	CFX®	0.922 bar	$p_{stat,F}$ in the experiment.
IV	CFX®	0.89 bar	Best value concerning the strut blade loading.
	LINARS	0.922 bar	$p_{stat,out}$ in the experiment.
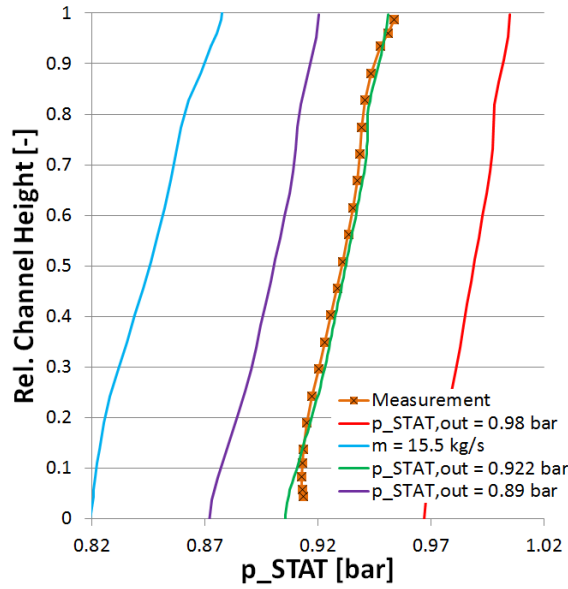
Figure 3.6: Radial distribution of the static pressure at plane F.

As mentioned, the three comparison targets have been used for the finding of this pressure. The three comparisons are given in Figure 3.6 and 3.7. Figure 3.6 shows the radial distributions of the static pressure at plane F, while Figure 3.7 shows the blade loading at 25 % and 50 % span together with the mass flows listed in the legend (in Figure 3.7(b)).

[**Simulation I**] For the first simulation, the measured pressure at the exit plane was used as the outlet condition for the simulation. This pressure is $p_{stat,out} = 0.98$ bar. Figure 3.6 shows a difference between the measurement results at plane F and the simulation results. This difference can be explained with the differences in the mass flows (see legend in Figure 3.7(b)). The measurement has a higher mass flow ($\dot{m} = 15.5$ kg/s) compared to the simulation ($\dot{m} = 14.12$ kg/s). The higher mass flow of the measurement leads to a higher velocity in the channels. Since the pressure loss Δp is
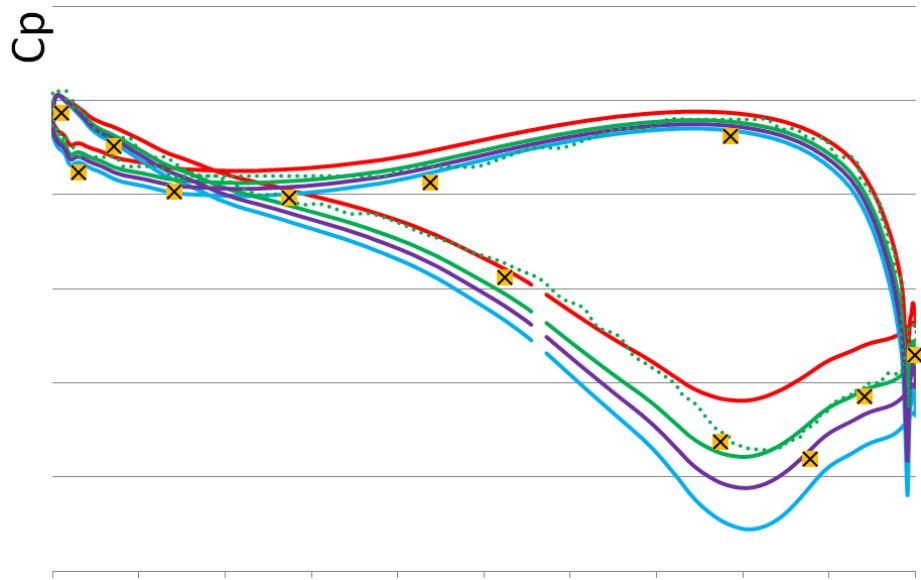
(a) 25% span
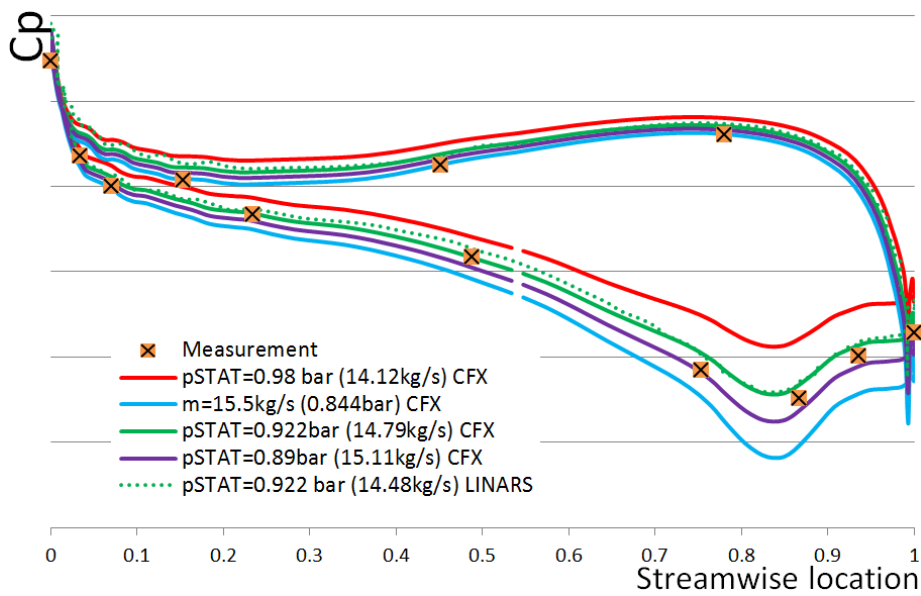
(b) 50% span

Figure 3.7: The strut blade loading curves in comparison to the experiment at different spans.

Table 3.4: Relative errors of the different comparison-targets in percent.

	$p_{stat,out}/\dot{m}$	$e_{Mass\ flow}$	$e_{p_{stat,F}}$	$e_{Blade\ loading}$
I	0.98 bar	-8.90	6.22	3.26
II	15.5 kg/s	0.00	-9.07	1.77
III	0.922 bar	-4.58	0.08	0.99
IV	0.89 bar	-2.52	-3.35	0.62

proportional to the square of the velocity, a lower pressure drop of the simulation is expected between plane F and the exit plane. Thus, the measured pressure at plane F is lower compared to the pressure of the simulation with $p_{stat,out} = 0.98$ bar. Also high differences between the blade loadings can be observed in Figure 3.7.

[**Simulation II**] The second simulation to define the static outlet pressure used the measured mass flow as outlet condition. This mass flow from the experiment is $\dot{m} = 15.5$ kg/s. To reach this mass flow, the simulation computed a resulting static outlet pressure of $p_{stat,out} = 0.844$ bar. This pressure is lower than the measured pressure ($\Delta p = 0.09$ bar) and also shows a far lower pressure at plane F (Figure 3.6). Also the strut blade loading differs remarkably compared to the measurement.

[**Simulation III**] The third try to find the best agreement between the three goals was the use of $p_{stat,out} = 0.922$ bar. This pressure was used to reach the same pressure as the measured pressure at plane F. Thus, the pressures at this plane correspond in Figure 3.6. Also the blade loading between this simulation and the measurement is hardly different. The computed mass flow of $\dot{m} = 14.79$ kg/s is lower compared to the measured mass flow ($\dot{m} = 15.5$ kg/s).

[**Simulation IV**] The aim of the last simulation was to set a pressure, which would correspond with the measured blade loading. Mainly at 50% span (Figure 3.7(b)) this aim was fulfilled and also at 25% span (Figure 3.7(a)) the discrepancies are not high. The static pressure at plane F differs from the measured data, which can be observed in Figure 3.6. The mass flow again differs between the measurement and this simulation.

In Table 3.4 a overview of the errors of the different simulations is given. The relative error is calculated with

$$e_{rel} = \frac{\langle x \rangle - \langle x_{Measurement} \rangle}{\langle x_{Measurement} \rangle} \tag{3.3}$$

where $\langle x \rangle$ is the averaged simulated value and $\langle x_{Measurement} \rangle$ is the averaged measured value.

The table shows, that the Simulation II has obviously no error concerning the mass flow target. Simulation III has the smallest error when comparing the static pressures at plane F and Simulation IV has the smallest error, when comparing the blade loading. A comparison of the different values shows, that Simulation III has the best overall agreement with the measured data: This simulation has the smallest error concerning the static pressure at plane F and has also a relative small error $e_{Blade\ loading}$. The mass flow error is indeed higher compared to simulation II or IV, but for the comparability of the simulation and the measurement, it is more important that the flow conditions within the duct, hence the pressures are similar.

The static outlet pressure was then set to $p_{stat,out} = 0.922$ bar for the following simulations. This pressure has been used for the LP stage calculation as well as for the two-stage setup.

The two-stage calculation needs other inlet conditions, since the inlet plane A is situated upstream the high pressure vane row. Again, four conditions as mentioned before are used. The values at the inlet were set as follows:

- total pressure $p_{tot} = 3.85$ bar,

- total temperature $T_{tot} = 433.15$ K,

- inflow direction normal to boundary,

- turbulence intensity 10% and mixing length 0.001m.

The values were again taken from measurements.

All results from the two-stage as well as from the one-stage calculation can be found in Chapter 4.

3.3   Unsteady Simulation

Another topic of this thesis is an unsteady simulation of the whole two-stage turbine. An unsteady calculation computes the conservation equation for every timestep, hence this type of simulation generates a time resolved result. This is important to observe unsteady effects within the turbine, like wakes, shock waves, rotor-stator interactions or turbulence effects. To reach a useful resolution, it is important to calculate the used timestep t_{step} correctly and wisely. The timestep represents the actual time which is passing between two iterations.

To calculate t_{step}, first the blade passing frequency (BPF) has to be calculated. This is done with Equation (3.4) with n as the rotation speed of the HP rotor and z as the number of blades of the HP rotor. The BPF
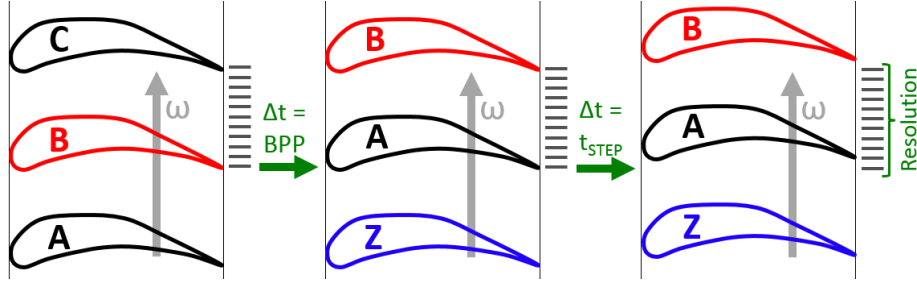
Figure 3.8: Illustration of t_{step}, BPP and Resolution.

describes the frequency of blades passing one point, e.g. one stationary vane blade. This value is also important for the noise emissions of for example the fan. The high pressure rotor is used for this calculation, because it has the highest rotation speed which leads to a higher BPF. If the low pressure rotor would be used for this calculation, the resolution of the calculation would not be high enough to see the fluctuations within the high pressure passage.

$$BPF = \frac{n \left[\text{rad}/\text{s}\right] \cdot z}{60} = \frac{11000 \ \text{rad}/\text{s} \cdot 36}{60} = 6600 \text{ Hz } (\text{Blades}/\text{s}) \qquad (3.4)$$

With the rotation speed $n = 11000$ rad/s and the number of blades $z = 36$ Blades of the HP rotor the BPF can be calculated to $BPF = 6600$ Hz.

With the BPF the blade passing period (BPP) can be calculated with Equation (3.5). This value represents the time, a blade needs to pass one pitch. This movement is illustrated in Figure 3.8. Blade B (red) rotates from its origin middle position towards the upper position passing one pitch. The time the rotor needs to perform this rotation is the BPP.

$$BPP = \frac{1}{BPF} = 1.515151 \cdot 10^{-4} \text{ s} \qquad (3.5)$$

For the high pressure rotor the BPP is $1.515151 \cdot 10^{-4}$ s. If this time is used as timestep the rotor would appear stationary in the results, since at every timestep two blades changed their places. Obviously to have a meaningful result, the timestep has to be smaller. The resolution r is used to define how many calculations are performed within one BPP. In Figure 3.8 a resolution of 10 is illustrated. Blade A (black) rotates one resolution step. The time used for this movement is the timestep. This means that with the BPP and the resolution r the timestep t_{step} can be calculated, see Equation (3.6). Therefore the BPP is divided by the resolution of the

Table 3.5: Summary of the timestep calculation.

BPF	BPP	t_{step}	Ω	ω
6600 Hz	$1.515151 \cdot 10^{-4}$ s	$0.05050505 \cdot 10^{-6}$ s	10 $^{\text{deg}}$/Blade	$0.0\dot{3}°$

simulation. The example is calculated with a resolution of 100, which means that the simulation computes 100 steps for one pitch.

$$t_{step} = \frac{BPP}{r} = \frac{1.515151 \cdot 10^{-4}}{100} = 1.515151 \cdot 10^{-6} \text{ s} \qquad (3.6)$$

Not only the time between two steps, also the position of the rotor is interesting. Thus the angle which the rotor rotates during a timestep should be calculated. First, the angular pitch Ω between two blades is calculated with Equation (3.7). If this angle is divided by the resolution, the resulting angle ω is the rotating angle between two iteration steps.

$$\Omega = \frac{360 \; deg}{z} = 10 \; ^{\text{deg}}/\text{Blade} \qquad (3.7)$$

$$\omega = \frac{\Omega}{r} = 0.1° \qquad (3.8)$$

In this example the angle ω is 0.1°. This result means, that a rotor needs $1.515151 \cdot 10^{-6}$ seconds ($= t_{step}$) to perform one step of the resolution. In this time the rotor rotates 0.1 degree ($= \omega$).

The unsteady simulation has been done with LINARS. The calculation has been done with a resolution of $r = 300$. This leads to a $t_{step} = 0.05050505 \cdot 10^{-6}$ s. This means, that 2700 iterations are necessary to calculate 90° rotation of the high pressure rotor. A summary of the calculated values for the simulation can be found in Table 3.5.

CHAPTER 4

Results

4.1 Effects Of Split Blades On The Flow

In this section of the thesis the first results of the simulation are discussed. These results are compared to the baseline (without splitters). The numerical setup of the baseline was performed by Spataro et al. [24]. For the comparison in this work, this setup was re-simulated with the same inlet conditions as described in Section 3.2.

It should be mentioned, that the endwall contour was not changed between the two cases. This results in a smaller effective flow area at the rear part of the TMTF with the splitter design. This adjustment was not done due to cost considerations and comparability with the baseline. To reach a comparability, the same reduced speed and reduced mass flow was used in both simulation, hence the static outlet pressure differs due to the blockage effect.

The numerical setup for simulation has already been described in Chapter 4.2. The used measurement techniques can be found in [24, 64].

The results in this section cover changed flow features as well as new features triggered by the splitter design.

Inlet Conditions

As already mentioned, the inlet boundary conditions were set as a radial distribution. This radial distribution has been taken from the experiment. In Figure 4.1 the radial distributions of the non-dimensional total pressure coefficient C_{P_T} and the Yaw-angle α in plane C are given. The total pressure
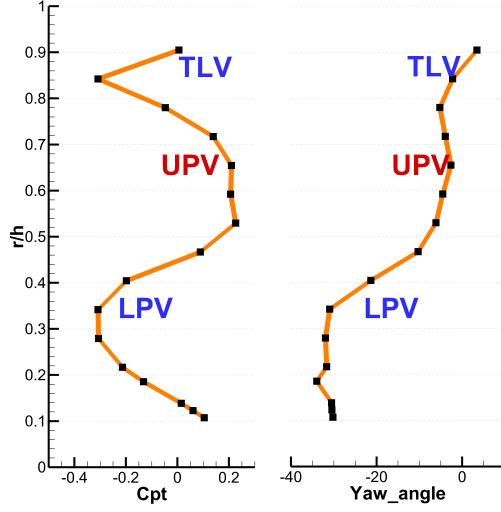
Figure 4.1: Inlet distribution as boundary condition for the simulation in plane C.

coefficient is defined as

$$C_{P_T} = \frac{p_T - \overline{p_{T,C}}}{\overline{p_{T,C}} - \overline{p_C}} \tag{4.1}$$

where p_t is the local total pressure, $\overline{p_C}$ and $\overline{p_{T,C}}$ represent the mass-averaged static and total pressure at plane C, respectively.

The inlet distributions show the influences of the upstream HP stage. These distributions show the three major structures (compare with Miller et al. [66]): A low passage vortex (LPV), an upper passage vortex (UPV) and a tip leakage vortex (TLV) of the unshrouded HP rotor. Since the secondary flow effects of the blades lead to a change in the energy extracted, as well as to a change of the flow angle, the vortices can be located in the charts in Figure 4.1. The LPV is located at about $r/h = 0.3$, the UPV at about $r/h = 0.65$ and the TLV at about $r/h = 0.8$. Because less energy is extracted by the HP turbine blade due to the tip clearance, α is lower and the C_{P_T} is higher close to the shroud ($r/h > 0.85$). [24]

To verify the accuracy of the simulation the blade loading of the strut is compared. In Figure 4.2 the strut blade loading at 25%, 50% and 75% span positions is shown. This figure shows the non-dimensional pressure coefficient C_p of the simulated and measured data of the embedded design (ED) together with the baseline (BL). C_p is calculated similar to C_{P_T} (Equation (4.1)) with:

$$C_p = \frac{p - \overline{p_C}}{\overline{p_{T,C}} - \overline{p_C}} \tag{4.2}$$

45

(a) 25% span	(b) 50% span	(c) 75% span
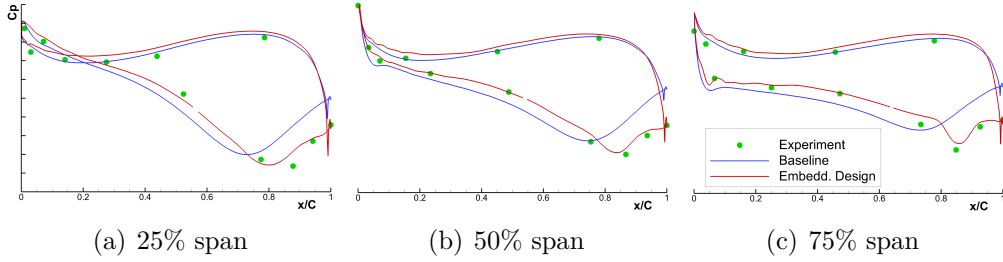
Figure 4.2: Spanwise TMTF strut blade loading.

where p is the local static pressure. The comparison of the CFD result and the measured data of the embedded design is satisfactory.

The additionally given graph of the baseline case in Figure 4.2 shows a higher pressure coefficient at the suction side of the strut compared to the embedded design. Also the minimum is situated slightly more upstream. The reason is the blockage effect of the splitter design, which results in a higher acceleration at the latter part of the blade, hence the pressure is lower. A cross-over of the pressure at 25% span (Figure 4.2(a)) indicates a negative incidence, while the pressure coefficient distribution at 75% span (Figure 4.2(c)) shows a positive incidence.

Flow evolution in the TMTF

To understand the flow through the TMTF, several planes were extracted. The positions of these planes are $x_{mid}/C = -0.01$, $x_{mid}/C = 0.26$, $x_{mid}/C = 0.73$, $x_{mid}/C = 0.885$, $x_{mid}/C = 0.905$, $x_{mid}/C = 0.98$ and $x_{mid}/C = 1.02$ (see Fig. 4.3). The first three planes are inclined in order to be approximately normal to the flow direction. The latter four planes are parallel to the splitter leading edge and the splitter/strut trailing edge, respectively. The coordinates x_{mid}/C refer to the position of the midspan of the planes. In these positions the streamwise vorticity ω_{SW} (Equation (4.3)), the static pressure coefficient C_p (Equation (4.2)) and the non-dimensional losses ζ (Equation (4.4)) have been evaluated. The contour plots of theses values are given in Figure 4.4. In this picture the losses ζ are normalized to the mass-averaged loss at the midspan (50% span) at the TMTF exit plane $\overline{\zeta_{mid,E}}$ (Plane E).

$$\omega_{SW} = \frac{v_x \cdot \omega_x + v_y \cdot \omega_y + v_z \cdot \omega_z}{v} \tag{4.3}$$

$$\zeta = \frac{\overline{p_{T,C}} - p_T}{\overline{p_{T,C}} - \overline{p_C}} \tag{4.4}$$
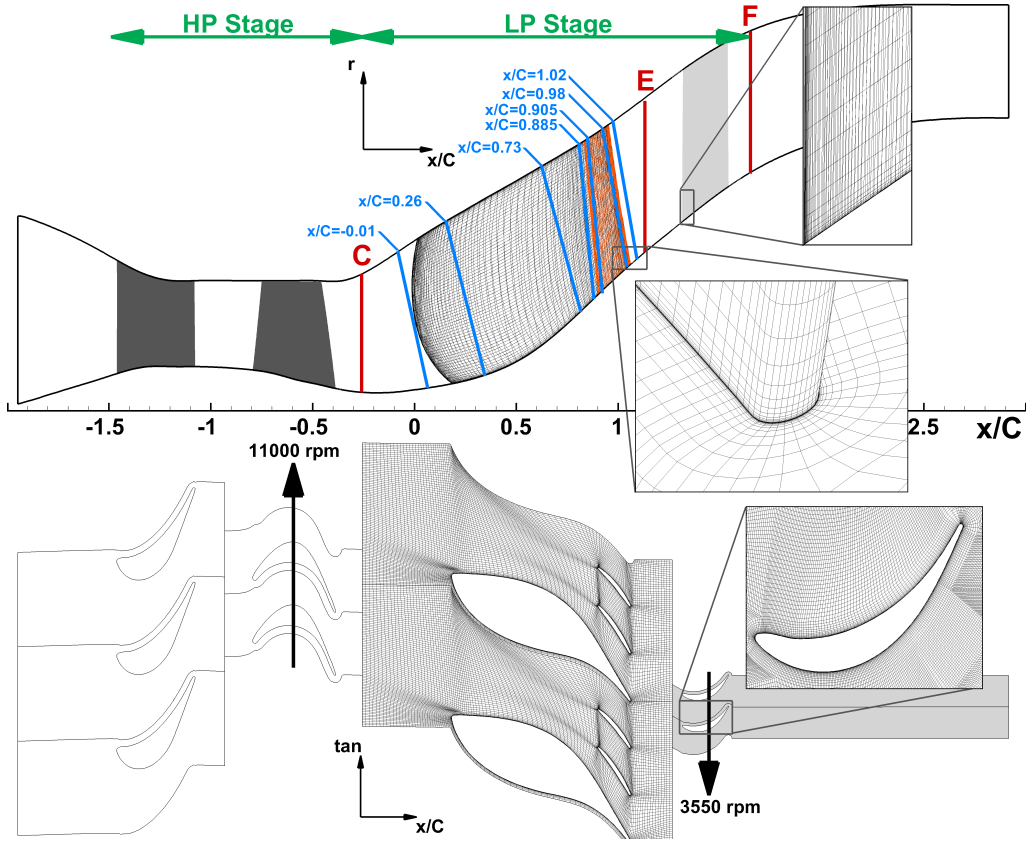
Figure 4.3: The turbine test facility showing the planes extracted for the analysis.

For the understanding of the flow it is necessary to understand the flow features triggered by the baseline TMTF and separate them from the effects of the split blades. An intense study of the baseline has been made by Spataro et al. [24]. In the following the outcomes of these studies are summarized, but additional effects are also discussed. In the following, Figure 4.4 has to be regarded together with Figures 4.5(a) to d, which are illustrating the streamlines at the hub, shroud and the blades of the baseline and embedded design, respectively.

The first plane at $x_{mid}/C = -0.01$ is clearly effected by the structures of the upstream HP rotor. The main structures of the oncoming flow are: the low passage Vortex (A), the upper passage vortex (B) and the tip leakage vortex (C). These structures are visible in the ω_{SW} map. Four other structures are also observable in this map: E1, E2, F1 and F2. These structures

47
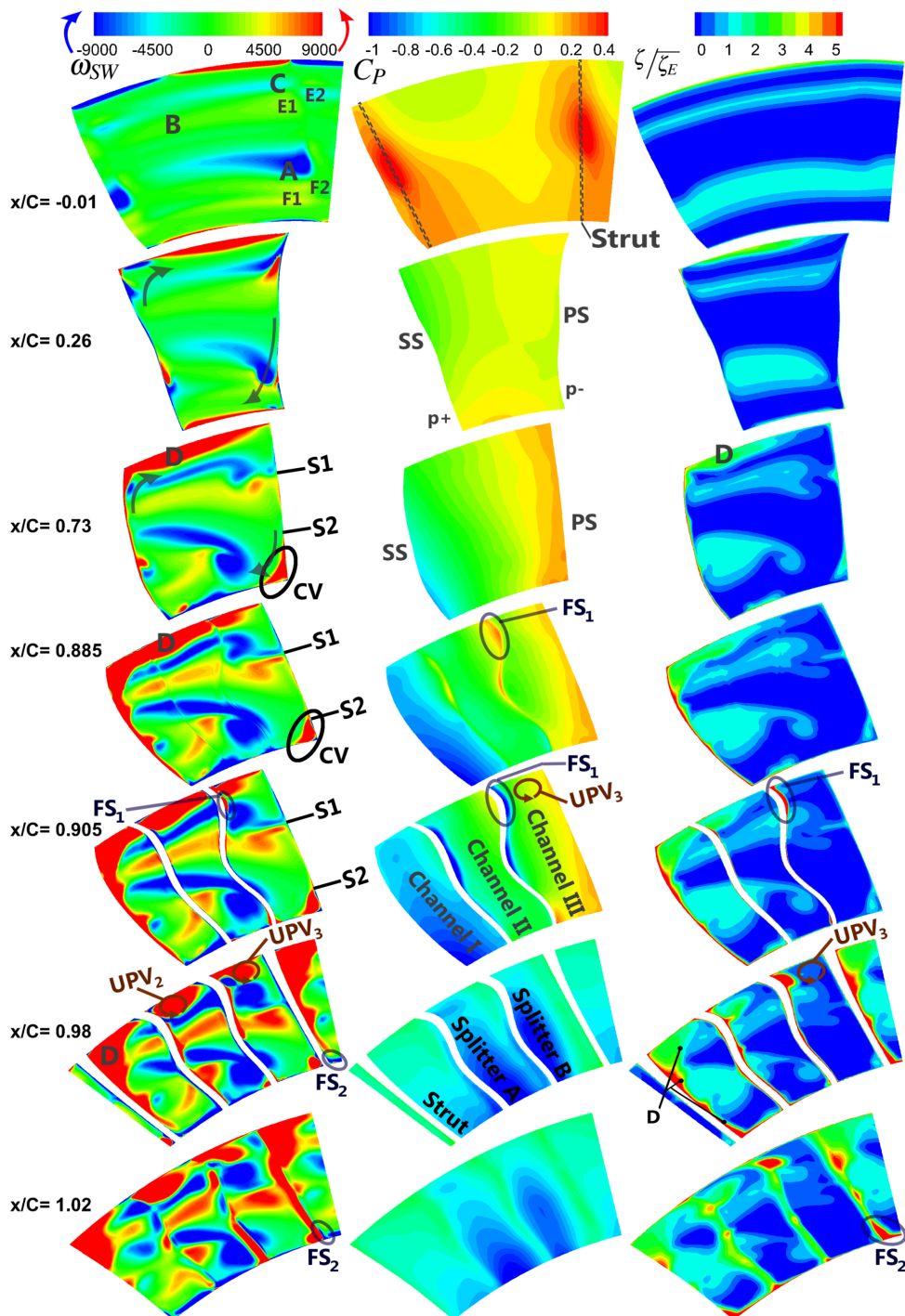
Figure 4.4: The flow evolution in different planes through the TMTF (view from downstream) [20].

(a) Suction side - baseline.

(b) Suction side - Embedd. design.

(c) Pressure side - Embedd. design.

(d) Shroud - Embedd. design.
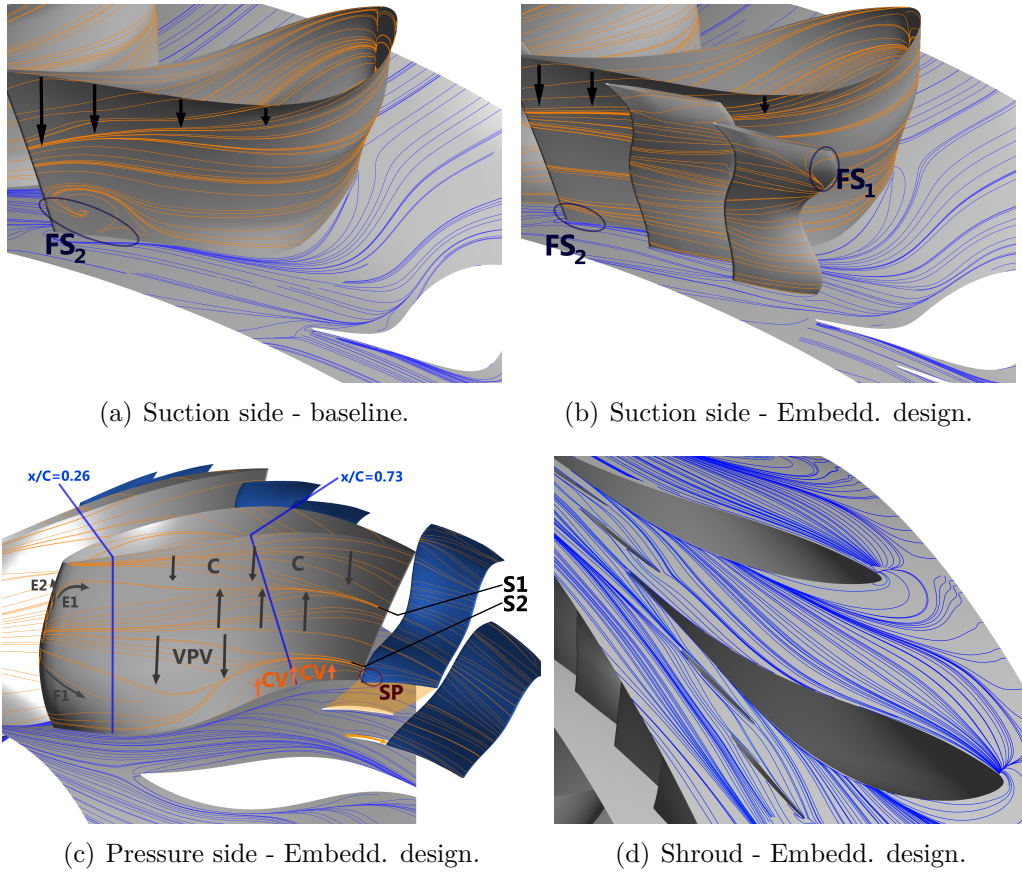
Figure 4.5: Visualization of the streamlines of the baseline and the embedded design.

are triggered by the sweep design of the strut (compare Spataro et al. [24]). When the flow approaches the leading edge a pressure gradient is induced, pushing the flow from midspan toward the hub and shroud, respectively. As a result, these four vortices can be found in the vorticity plot. The structures are divided in an upper (E) and a lower (F) vortex at the pressure (1) and the suction (2) side. These structures also cause a shift of the streamlines close to the leading edge in Figure 4.5(c). In this streamline illustration also the displacement of these four structures by the pressure gradient can be observed.

When looking at the streamlines at the shroud in Figure 4.5(d) the stagnation point as well as the horseshoe vortices can be observed. Clearly the suction and the pressure side leg of the horseshoe vortex can be observed at the strut leading edge and downstream. These two vortices can also be

seen as blue and red zones close to the wall at plane $x_{mid}/C = -0.01$.

The pressure distribution at the next plane $x_{mid}/C = 0.26$ shows two main gradients. The first gradient is induced by the negative incidence of the strut at lower parts of the channel. This circumstance has already been described and can be observed in the blade loading of the strut in Figure 4.2(a). Due to the higher pressure at the suction side compared to the pressure side, a gradient from SS toward PS emerges. Thus a traditional lower passage vortex can not evolve. The second remarkable gradient points from the hub towards the shroud at the whole span of the suction side. This gradient is triggered by the relatively high pressure at the hub suction side and the changing incidence from hub to shroud. This strong gradient favours the development of a counter-clockwise rotating structure, called vane passage vortex (VPV, see Spataro et al. [24]). This vortex covers the whole channel at positions $x_{mid}/C > 0.3$. The structure is indicated with arrows in the vorticity map in Figure 4.4. This VPV also deforms and shifts the vortexes seen at plane $x_{mid}/C = -0.01$ away from the endwalls. For example it diminishes the suction side leg of the horseshoe vortex described above.

The pressure distribution at $x_{mid}/C = 0.73$ shows a strong PS to SS gradient. This gradient enhances the VPV at the hub. At the shroud, this gradient is reverse in respect to the VPV. As the shroud streamlines in Figure 4.5(d) show, this gradient is also not blocked by the VPV. Indeed another vortex is indicated at the shroud, marked with D. This structure results from the enhancing of the pressure side leg of the horseshoe vortex. At $x_{mid}/C = 0.73$ D also includes a corner vortex. The structure D can also be observed in the loss map. The other spots are remains of the HP-LPV, HP-UPV and HP-TLV which were deformed by the VPV. Additionally a corner vortex (CV) is induced at the hub-PS corner, due to the sharp edges. This CV can also be observed in Figure 4.5(c). It shifts the streamlines at the lower part of the channel. Due to the counter-rotating VPV, a separation line is developed, marked as S_2. A second separation line can be found between the VPV and the remains of the HP-TLV, marked as S_1.

The fluid transportation by the pressure gradient and the VPV can also be seen in the streamline illustration in Figure 4.5(a) (Baseline) and b (Embedded design). The streamlines at the hub shows this "downwash" from the pressure side towards the suction side.

So far, the mentioned effects in the channel were not effected by the split blades. In the baseline case, these described flow features are quite similar (only influenced by the different pressures) and they keep their orientation and affect the downstream low pressure rotor. At plane $x_{mid}/C = 0.885$ the first influence of the split blades can be observed. This plane is situated

close to the leading edge upstream of the splitter. The effects should be regarded together with Figures 4.6(a) to c. These Figures show a contour plot of the velocity at different span positions.

(a) 5% SPAN. (b) 65% SPAN. (c) 90% SPAN.
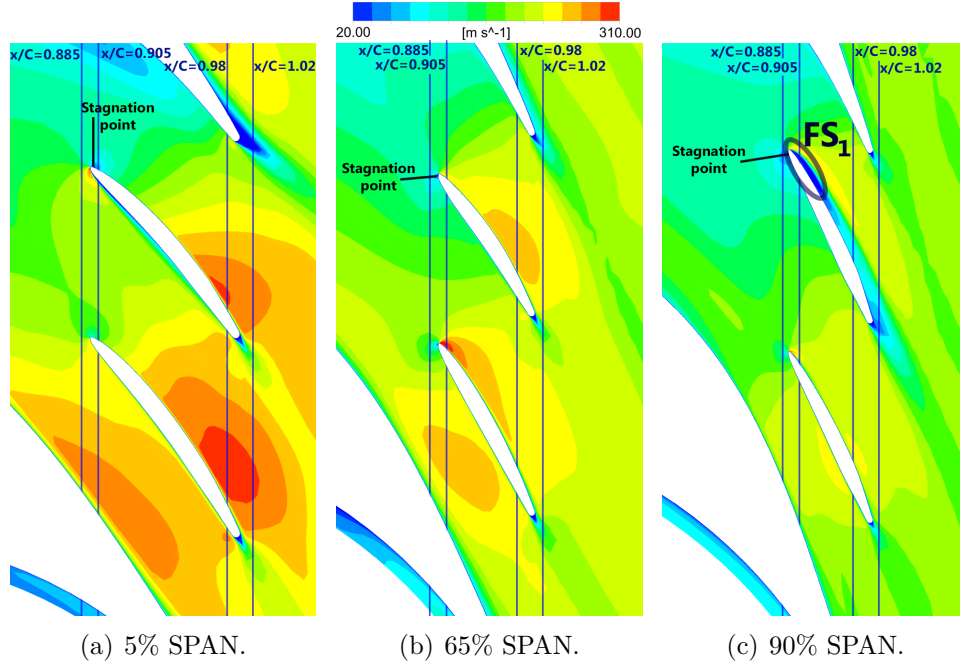
Figure 4.6: Velocity contour plots at different span positions.

The pressure distribution at plane $x_{mid}/C = 0.885$ shows areas of higher pressure in the upper part of the channel, mainly at splitter B. This higher pressure is the result of a wrong incidence which causes a flow separation marked in the plot as FS_1. This separation is also visible in Figure 4.6(c). A flow separation results in high losses. In plane $x_{mid}/C = 0.905$ the losses triggered by FS_1 are visible in the loss map. At this position, also a small vortex induced by FS_1 is visible in the ω_{SW} map. The flow separation also leads to an over-speed in the upper part of the channel (lower pressure) at plane $x_{mid}/C = 0.905$.

Other higher pressure spots which can be found at plane $x_{mid}/C = 0.885$ are also due to a wrong incidence, but do not result in flow separation. These spots indicate the stagnation point of the splitters, thus show the low velocity at this point. This fact can also be seen in Figure 4.6. The same is valid for the low pressure spots at plane $x_{mid}/C = 0.905$, but in this pressure map the low pressure indicates an over-speed, which is the result of a slight difference between the stagnation point at the leading edge. It

51

has to be mentioned, that these effects are quite small and do not indicate losses.

At the two planes $x_{mid}/C = 0.905$ and $x_{mid}/C = 0.98$ the vorticity map shows that the large structures are chopped by the splitters. Also the turning stops, which indicates that the VPV does not exist anymore. Obviously also the upper passage vortex D is chopped into tree parts. These now independent structures are small vortexes, one UPV in every channel. These UPV cause the flow to move from the suction side to the pressure side of each channel. Also UPV_3 forces the fluid towards the suction side of splitter B causing an enhancement of the loss generated by the flow separation FS_1.

The streamlines at the shroud (Figure 4.5(d)) as well as the velocity maps (Figure 4.6) confirm the displacement towards the strut suction side by the VPV. This results in a higher velocity in channel I, whilst the flow speed in channel II and III is lower. The pressure distribution shows a nearly uniform pressure distribution in the channels II and III.

The pressure distribution at plane $x_{mid}/C = 0.98$ and the velocity contour plots in Figure 4.6 show a reduction of the speed, mainly at the upper part of channel I. This is caused by an area increase of this channel. At the same time the available area in channel II decreases, which leads to a higher speed (lower pressure) in this channel. The overall velocity distribution shows the highest velocity at the hub, decreasing towards the shroud due to the radial equilibrium.

The streamwise vorticity map at this second to last plane shows an interaction of the UVP_3 with the FS_1 vortex. These two co-rotating vortices induce a counter-rotating buffer vortex. This vortex is strong and leads to losses which can be found in the loss map. In the ζ map also losses caused by structure D at the strut suction side and the shroud of channel I can be observed. At the corner SS-strut and hub a flow separation appears. Obviously this FS_2 also leads to losses, which can be observed at the loss map of plane $x_{mid}/C = 1.02$.

To validate the effects of the splitter, the baseline should be compared with the embedded design at plane $x_{mid}/C = 1.02$. Figure 4.4 shows the embedded design and Figure 4.7 gives the contour plots of the baseline.

Comparing the flow separation FS_2 at the baseline with the embedded design, the BL shows a remarkable higher vorticity FS_2 in the baseline case (Figure 4.7(a)). This fact can also be observed when comparing the streamlines of the suction sides of the struts: While the baseline (Figure 4.5(a)) shows a high lift off of the streamlines, the embedded design (Figure 4.5(b)) shows a comparatively low lifting. Obviously this higher lifting of the streamlines has to result in higher losses. These higher losses can be observed when comparing the loss maps of the ED (Figure 4.4, plane

(a) Streamwise vorticity ω_{SW}. (b) Pressure coefficient C_P. (c) Non-dimensional losses $\zeta/\overline{\zeta_E}$.
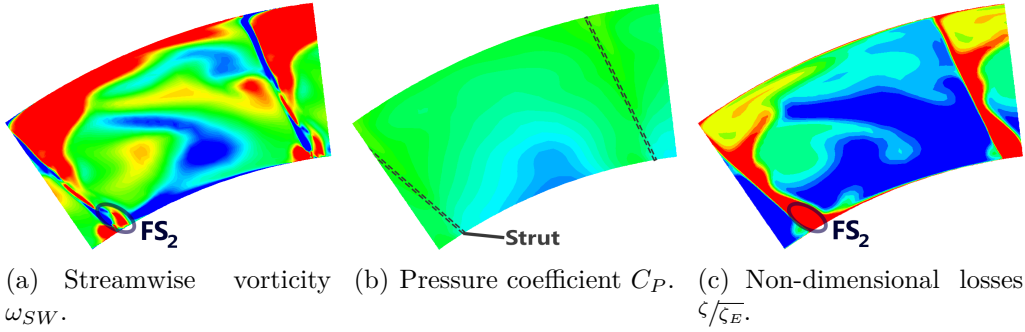
Figure 4.7: Plots of ω_{SW}, C_P and $\zeta/\overline{\zeta_E}$ at plane $x_{mid}/C = 1.02$ of the baseline.
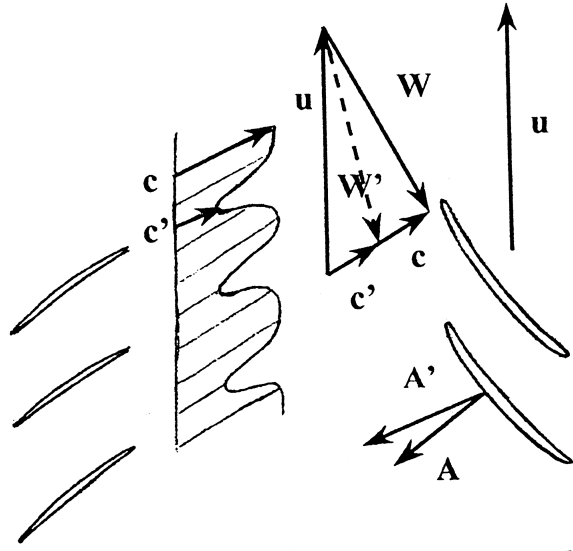
Figure 4.8: Illustration of the influence of a wake at the LP rotor inlet [7].

$x_{mid}/C = 1.02$) and the baseline (Figure 4.7(c)). This effect can also be seen by an oil flow visualization in [19].

The overall distribution of the streamwise vorticity ω_{SW} of the baseline shows clearly the structures of the upstream HP rotor. The BL also shows that the VPV is still turning theses structures. The ED shows no evidence of a turning, hence the VPV was successfully eliminated. The overall distribution of ω_{SW} of the ED design also shows the chopped structures. This will lead to higher fluctuations, but the amplitude is less. This fact will be discussed later in this section.

Smaller wakes have the advantage, that the unsteady influences on the downstream low pressure rotor blades are smaller. This is illustrated in Fig-
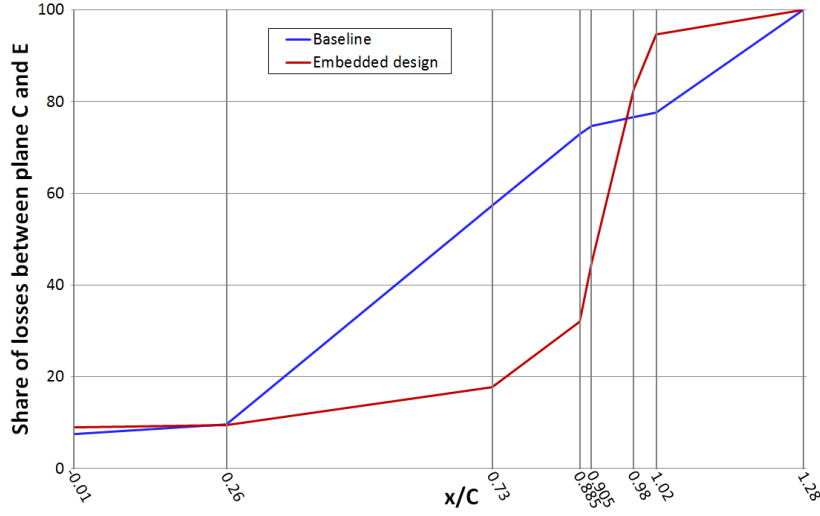
Figure 4.9: Share of non-dimensional losses ζ of the baseline and the embedded design case between plane C and E.

ure 4.8. In this illustration c is the velocity of the free flow and c' represents the smaller velocity of the wake. This smaller velocity leads to a change in the velocity inlet-triangle at the LP rotor leading edge. This change influences the angle of incidence, hence a shift of the stagnation point. Also these fluctuations will likely lead to losses or even flow separations. The illustration in Figure 4.8 is simplified and assumes, that the yaw angle has the same value at every circumferential position. Although this is not the case in this simulation, the statement made is still valid. The distribution of the yaw angle will be discussed later in this section.

The losses map of the baseline in Figure 4.7(c) shows a thick zone at the strut wake, whereas the ED shows three smaller zones. It seems that the losses are relocated and distributed between the three wakes.

In Figure 4.9 the share of the non-dimensional losses ζ between plane C (ζ=0 %) and E (ζ=100 %) is shown. The comparison between the two cases shows that the development of the losses at the begin of the channel (Plane C to about $x/c = 0.3$) is similar, since the influence of the splitters is low. Downstream of plane $x/c = 0.3$ the VPV dominates the development of the losses. Since no other effects affect the evolution of losses within the channel of the baseline, the losses increase more or less constantly up to plane E. The curve of the embedded design shows that the splitters have the highest share of losses. The highest losses are produced between planes $x/c = 0.905$ and $x/c = 0.98$ within the splitter channels. The curve of the embedded design shows that a reduction of the losses within the splitters

will lead to an increase of the efficiency.

Free Flow Behind The TMTF

The main goal for the embedded design was the homogenization of the flow in order to reach a more uniform flow towards the downstream low pressure rotor. To illustrate the advantages and improvements of the splitter design, it is compared to the baseline at plane E. This comparison can be found in Figure 4.10. In this Figure the contour plots (Figure 4.10(a) and (c)) and the radial distribution (Figure 4.10(b)) are given for the yaw angle α, the Mach number Ma/Ma_E, the static pressure coefficient C_p and the non-dimensional losses ς/ς_E. The Mach number and the non-dimensional losses are normalized to their mass-averaged values at plane E. In this case, C_p is calculated with:

$$C_p = \frac{p - \overline{p_E}}{\overline{p_{T,E}} - \overline{p_E}} \tag{4.5}$$

When comparing the contour plots, the first difference are the wakes: While the baseline shows strong evidence of the wakes in every plot, the wakes are hardly visible in the embedded design plots. The losses map of the baseline also shows the vane passage vortex. A main effect are the shed vortices at hub and shroud, which are also visible in the loss map. These shed vortices are the result of an interaction of two neighbouring VPVs. The shed vortex loss at the shroud is superimposed on the loss of the flow separation FS_2. In the loss map of the embedded design the loss of FS_2 is also still visible, but remarkably lower.

The distribution of the yaw angle shows a highly different yaw angle plot comparing the baseline with the embedded design. One reason is the VPV, which influences the yaw angle of the baseline. This is also visible in the radial distribution: The VPV decreases (overturning) the yaw angle close to the hub and increases (underturning) the angle at the shroud. This radial variation of the yaw angle could be considered in the design of the low pressure rotor, but a circumferential variation will lead to wrong incidences, hence to losses. To analyse these fluctuations, the circumferential variation of the yaw angle is given in Figure 4.11.

As discussed before, the yaw angle of the embedded design has higher fluctuations, but a lower amplitude. To quantify this fluctuation, the standard deviation σ has been calculated. For the yaw angle this calculation gives for three span positions (25%, 50% and 75%) 3.7°, 5.0° and 2.5° for the baseline design and 2.8°, 2.8° and 2.5° for the embedded design. The highest difference can be seen at 50% span. σ of the ED is half compared
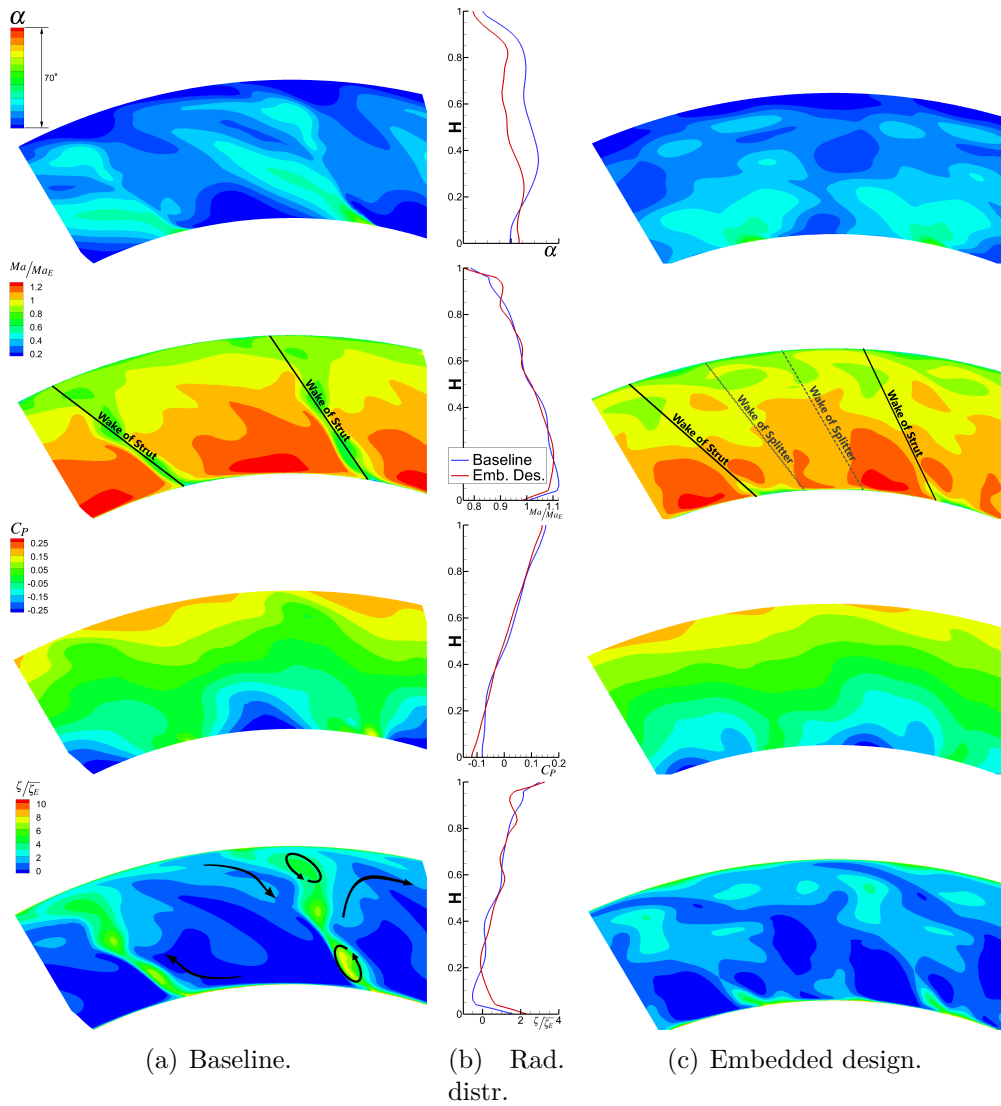
Figure 4.10: Contour plots at plane E ($x/C = 1.28$) downstream of the TMTF.

to the BL and this difference will reduce the losses due to the incidence of the LP rotor. In Table 4.1 the standard deviations of different quantities are listed.

The contour plot of the Mach number also shows clearly the wakes of the baseline. The wake in the plot is formed by the lower velocity which was already mentioned and is illustrated in Figure 4.8. Both contour plots, BL as well as ED, shows areas of highest velocity close to the hub. The standard

(a) 25% SPAN.　　　　　(b) 50% SPAN.　　　　　(c) 75% SPAN.
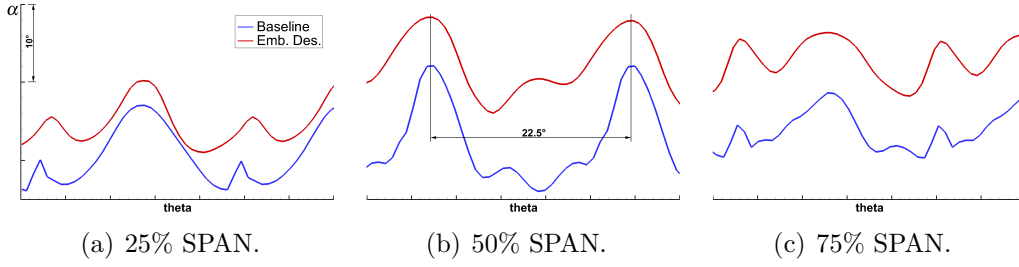
Figure 4.11: Circumferential distribution of the yaw angle α at different span positions.

Table 4.1: Standard deviation of different circumferential values.

	Standard deviation σ					
	Baseline			Embedded design		
Span	25%	50%	75%	25%	50%	75%
Yaw angle	3.7°	5.0°	2.5°	2.8°	2.8°	2.5°
Mach number	0.056	0.043	0.028	0.023	0.019	0.025
Static pressure (bar)	0.0069	0.0062	0.0063	0.0070	0.0068	0.0035

deviations (see Table 4.1) again show lower circumferential fluctuations of Ma_{ED} compared to Ma_{BL}.

The pressure distribution of the ED is more uniform compared to the BL and the three different channels are hardly distinctable. In both cases, the pressure distribution induces a hub to shroud gradient. This gradient will superimpose on the gradient of the second bend located downstream of the S-shaped channel.

The radial distributions of the losses are quite similar, although the embedded design shows higher losses at the hub, while the baseline shows higher losses close to the shroud, where the shed vortex is very active.

In summary these findings show, that the embedded design has a very positive effect on the fluctuations of the flow. The ED homogenizes the flow and successfully passes a more uniform flow towards the downstream low pressure rotor. A negative aspect of the splitters is the higher loss due to the additional blades. In this simulation, the blockage effect was not compensated by endwall shaping. This blocking will likely lead to higher losses. To quantify the losses in the stage an efficiency η_{TMTF} of the TMTF was calculated. This efficiency is calculated with the loss coefficient ζ_{TMTF}:

$$\zeta_{TMTF} = \frac{\overline{p_{t,C}} - \overline{p_{t,E}}}{\overline{p_{t,C}} - \overline{p_E}} \tag{4.6}$$

This calculation compares the loss of total pressure within the duct to the dynamic pressure at plane E. The efficiency η_{TMTF} is calculated with:

$$\eta_{TMTF} = 1 - \zeta_{TMTF} \cdot 100\% \tag{4.7}$$

The resulting efficiencies are $\eta_{TMTF,BL}$= 89.9 % for the baseline design and $\eta_{TMTF,ED}$= 89.2 % for the embedded design. The slightly lower efficiency (higher loss) probably stems from the increased blockage of the splitter blades. It can be expected that the embedded design will lead to less losses if the blockage is considered in the layout of the meridional contour.

4.2   Steady State Simulation

The section before dealt with the influence of the splitters compared to the baseline. This section of the thesis analyses several differences between the used codes as well as the influence of some key parameters. First, a comparison between CFX® and LINARS has been made. This comparison shows the differences of the computed results of the one and the two-stage simulation setup. At the latter part of this chapter, the influence on the results of some parameters has been simulated with LINARS. The influence of

- the mixing length,
- the turbulence modeling method (comparing SA with SST) and
- the transition

on the flow has been analysed. Also in this section measurement data has been used to validate the computed results. Additional information about the measuring method can be found in [64]. The setup of the simulation has already been discussed in Chapter 3.2.

All simulations performed in this section are steady state simulations.

Low Pressure Stage

As already mentioned, first the low pressure stage was simulated. The results of the codes are compared at three different planes: Plane C (Inlet), plane E and plane F. At these positions the radial distribution of Ma, p_{tot}, p_{stat}, T_{tot} and α is given in Figure 4.12. The position of the planes can be observed in Figure 3.1 (Page 32).

Plane C represents the inlet domain. The radial distribution is given in Figure 4.12(a). At this plane, the measured results of p_{tot}, T_{tot} and α have
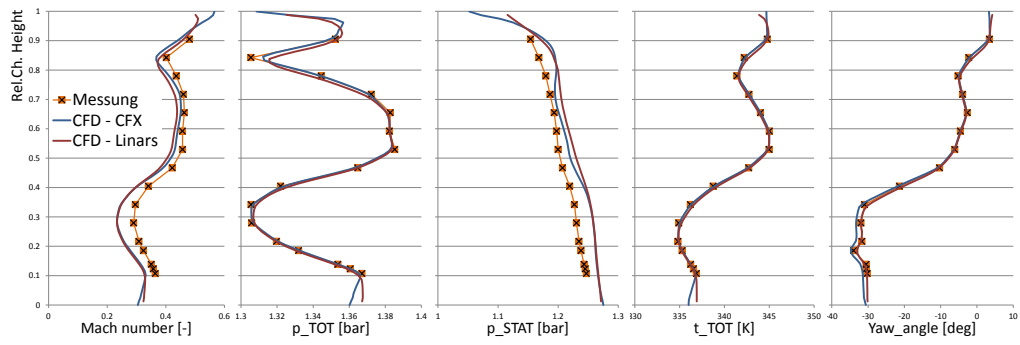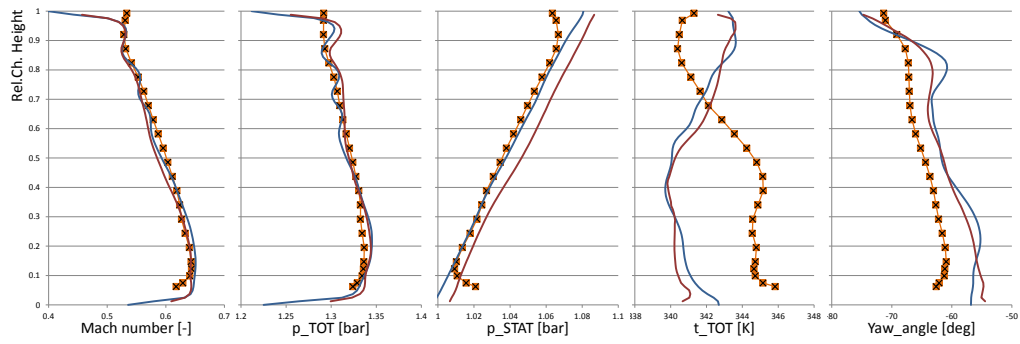
(a) Plane C.

(b) Plane E.
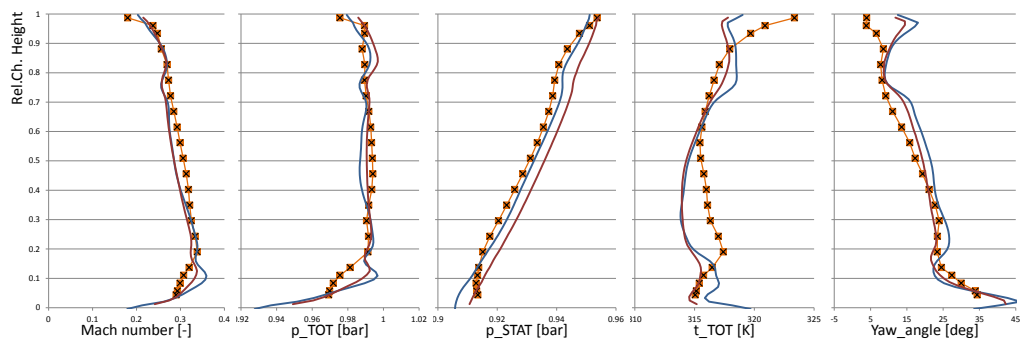
(c) Plane F.

Figure 4.12: Low pressure calculation: Radial distribution of Ma, p_{tot}, p_{stat}, T_{tot}, α at plane C, E and F.

been set as inlet boundary conditions, hence the curves of the computed results are similar to the measured data. The result of Linars shows small differences between the cases. These differences occur, because Linars sets the boundary conditions at ghost cells, which are situated right upstream of plane C. Thus the values at plane C are new values changed between the ghost cell and the first computational cell.

The differences in Ma and p_{stat} are induced by the difference of the mass flow $\dot{m}$. The mass flow in both simulations is lower than the measured $\dot{m}$, hence the velocity is smaller in the simulation, since the flow area is the same. While the measured mass flow is $\dot{m} = 15.5$ $^{kg}/_{s}$, the computed mass flow of CFX® and Linars is $\dot{m} = 14.79$ $^{kg}/_{s}$ and $\dot{m} = 14.48$ $^{kg}/_{s}$, respectively. The smaller velocity leads to a lower Mach number Ma, but a higher static pressure p_{stat}, because the total pressure is the same.

As mentioned, the mass flow of Linars ($\dot{m} = 14.48$ $^{kg}/_{s}$) is slightly smaller than of CFX® ($\dot{m} = 14.79$ $^{kg}/_{s}$). This again leads to different velocities, thus a different static pressure. These small differences can be observed between about $^{r}/_{H} = 0.4$ and $^{r}/_{H} = 0.8$ in the radial static pressure distribution in Figure 4.12(a).

Comparing the graphs at plane E (Figure 4.12(b)) it is conspicuous that the two codes have similar trends. The radial distribution of T_{tot} shows an opposite trend between the simulations and the measurement. Since both codes predict the same trend, it has to be clarified, if the flow setup of the measurement is correct. In this case this has been made with the streamwise distribution of the measured total temperature. The averaged, measured total temperature at plane C is $T_{tot,C} = 339.85$ K and at plane E $T_{tot,E} = 343.39$ K. This means a rise in the total temperature of $\Delta T_{tot} = +3.54$ K. It has to be mentioned, that the total temperature should only rise within a duct, if energy is added to the system. Since between plane C and E neither a sealing, gap or bearing nor a heated wall is installed, this rise of total temperature ΔT_{tot} should not appear. The conclusion of this is, that the measured total temperature has to be doubted.

Another value difference can be observed in the yaw angle α. Both, Linars and CFX® underestimate the deflection of the TMTF compared to the measurement data, CFX® even more at some positions than Linars. A reason for this α difference computed by CFX® could be the result of a different vorticity intensity of the codes. It is conspicuous, that the differences do not cover the whole channel height, but positions, where remains of the HP secondary flows are found. These differences can be observed in Figure 4.13. This Figure shows the flow evolution through the duct with the help of several planes. These planes are extracted at $^{x}/_{C} = -0.02$, $^{x}/_{C} = 0.26$, $^{x}/_{C} = 0.74$ and $^{x}/_{C} = 0.98$. The position of these planes can be

Table 4.2: Relative error of the LP stage simulations at different planes.

	Plane C		Plane E		Plane F	
	CFX®	LINARS	CFX®	LINARS	CFX®	LINARS
Ma	4.55%	6.246%	0.949%	1.142%	0.827%	1.476%
p_{tot}	0.019%	0.070%	0.231%	0.281%	0.007%	0.328%
p_{stat}	0.794%	1.235%	0.140%	0.845%	0.085%	0.526%
α	10.356%	14.779%	5.962%	5.678%	16.699%	6.145%

observed in Figure 3.1 (Page 32). This illustration shows, that the intensity of the streamwise vorticity ω_{SW} simulated by CFX® is higher compared to LINARS. This explains the difference in α.

Figure 4.12(b) shows that LINARS calculates a higher static pressure compared to the measurement data and the computed data of CFX®, respectively. Again, an explanation can be found in the mass flow: As discussed before, $\dot{m}$ of LINARS is lower than $\dot{m}$ of the CFX® solution. Since the total pressure is similar, the static pressure has to be higher, because the velocity c is smaller due to the lower mass flow.

Also plane F (Figure 4.12(c)) shows an aberration in the total temperature between the simulations and the measurement. The CFD solutions have a similar trend as the data of plane E, while the measurement data changes its trend.

Summing up, it is remarkable, that the radial distributions of the two simulations agree quite well, only minor differences can be observed. Both simulations also agree with the measurement data quite well, except the distribution of the total temperature. To qualify the results, Table 4.2 shows the relative errors of the two simulations relating to the measurement. In this table, the total temperature is not listed due to the questionable measurement result. The relative error e_{rel} is calculated with

$$e_{rel} = \left| \frac{\langle x \rangle - \langle x_{Measurement} \rangle}{\langle x_{Measurement} \rangle} \right| \cdot 100\% \qquad (4.8)$$

Table 4.2 shows, that the errors in the pressures are mainly less than 1%, and the errors of the Mach numbers are mainly less than 5%. Due to the different mass flows (discussed above), the Ma error of LINARS is always higher than of CFX®. The differences of the α-errors are relatively high, which can also be explained with the different mass flow, since the axial velocity component which defines the mass flow with $\dot{m} = A \cdot c_{ax}$ also influences the yaw angle (definition of α, see Equation (3.1), page 37). At plane F the errors between the two codes are relatively high compared to the
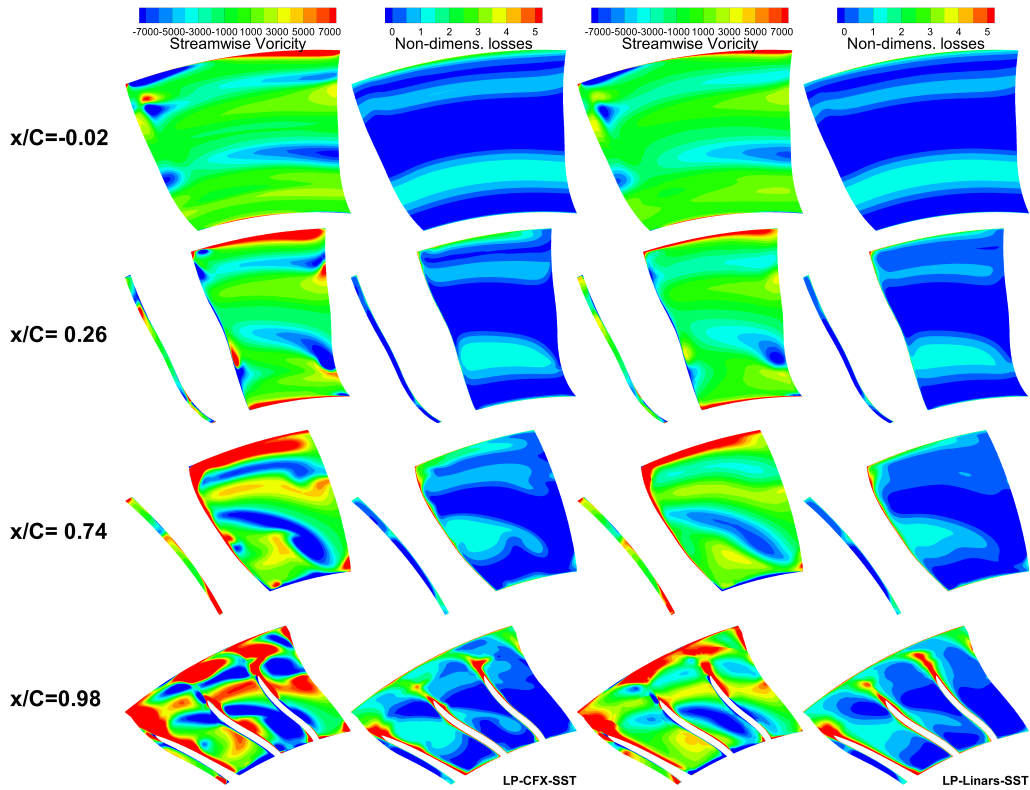
Figure 4.13: LP calculation: Flow evolution differences between CFX® and LINARS of ω_{SW} and ζ.

other planes. This can be explained with the different vorticity intensity, see above.

So far, only the radial distributions have been analysed. To see the mentioned differences of the turbulence modeling, a flow evolution should be discussed. In Figure 4.13 the variation of the three dimensional flow of the two codes can be observed. Since the characteristics of different structures have already been discussed in Chapter 4.1, here only differences between the codes shall be pointed out.

The main difference between the two codes is the intensity of the modelled turbulence, thus the value of the streamwise vorticity ω_{SW}: CFX® calculates a higher ω_{SW} than LINARS, although the turbulence model is the same SST model in both cases. Although CFX® computes the vorticity higher, the non-dimensional losses ζ are quite the same, only slightly higher than in the LINARS calculation.

In Plane $x/C = -0.02$ the LPV from the upstream HP stage can be found clearly. The TLV is pretty weak at the LINARS solution and the UPV is

weak in both cases, but again weaker as the result got with LINARS. The difference in the vortices simulation can also be seen in the turning of the structures: The structures from the LINARS turn less within the passage and that indicates, that the VPV is not as strong as in the CFX® calculation. The differences in turning can be observed at Plane $x/C = 0.74$.

Another difference is visible when comparing the horseshoe legs at the shroud at Plane $x/C = 0.26$ and downstream. CFX® predicts a stronger vortex. Thus, the movement away of the endwall and turning of this boundary layer happens earlier in the duct compared to the LINARS solution.

Generally both codes predict the structures and the behaviour of the flow quite well. Although the LINARS simulation result shows a quite low streamwise vorticity compared to CFX®, the behaviour is still characteristic for the TMTF. It has to be mentioned that it can hardly be said, which vorticity intensity is "right", hence both results can be used to predict the flow evolution through the duct.

Low And High Pressure Stage

In this part, a comparison of the two-stage turbine simulation results is given. Again, the two codes CFX® and LINARS are compared to the measurement. The setup has already been discussed in Section 3.2. Compared to the one-stage setup, two additional planes are added for the comparison: Plane A and B. The inlet boundary is situated at plane A and can be seen together with plane B in Figure 3.1 (Page 32). In plane A and B no measurement results exist, hence in these planes only the two codes can be compared.

As already mentioned, plane A is the inlet plane, hence the distributions are very similar (see Figure 4.14(a)). Small variations of the radial distributions can occur due to the already discussed ghost cells of LINARS. Unlike to the one-stage calculation, the mass flows at the two-stage calculations are very similar, CFX® predicts $\dot{m} = 15.09\ \mathrm{kg/s}$ and LINARS $\dot{m} = 15.14\ \mathrm{kg/s}$. Thus, the averaged velocities at plane A are nearly the same, but differences can be found in the radial distribution of Ma: LINARS computes a higher velocity close to the shroud and a lower velocity close to the hub compared to CFX®.

Plane B (Figure 4.14(b)) is situated between the high pressure stator and rotor and is at the same time the interface between the rotating and stationary frame. The differences between the codes are not significant and the very small differences can again be explained with the small difference in the mass flow. The differences in total temperature T_{tot} are worth mentioning: The decrease in T_{tot} close to the endwalls by LINARS indicates that
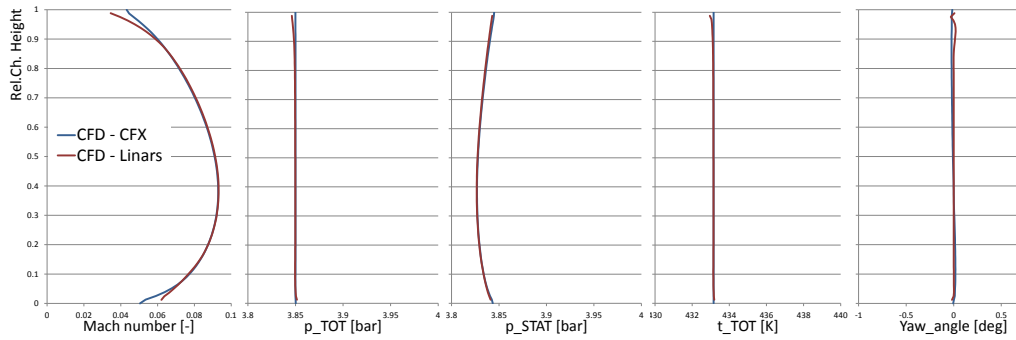
(a) Plane A.
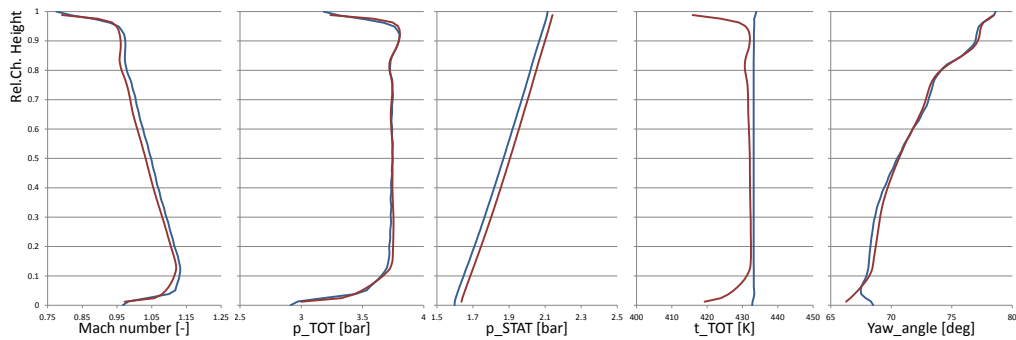
(b) Plane B.

Figure 4.14: Two-stage calculation: Radial distribution of Ma, p_{tot}, p_{stat}, T_{tot}, α at plane A and B.

the static temperature T is not evenly distributed over the channel height, since the dynamic share is quite the same at both codes. Also the yaw angle α is different close to the hub. This allows the conclusion, that the main difference between the codes in this section of the turbine occurs in the boundary layer.

In Plane C (Figure 4.15(a)) the overall trend between the two codes is quite similar. Small differences can be observed in the radial distribution of α, mainly at about $^r/_H = 0.3$ and about $^r/_H = 0.85$. As already mentioned in this work, the yaw angle distribution shows the effect of the secondary flows of the upstream HP rotor. It is remarkable, that the discrepancy in between the codes occur it the position of the LPV and the TLV of the HP rotor, respectively (compare Figure 4.1, page 45). This leads to the conclusion, that CFX® expects a stronger LPV and a stronger TLV. Here it should also be mentioned that the resolution (hub to shroud) of the CFD results is significantly higher than the resolution of the measurement data,
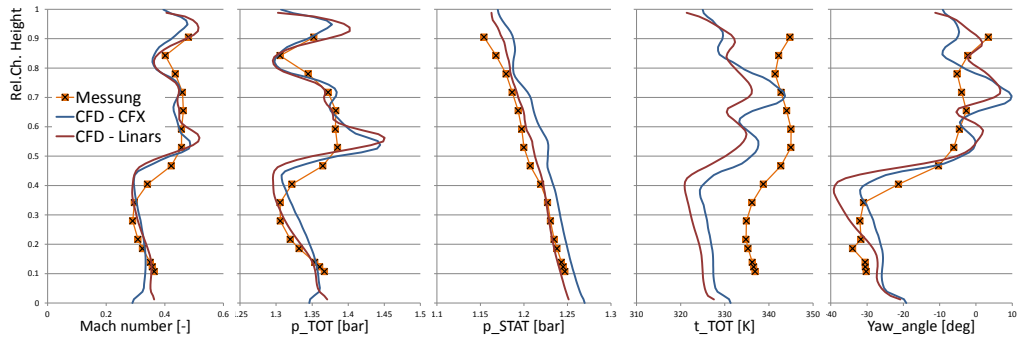
(a) Plane C.
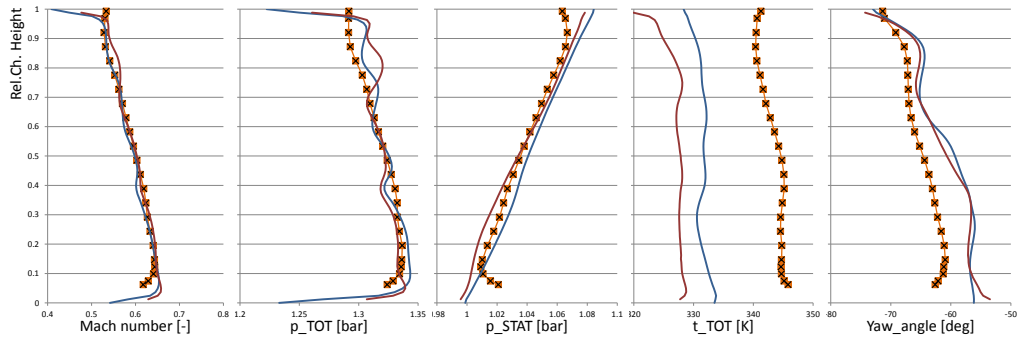
(b) Plane E.
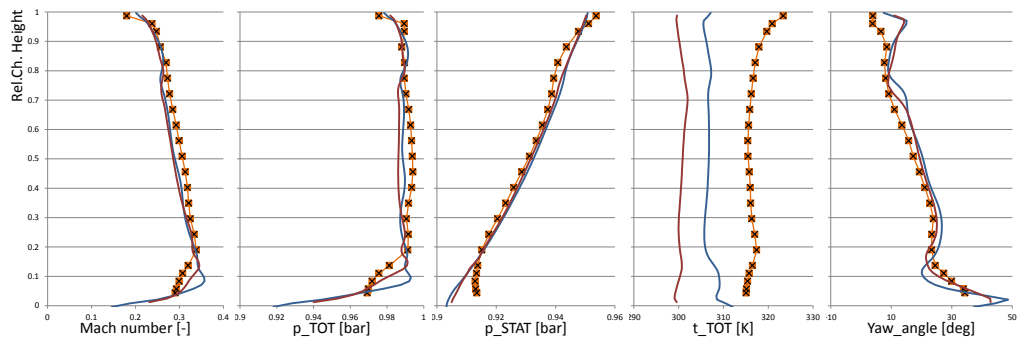
(c) Plane F.

Figure 4.15: Two-stage calculation: Radial distribution of Ma, p_{tot}, p_{stat}, T_{tot}, α at plane C, E and F.
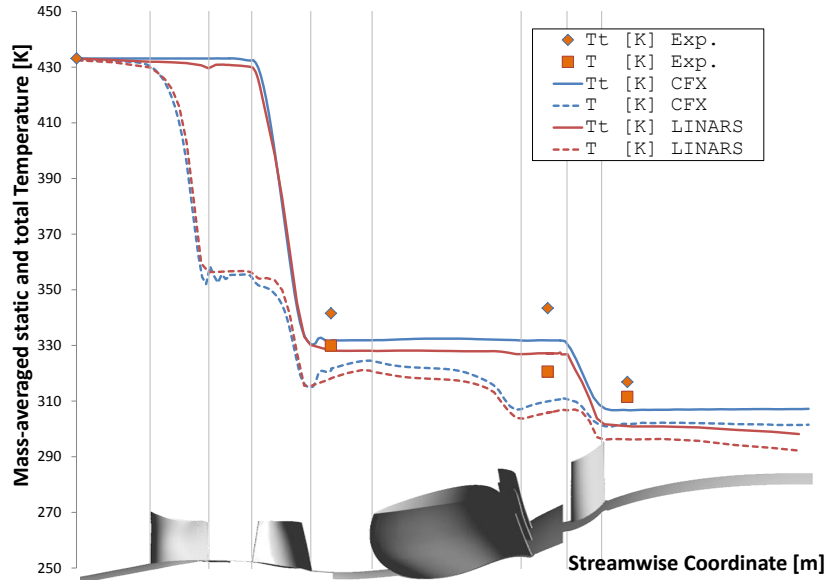
Figure 4.16: Two-stage calculation: Streamwise static and total temperature.

hence not all radial fluctuations could be measured.

Another mentionable fact is, that both codes compute T_{tot} lower compared to the measured data. As mentioned before, the measured data should be doubted in this case, since the total temperature rises in the TMTF. LINARS also expects a lower total temperature at plane C. When looking at T_{tot} at plane E it can be observed, that the radial distributions of the two codes diverge. To analyse this, the streamwise development of the static and total temperature is illustrated in Figure 4.16. Obviously the total as well as the static temperature differ quite strongly between the measurement and simulation as well as between the simulations. Also the rise in total temperature of the measured data can be observed. But this chart also shows, that LINARS computes the total temperature too low, since the total temperature is dropping within the TMTF. As already discussed, this should not happen, since the simulated system is adiabatic. The same trend of the total temperatures can be observed at plane F.

Figure 4.15(b) (Plane E) shows again similar trends between the two codes (except T_{tot}). Interesting is, that both codes underestimate the turning by the TMTF. Since this underestimation is higher at lower radii, this could be the result of an underestimation of the VPV together with the PS to SS gradient at the hub.

Plane F (Figure 4.15(c)) shows a quite good agreement of the radial

Table 4.3: Relative errors of the two-stage simulations at different planes.

	Plane C		Plane E		Plane F	
	CFX®	LINARS	CFX®	LINARS	CFX®	LINARS
Ma	3.220%	0.404%	1.189%	0.759%	1.357%	1.581%
p_{tot}	0.322%	0.069%	0.006%	0.159%	0.091%	0.154%
p_{stat}	1.005%	0.041%	0.515%	0.137%	0.044%	0.045%
α	20.588%	11.928%	6.049%	5.673%	13.178%	9.383%

distribution of α between the simulations and the measurement. Like in plane E, the radial distributions of the other values show similar trends between the three cases.

Generally it has to be said, that the simulation is pretty consistent and similar to the measurement, only the total temperature differs remarkably, due to already mentioned reasons. To qualify the results, the relative error has been calculated and is listed in Table 4.3.

Like in the LP stage simulations, the errors of Ma, p_{tot} and p_{stat} are quite small. The errors in the yaw angle are again quite high, for example the error of CFX® at plane C: The reason is the already described over-estimation of the strength of the LPV and the TLV of the upstream HP rotor. Also LINARS overestimates these vortices, but the error is smaller.

Again the differences of the three dimensional flow should be observed with a flow evolution analysis through the TMTF. Therefore streamwise vorticity ω_{SW} and the non-dimensional losses of the two simulation results are given in Figure 4.17. Additionally to the four extracted plane already mentioned, plane C is also illustrated in the Figure. This plane is situated little upstream of the actual plane C, so the plane is located before the mixing plane. This helps to see structures of the HP rotor more clearly, since these structures would be circumstantially averaged by the mixing plane, or "blurred".

Already the distribution of the streamwise vortices ω_{SW} as well as the non-dimensional losses ζ in Plane C show differences between the CFX® and LINARS result. Mainly at the lower part of the channel, the structures have different positions between the two codes. This leads to the conclusion, that the turning within the HP stage is different. This can be verified with the α distribution in Figure 4.15(a) at page 65. The turning of CFX® is higher compared to LINARS, hence the structures are moved circumferentially at the lower part of the channel, while the position is similar between the codes at higher radii where the turning is very similar. The losses are quite the same, although LINARS expects more losses at the upper part of the

67
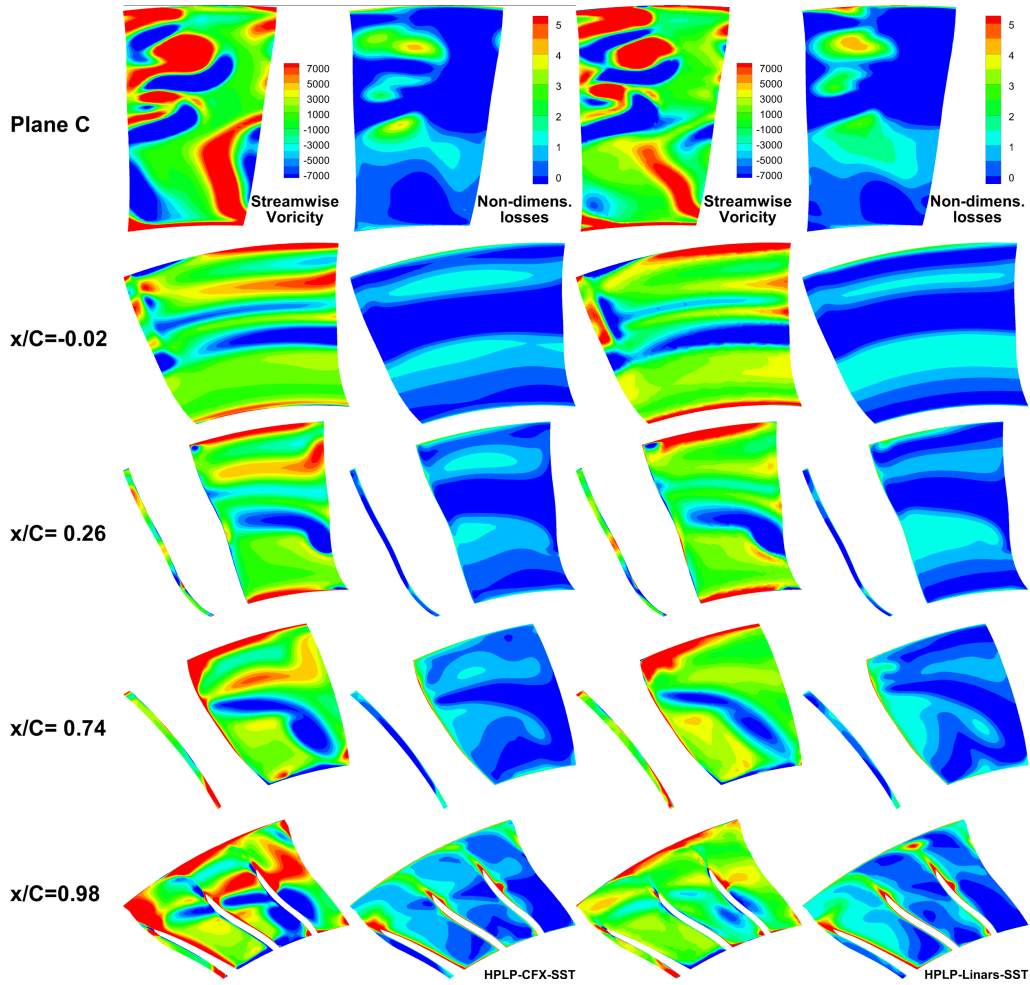
Figure 4.17: Two-stage calculation: Flow evolution differences between CFX® and LINARS of ω_{SW} and ζ.

channel.

Moving downstream into the TMTF ($x/C = -0.02$) is can be observed, that LINARS generally expects less vorticity, but expects a stronger low passage vortex coming from the high pressure rotor as well as a stronger horseshoe vortex SS leg. The reason for the discrepancy is the different turbulence modeling between the codes. While passing the TMTF towards the splitters, the vorticity decay fast in the LINARS calculation. At $x/C = 0.98$ the ω_{SW} differences between the codes are clear: While CFX® has clear structures at this position, LINARS computes weaker vorticity. Although the LINARS result shows much lower streamwise vorticity, the losses are slightly higher compared to CFX®.

Mixing Length

In Chapter 2.2 it has already been pointed out, what different mixing lengths as boundary conditions mean. The ML $l_m = 0.001$ m of the previous simulations has been taken from experience, so it is an empirical value. This section of the work compares different ML to see, what the effect of this value is. The LP stage setup is computed with LINARS and the chosen length-variations simulated are: $l_m = 0.0005$ m, $l_m = 0.001$ m, $l_m = 0.005$ m and $l_m = 0.01$ m.

In Figure 4.18 again the radial distributions at Planes C to F are illustrated. In Plane C (Figure 4.18(a)) the graphs are quite similar. Differences can be observed mainly close to the shroud $r/H > 0.85$, obviously, since the shear stresses are higher close to the endwalls due to the variation of the dissipation. A higher l_m implies a lower dissipation rate. This leads close to the endwalls to a lower total pressure p_{tot} with higher ML.

Figure 4.18(b) (Plane E) shows again a similar trend between the simulations and (except T_{tot} differences, which have been discussed above) the measurement. Variations between the charts can be observed for p_{tot} at $r/H > 0.9$, T_{tot} at $0.3 < r/H < 0.6$ and α at $0.6 < r/H < 0.9$. The variation in the total pressure p_{tot}, respectively is caused by the slower dissipation. A higher ML leads to a lower turbulent kinetic energy (TKE) dissipation rate ϵ, which means, that the eddys need more length to dissipate. Out of $\epsilon \sim 1/\mu_{turb}$ and $\mu_{turb} \sim \zeta$ follows that ζ is higher at higher l_m. To sum up:

$$l_m \uparrow \Rightarrow \ \epsilon \downarrow \Rightarrow \ 1/\mu_{turb} \downarrow \ \text{ or } \ \mu_{turb} \uparrow \Rightarrow \ \zeta \uparrow \tag{4.9}$$

$$\text{Thus: } l_m \uparrow \Rightarrow \ \zeta \uparrow \ \text{ and } \ \zeta \uparrow \Rightarrow \ p_{tot} \downarrow, \ T \uparrow \tag{4.10}$$

In other words this means, that a higher mixing length will increase losses of the flow. These losses will decrease the local total pressure, but will increase the local static temperature, since the losses will dissipate its energy in heat. These conclusions can be confirmed in Plane E (Figure 4.18(b)). The differences between the yaw angles α in the range of $0.3 < r/H < 0.9$ is caused by the differences in the secondary effects. This can be explained with the fact, that different dissipation rates influence the duration (or dissipation speed) of these secondary vortices coming from the upstream HP rotor. The different duration of the dissipation influences the strength and size of the vortices leaving the passage.

In Plane F (Figure 4.18(c)) again differences can be observed in p_{tot}, T_{tot} and α.

This quick overview about the influences of the mixing length boundary condition shows, that the change of the radial distribution is not huge, but l_m has an influence on the flow, so that it should be set correctly.
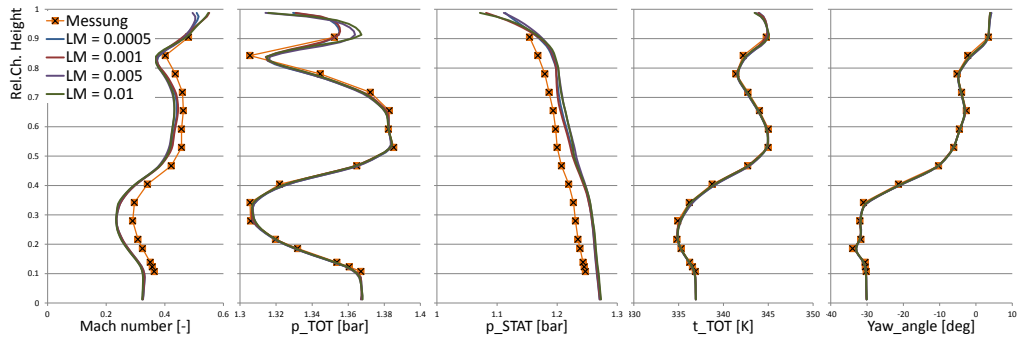
(a) Plane C.
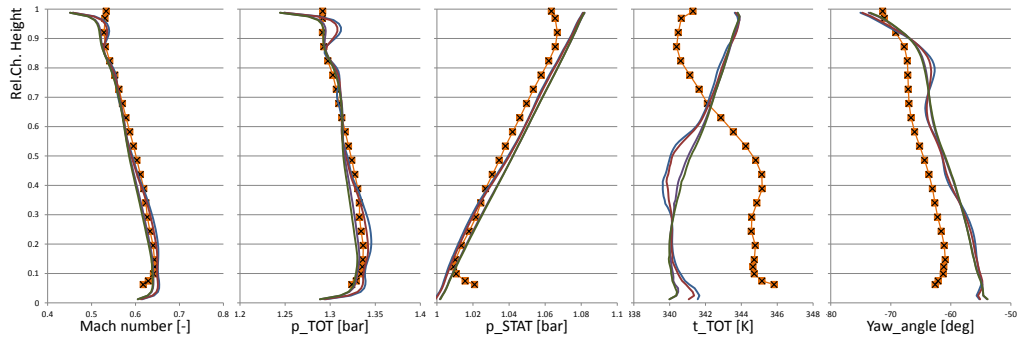
(b) Plane E.
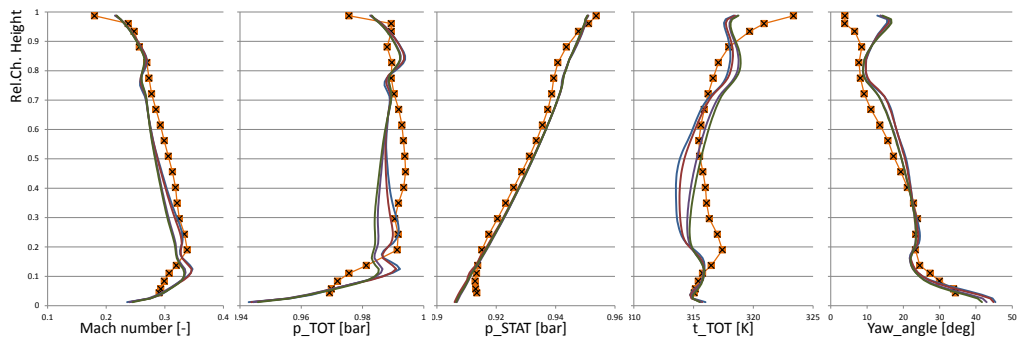
(c) Plane F.

Figure 4.18: Mixing length calculation: Radial distribution of Ma, p_{tot}, p_{stat}, T_{tot}, α at plane C, E and F.

70

Table 4.4: Relative errors of the SA/SST comparison simulations at different planes.

	Plane C		Plane E		Plane F	
	SA	SST	SA	SST	SA	SST
Ma	5.042%	6.246%	3.373%	4.865%	5.387%	7.013%
p_{tot}	0.070%	0.070%	0.502%	0.429%	0.053%	0.341%
p_{stat}	0.982%	1.235%	1.085%	1.932%	0.577%	1.200%
α	14.463%	14.779%	2.654%	3.193%	6.815%	14.256%

Spalart Allmaras (SA) vs. Shear Stress Transport (SST)

In this section the two turbulence models *Spalart Allmaras* (SA) and *Shear Stress Transport* (SST) are compared. The theory behind these two turbulence models was described in Section 2.2. Both calculations in this section were computed with LINARS and the LP-stage setup is used. As already mentioned, the turbulent boundary conditions are a mixing length of $l_m = 0.001$ m and a turbulent intensity of 10%.

In Figure 4.19 the radial distributions of Ma, p_{tot}, p_{stat}, T_{tot}, α at the different planes are illustrated. In Plane C (Figure 4.19(a)) the graphs are very similar, since the influence of the turbulence model is not big at the inlet plane. The small observable differences can be explained once again with differences in the mass flow. Comparing these two flows shows, that the SA calculation has a slightly higher $\dot{m} = 14.87$ kg/s compared to the SST calculation with $\dot{m} = 14.48$ kg/s. The influence is again visible in the radial distribution of Ma and p_{stat}, respectively.

More differences can be observed in Figure 4.19(b). The SST model overestimates the static pressure p_{stat} in this plane E, while the results of the SA model correspond with the data of the measurement quite well. An interesting point is the diagram of the yaw angle: The SA model shows less dissipation and better transports the vortices of the HP stage between plane C and E. This fact can be seen at the dents at $r/H = 0.25$, $r/H = 0.4$ and $r/H = 0.8$. These dents represent the transported LPV, UPV and TLV of the HP rotor.

Plane F (Figure 4.19(c)) has the same differences in p_{stat} like Plane E between the SA and the SST model. In the graph of the yaw angle α it can be observed that the SA model overestimates the turning of the LP rotor. Again, the relative errors have been calculated. The results are summed up in Table 4.4.

In this case it is more important that the errors between SA and SST
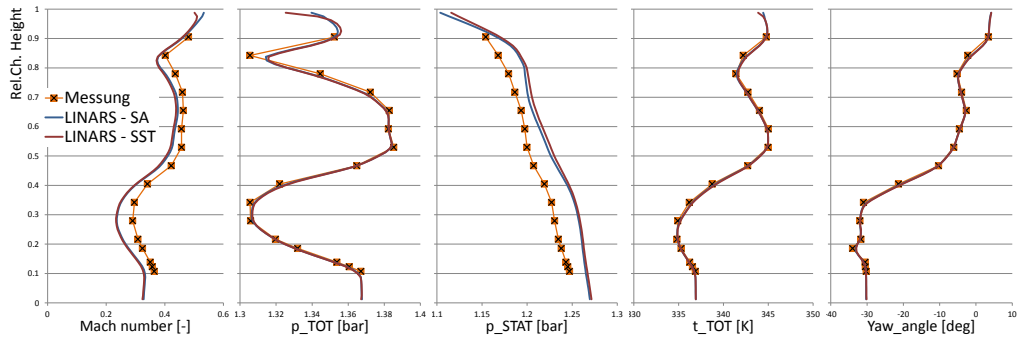
(a) Plane C.
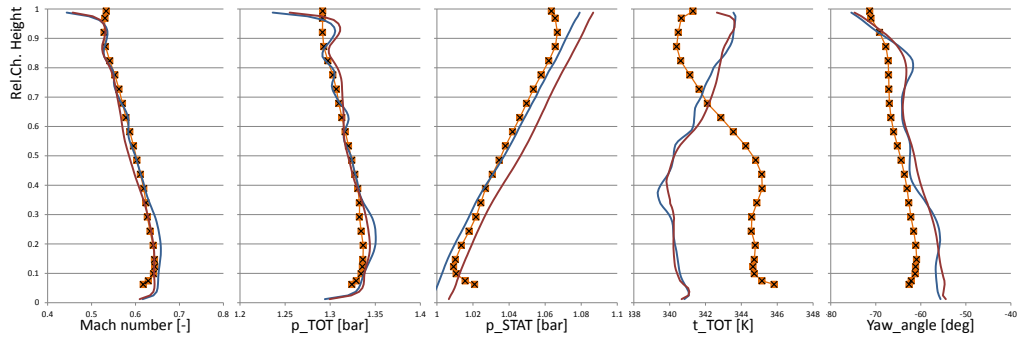
(b) Plane E.
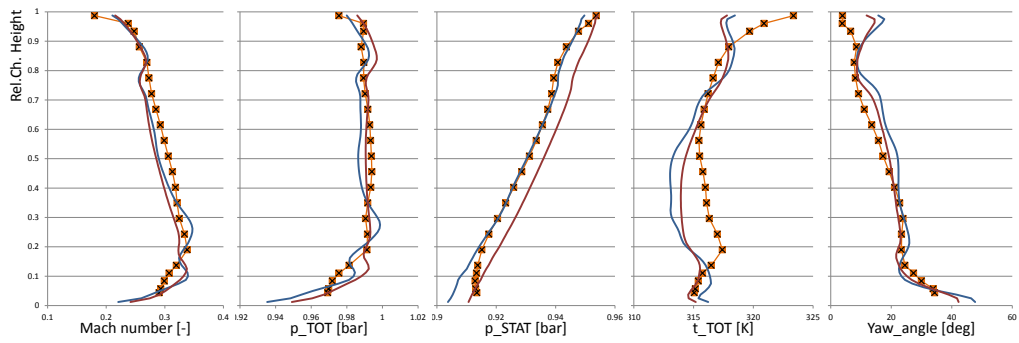
(c) Plane F.

Figure 4.19: SA vs. SST calculation: Radial distribution of Ma, p_{tot}, p_{stat}, T_{tot}, α at plane C, E and F.
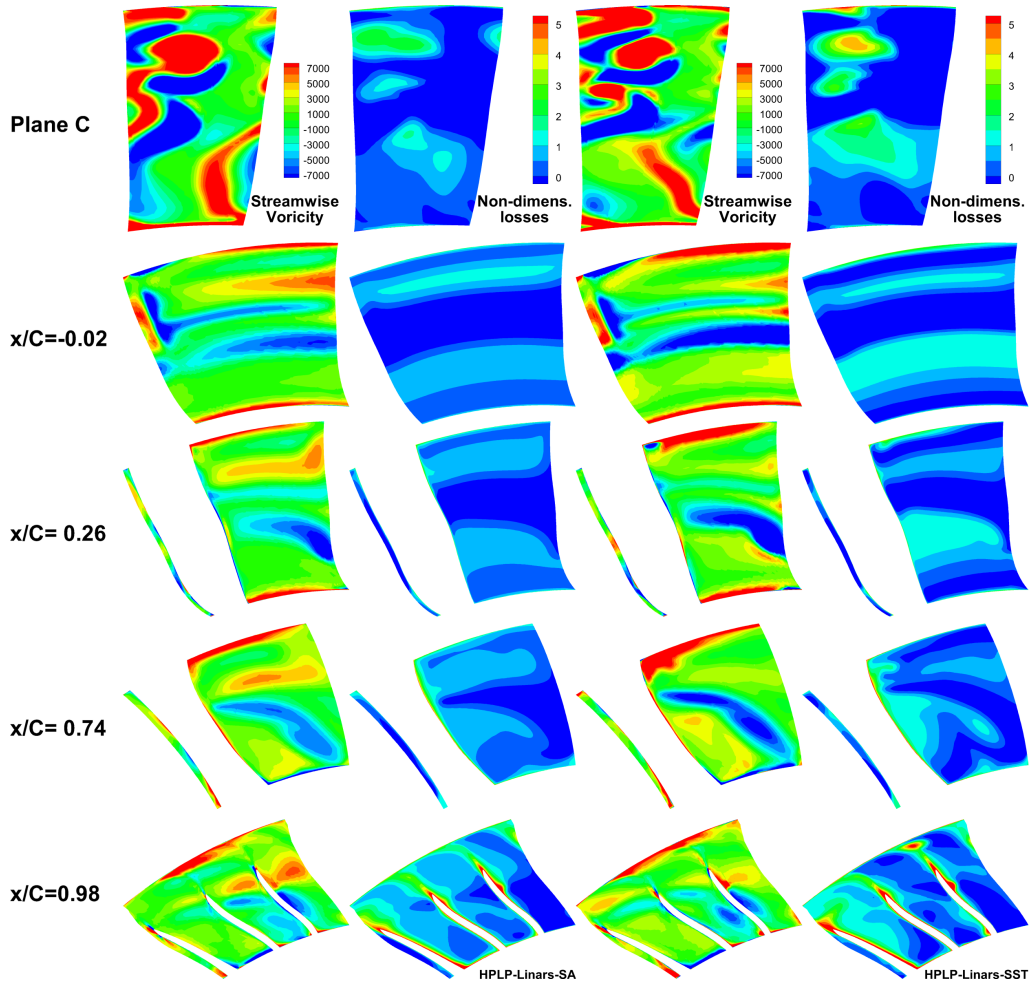
Figure 4.20: Flow evolution differences between the SA and the SST model of ω_{SW} and ζ.

are quite similar. The absolute values have already been compared earlier in this thesis. Comparing the errors of the two different simulations shows, that the differences are very little. The biggest difference shows the error of the yaw angle at plane F.

Overall, the differences in the radial distribution between the *Spalart-Allmaras* and the *Shear Stress Transport model* are small, although some deviations can be observed. Thus, the flow evolution through the TMTF should be discussed. In Figure 4.20 the changes of the streamwise vorticity ω_{SW} and the non-dimensional losses ζ (Equation (4.3) and (4.4) on page 46) are plotted.

Already at plane C differences between the turbulence models can be

observed at the contour plots. The LPV coming from the upstream rotor is turned and more separated for the SST model due to a interaction and mixing of the lower and upper passage vortex. The SA modeling leads to a well-observable distribution of LPV, UPV and TLV. The non-dimensional losses ζ of the SST model are also higher compared to the SA model. This indicates, that the velocity gradients a higher, which results in a higher ω_{SW}.

At the following planes it is interesting to see, that the clockwise rotating vortices (blue) are more strongly developed for the SST model. On the other hand the counter-clockwise rotating vortices (red) are weaker. A reason for this could be that the vane passage vortex (also clockwise rotating) is stronger developed in the SST model calculation. At the last two planes at $x/C = 0.74$ and especially at $x/C = 0.98$ this different intensity of the VPV can be observed, since the transported vortices are turned less through the TMTF by the SA turbulence model.

Another difference between the models can be seen in the boundary layer. As discussed in Chapter 2, the SST model produces too much turbulence in areas, where already shear stress exists, thus the model generates too much turbulence close to the endwalls. This effect can be observed mainly at the shroud wall: While the SA calculation only shows low vorticity, SST computes more streamwise vorticity which results in higher losses.

Transition

As described in Section 2.2, it is important to analyse the boundary layer since it has a major influence on the drag of the profiles, and thus an impact on losses. In this section, the influence of transition modeling should be discussed. Also an illustration of the boundary layer behaviour is given in this part of the thesis. The two-stage turbine is calculated with LINARS. The differences between a simulation with and without transition of the high pressure stage can be observed in Figure 4.21 and of the low pressure stage in Figure 4.22.

In Plane A the inlet distribution can be observed. Obviously no differences can be observed, since the boundary layer just starts developing at this point (Figure 4.21(a)). In Plane B already small differences in the Mach number Ma and the static pressure p_{stat} can be seen (Figure 4.21(b)). These differences show a higher velocity in the stage, when the calculation is done with transition. The reason is, that the calculation with transition leads to a higher mass flow $\dot{m}$. Computing with transition leads to a mass flow of $\dot{m}_w = 15.27$ kg/s while the calculation without transition leads to a mass
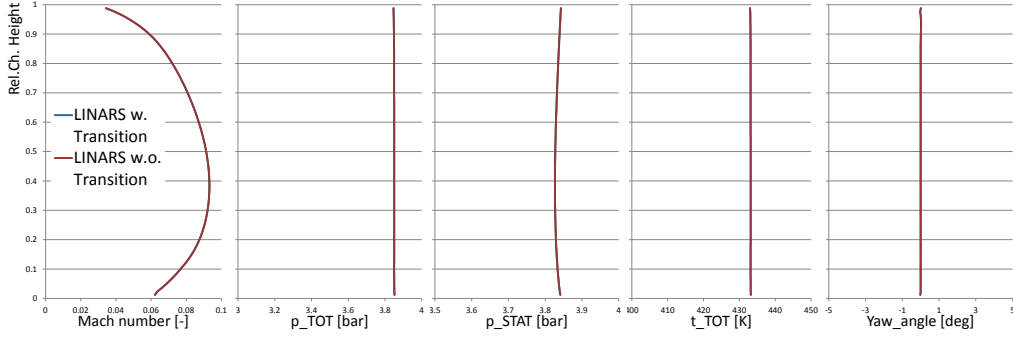
(a) Plane A.
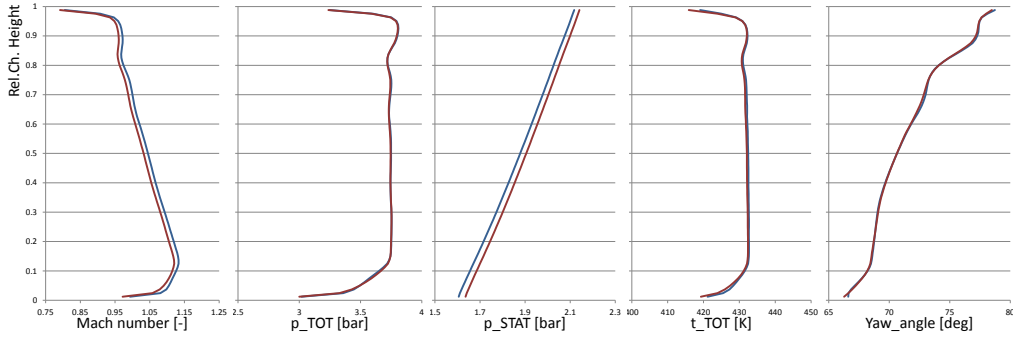
(b) Plane B.

Figure 4.21: Transition calculation: Radial distribution of Ma, p_{tot}, p_{stat}, T_{tot}, α at plane A and B.

flow of $\dot{m}_{wo} = 15.16$ kg/s. The differences in the mass flow are likely the result of different friction losses or drag within the stages.

When comparing the differences of T_{tot} between plane B and C (Figure 4.22(a)), it seems that with transition slightly less energy was converted in the HP rotor. To quantify this assumption, the isentropic efficiency η_{is} can be calculated with the equation

$$\eta_{is} = \frac{T_{tot,B} - T_{tot,C}}{T_{tot,B} - T_{tot,C,is}} \tag{4.11}$$

The temperatures in Equation (4.11) are illustrated in Figure 4.23. The Temperature $T_{tot,B}$ and $T_{tot,C}$ as well as the pressures $p_{tot,B}$ and $p_{tot,B}$ are taken from the simulation as mass-averaged values at the Planes B and C, respectively. With the equation

$$\frac{T_{tot,C,is}}{T_{tot,B}} = \left[\frac{p_{tot,C}}{p_{tot,B}}\right]^{\frac{\kappa-1}{\kappa}} \tag{4.12}$$

75
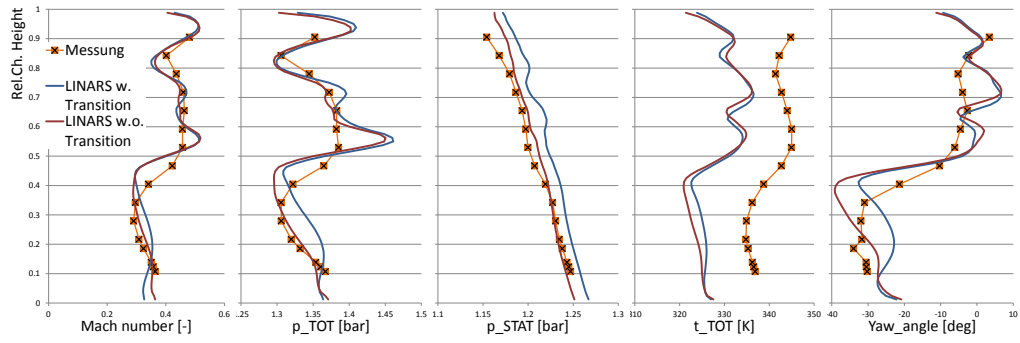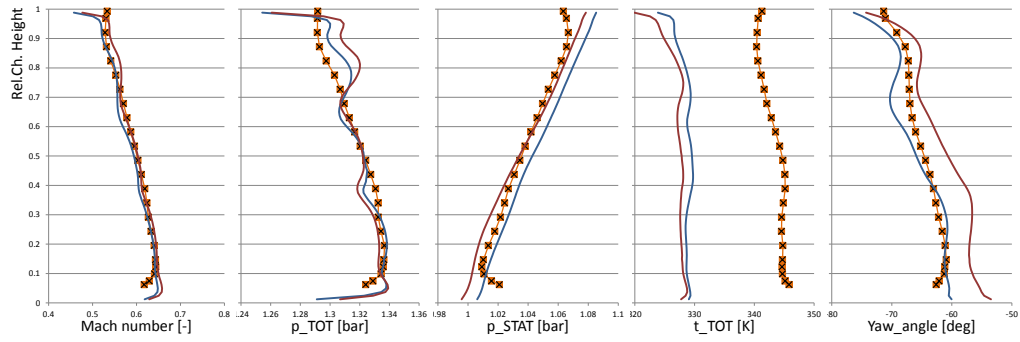
(a) Plane C.

(b) Plane E.
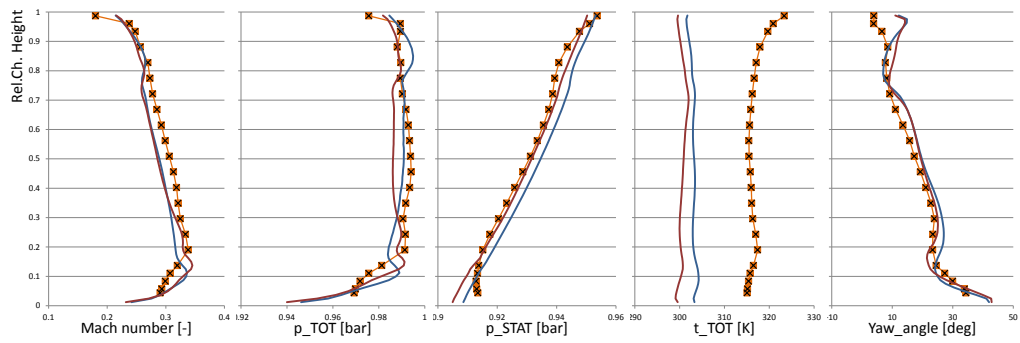
(c) Plane F.

Figure 4.22: Transition calculation: Radial distribution of Ma, p_{tot}, p_{stat}, T_{tot}, α at plane C, E and F.
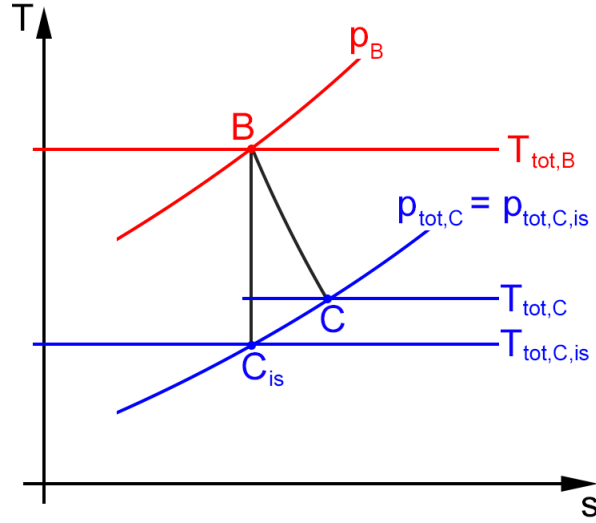
Figure 4.23: An illustration of an isentropic and an polytropic state change through the HP rotor.

an isentropic state change can be calculated with $\kappa = 1.4$. With this equation, the isentropic temperature $T_{tot,C,is}$ can be calculated for both cases:

$$T_{tot,C,is} = T_{tot,B} \cdot \left[\frac{p_{tot,C}}{p_{tot,B}} \right]^{\frac{\kappa-1}{\kappa}} \tag{4.13}$$

$$T_{tot,C,is,wo} = 356.647 \text{ K} \cdot \left[\frac{135639.2 \text{ Pa}}{371013.2 \text{ Pa}} \right]^{\frac{1.4-1}{1.4}} = 267.535 \text{ K} \tag{4.14}$$

$$T_{tot,C,is,w} = 355.721 \text{ K} \cdot \left[\frac{136145.8 \text{ Pa}}{371368.6 \text{ Pa}} \right]^{\frac{1.4-1}{1.4}} = 267.051 \text{ K} \tag{4.15}$$

To calculate the isentropic efficiency, the values $T_{tot,C,wo} = 318.014$ K and $T_{tot,C,w} = 319.543$ K are necessary. By inserting these two values into Equation (4.11) η_{is} can be calculated:

$$\eta_{is,wo} = \frac{356.645 \text{ K} - 318.014 \text{ K}}{356.645 \text{ K} - 267.535 \text{ K}} = 0.433 \tag{4.16}$$

$$\eta_{is,w} = \frac{355.721 \text{ K} - 319.543 \text{ K}}{355.721 \text{ K} - 267.051 \text{ K}} = 0.408 \tag{4.17}$$

This calculation shows, that the calculated efficiency of the HP turbine is higher without the activated transition. Since the overall change Δp_{tot} and the isentropic efficiency η_{is} of the transition simulation is lower, the energy transferred to the spool is lower in this case. This fact can also be observed

Table 4.5: Relative errors of the transition comparison simulations at different planes.

	Plane C		Plane E		Plane F	
	with	w/o	with	w/o	with	w/o
Ma	0.174%	0.404%	4.755%	3.036%	7.370%	7.112%
p_{tot}	1.026%	0.069%	0.631%	0.551%	0.131%	0.140%
p_{stat}	1.103%	0.041%	1.802%	0.940%	1.036%	0.716%
α	26.012%	11.928%	3.930%	3.188%	10.838%	11.640%

in the flow turning of the fluid through the stage. High differences in α at the lower part of the channel ($r/h < 0.45$) show, that the transition leads to a reduced turning within the HP rotor. The reason for this can be observed in Figure 4.24 and is explained later in this section.

After passing the TMTF (Plane E), p_{tot} shows another trend compared to plane C (Figure 4.22(b)): While at plane C the total pressure is similar, only differences at $r/h < 0.45$ can be observed, plane E shows also differences at $r/h > 0.8$. These differences indicate a change of the redial pressure distribution while the averaged pressure is similar. On the other hand, the simulation without transition underestimates the turning by the TMTF.

At Plane F (Figure 4.22(c)) the flow angles as well as the total pressure are quite similar. That means, that the flow turning $\Delta\alpha_{EF}$ between the planes was again underestimated by the simulation without transition. Also since T_{tot} was lower at plane E in the transition case, again less energy was extracted through the LP rotor.

Again, the relative errors are calculated to quantify the differences between the two simulations. These errors are listed in Table 4.5.

The main differences are observable for the yaw angle at plane C. This difference also leads to the difference in the efficiency calculated above.

More or less, all the differences observed between these two simulations occur in the lower part of the channel and mainly in the passage between Plane B and Plane E. To see the behaviour of the boundary layer, the Intermittency γ is illustrated in Figure 4.24 as a contour plot a mesh cell layer above the HP and TMTF hub and blade faces. If $\gamma = 0$ (blue contour), the boundary layer is fully laminar. A $\gamma = 1$ (red contour) represents a fully turbulent BL. The values between 0 and 1 represent the transition between the laminar and turbulent BL.

The differences in turning and energy extraction discussed above between Plane B and Plane C can be observed at the hub and blade of the high pressure rotor. The reason is the highly changing boundary layer: Several
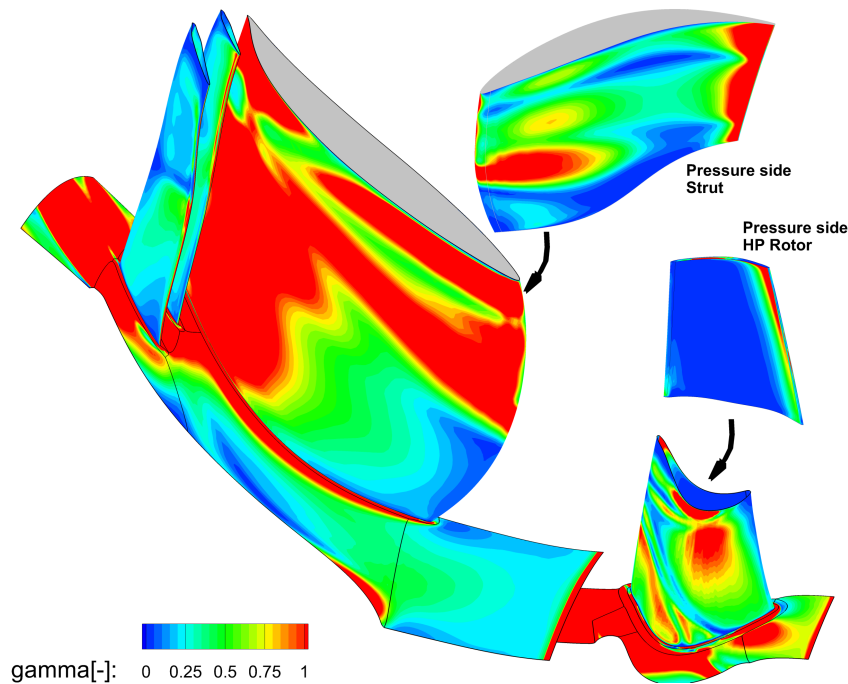
Figure 4.24: The γ-value as contour-plot at the HP and TMTF hub and blade faces.

times the BL gets fully turbulent but also returns to a laminar boundary layer. This reverse development of the layer is called relaminisation. This seesaw of the BL state leads probably to the higher losses and lower energy extraction discussed above in this section.

The differences in the yaw angle α between the two simulations in Plane C is the result of the highly different boundary layers at the suction and pressure side: While the BL at the PS is hardly turbulent, the SS shows a turbulent and often changing BL. This will result in different boundary layer thicknesses which influence the yaw angle. Figure 4.25 shows an illustration of this process. The BL at the pressure side is thicker compared to the BL at the SS. This will lead to a change of the flow angle, from c to c'.

The reason, why the differences mainly occur at lower relative heights is visible at the strut: While in the upper part of the channel, the boundary layer close to the leading edge is fully turbulent, the development of a fully turbulent layer takes much longer in the lower part of the suction side. Also at the pressure side of the strut, the boundary layer is more laminar, close to the hub nearly along the whole span.
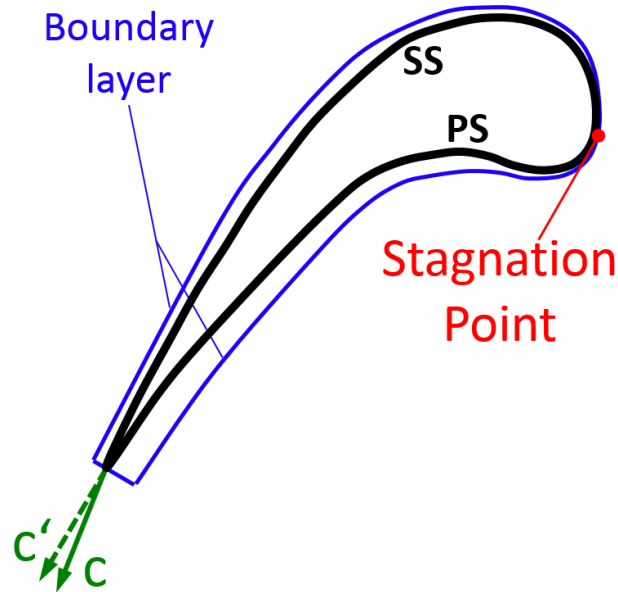
Figure 4.25: The influence of the boundary layer thickness on the deviation/yaw angle.

4.3 Unsteady Simulation

The last section of this chapter deals with the unsteady simulation of the two-stage turbine. The simulation was performed with LINARS. The main target of the unsteady simulation is to observe the influences of unsteady fluctuations, for example rotor-stator interactions.

Figure 4.26 and 4.27 illustrate such fluctuations. In these charts the fluctuations of the averaged p_{tot} and α, respectively, are plotted at specific planes over the rotation angle. These graphs show the mass-averaged values at specific planes and describe the fluctuation of these two values over the time. In both cases, the fluctuations at plane C have the highest amplitude (see Figures 4.26(a) and 4.27(a)). These high amplitudes are the result of large structures coming from the upstream HP rotor. The frequency of the fluctuations corresponds with the blade passing frequency of the rotor.

At plane E (Figures 4.26(b) and 4.27(b)) the amplitudes are much lower. A reason is that the strong structures of the HP rotor are decaying and are chopped by the splitters. This leads to a reduction of the losses of the downstream LP rotor compared to the baseline case without splitter, since the baseline setup would not chop the structures, hence would not damp the amplitude. The graph at plane E also shows that a lower frequency
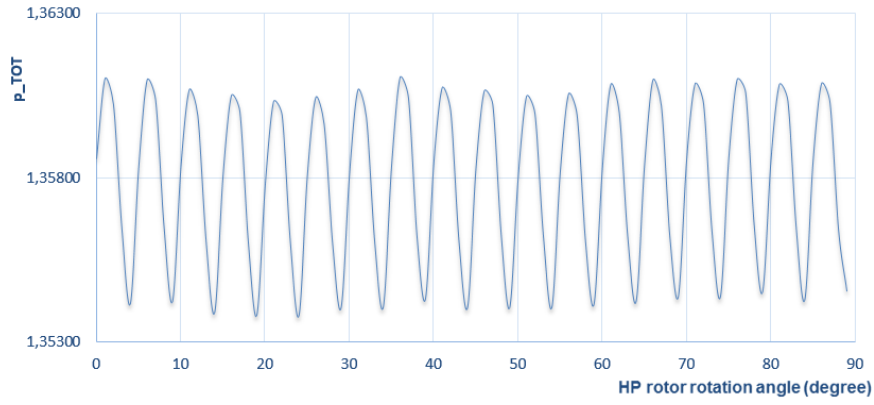
(a) Plane C.
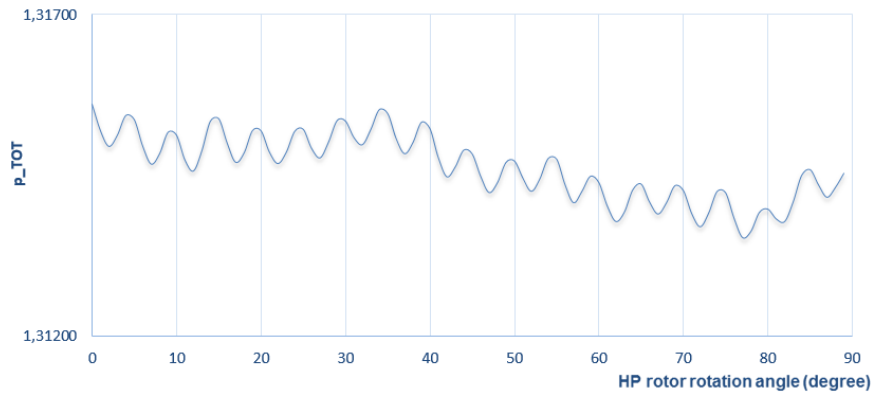
(b) Plane E.
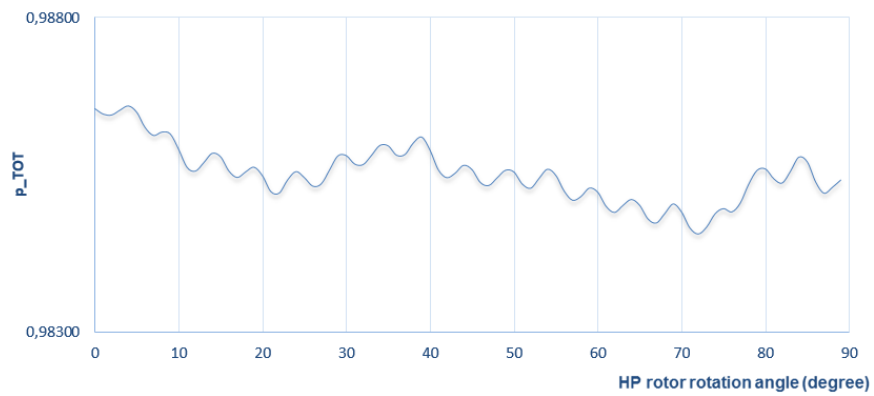
(c) Plane F.

Figure 4.26: Mass flow-averaged total pressure p_{tot} plotted over rotation angle at different planes

81
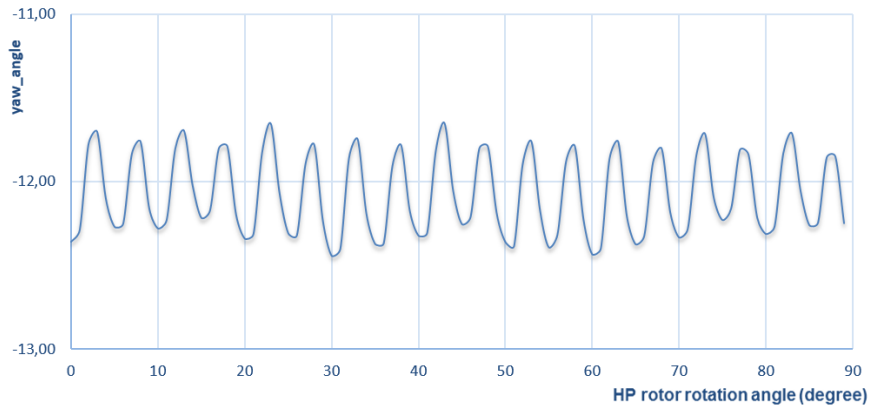
(a) Plane C.
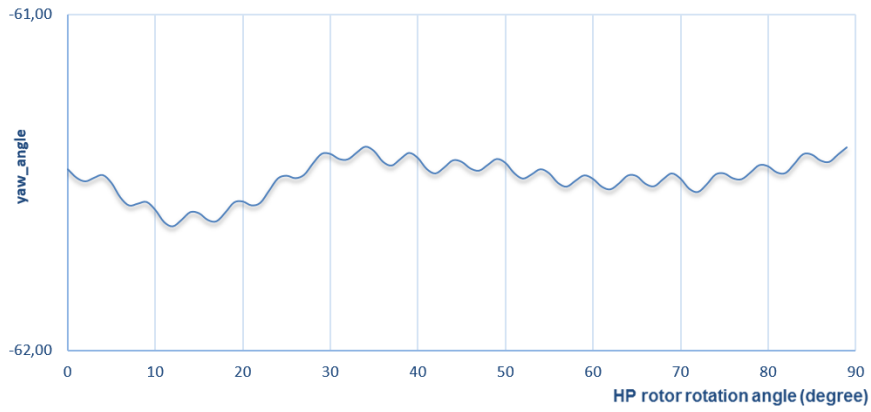
(b) Plane E.
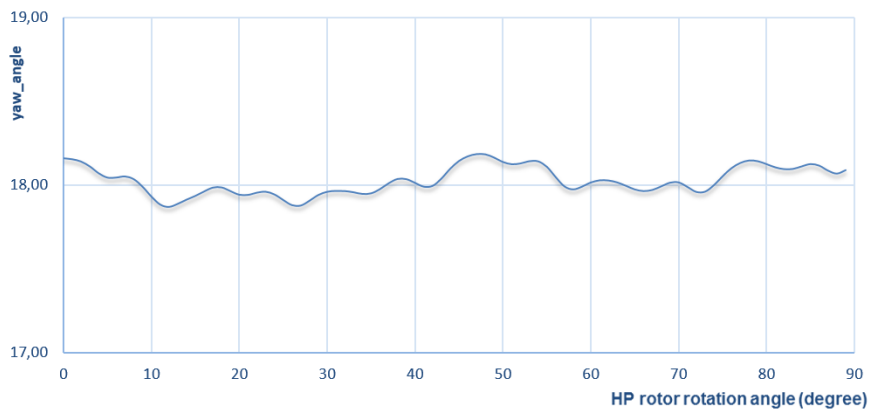
(c) Plane F.

Figure 4.27: Averaged yaw angle α plotted over rotation angle at different planes

superimposed with the high frequency of the HP rotor. This low frequency is the result of the VPV.

The graph at plane F (Figures 4.26(c) and 4.27(c)) shows quite the same trend as Plane E, but the amplitudes have been reduced due to friction and dissipation.

Overall it can be said, that the unsteady effects of the HP rotor are reduced and the flow to the subsequent LP rotor is homogenized and most important, the amplitudes are reduced.

In the following several selected contour plots are discussed. The figures show eight contour plots at different time steps. Between the plots a HP rotation angle of $\Delta\omega = 3°$ has been chosen. This angle has been calculated with equation

$$\Delta\omega = \frac{P_\mathrm{TMTF}}{n} \tag{4.18}$$

where P_TMTF is the pitch angle between two struts and n is the number of desired pictures. Inserting values into Equation (4.18) results

$$\Delta\omega = \frac{22.5°}{8} \tag{4.19}$$

$$= 2.81° \approx 3° \tag{4.20}$$

This means that the HP rotor travels 24° which covers approximately one pitch of the TMTF (22.5°). Generally it can be said that the differences between the TMTF channels at one timestep are mainly caused by the HP stator, since the pitch of the TMTF struts and the HP stator blades do not have the same denominator. Differences between the timesteps are caused by the HP rotor.

The first illustration shows the pressure gradient $|\delta\vec{p}/\delta\vec{x}|$. The contour plots of the pressure gradient (Figure 4.28) show clearly the shocks ranging from the HP stator to rotor. This shock causes a deceleration of the fluid from supersonic to subsonic speed. The Mach number contour plot shows this transition to $Ma < 1$ (see Figure 4.29). The shock is stationary since it is caused by the HP stator. The passing leading edge of the HP rotor interacts with this shock. If the shock hits the LE, the shock is reflected. This unsteady reflections lead to a change of the velocity at the HP stator suction side and can be observed at the Mach contour plot in Figure 4.29. The pressure gradient plot in Figure 4.28 also shows a high $|\delta\vec{p}/\delta\vec{x}|$ value at the HP rotor trailing edge. This indicates a high pressure difference between the suction and pressure side.

The Mach number contour plot (Figure 4.29) shows differences between the two displayed TMTF channels: Splitter B at the upper channel shows

a spot of low Ma while the Splitter B at the lower channel does not show such a spot. As mentioned before, these differences are caused by the HP stator.

The Mach number plot also shows time variations of the velocity within the duct. This fluctuation is also present behind the struts, which is better observable at plot 4.30.

Figure 4.31 shows the contour plot of the streamwise vorticity ω. The plot clearly shows the vortices at the wakes of the high pressure stator. These structures are transported through the high pressure rotor where they are superimposed by the secondary effects of the high pressure rotor. The effects of the HP stator are still observable downstream of the HP rotor, so the HP stator has a high influence on the flow field at plane C. One unsteady effect generated by this flow field are the fluctuating horseshoe vortexes at the strut leading edge (compare LE at different t_{step} in Figure 4.31). Another effect caused by the HP stator can again be observed when comparing the two channels: The upper displayed channel has a clearly stronger vorticity structure (blue) compared to the lower channel. This stronger structure leads to an incidence change of the flow approaching the splitters. Thus, mainly the splitter B (upper splitter) shows a stronger structure (red) which will reach the low pressure rotor, while at the other illustrated channel this structures behind the TMTF dissipate faster.

To see the differences between the steady and unsteady simulations, Figure 4.32 shows the same position and values as Figure 4.31, but for the steady state simulation (also LINARS result). The differences between the simulations are obvious and should be discussed in the following. First, the vortices behind the HP stator are clearly resolved in the unsteady, but are wiped out in the steady-state simulation. Both simulations show that the structure with negative vorticity ω_{SW} (blue) is stronger that the positive one (red). The mixing plane B (between HP stator and rotor) of the steady simulation averages the structures hence they are not observable behind the mixing plane. The averaging leads to a constant vorticity (light blue zone) behind the plane. A similar trend can be observed at the mixing plane behind the HP rotor. The wakes of the HP rotor are also wiped and not so clear compared to the unsteady simulation. In this case the mixing plane also averages all values and so structures are not observable behind the mixing plane. The result is again a structure with circumferentially constant vorticity behind plane C. Although the structures are not clearly visible in the steady-state simulation, the averaged values are similar to the values in the unsteady simulation. Within the duct of the TMTF, the dominant blue structure is similar between the two simulations.

Comparing the structures at the splitters, the zones are quite similar,

although their intensity is not. The steady-state simulation expects the counter-clockwise rotating structure (red) at the "suction" side of the 2nd splitter (upper splitter) will dissipate faster. Thus this structures will not reach the low pressure rotor in the steady-state simulation and obviously the fluctuations at this rotor are lower due to the mixing plane. The clockwise rotation structure (blue) between the two splitters as well as the counter-clockwise rotating structure (red) between the strut SS and the first splitter are computed stronger by the steady-state simulation.

Generally, the steady state simulation gives a good result and it shows similar structures compared to the unsteady simulation but to see and understand the fluctuations and the rotor-rotor interactions it is indispensable to analyse the flow with an unsteady simulation.

Figure 4.33 illustrates a blade-to-blade contour plot of the entropy at 50% span. The plots show a different entropy evolution between the TMTF channels illustrated. A different entropy indicates different losses within the channels. As mentioned before, such differences between the channels are caused by the HP stator. Thus the HP stator blades also affects the losses of the TMTF channel. Figure 4.33 also shows different losses between the splitters. The highest loss is produced by splitter B of the upper channel. The losses are highly fluctuating and unsteady.

At 90% span (Figure 4.34) the flow separation of splitter B as discussed in Chapter 4.1 is visible in the entropy. At different timesteps a different intensity of the FS can be observed.

As discussed before, the high pressure stator has a big influence on the subsequent domains. To analyse the structures caused by the HP rotor and stator, respectively, the unsteady results in the planes B (between the HP rotor and stator) and C (downstream of the HP rotor) are illustrated at Figures 4.35 and 4.36. The total pressure p_{tot} in Figure 4.35 shows three more or less "green" spaces at plane B. They are caused by the wake of the HP stator. Between these zones alternating "red" and "orange" spots are visible. The "orange" p_{tot} spots (lower pressure) are caused by the reflection of the shocks (see Figure 4.28). Downstream of the HP rotor at plane C the effects of the rotor and stator can be separated with help of the pitch: The illustrations represent an angle of 45°. Within this angle three vane blades and four and a half rotor blades are placed, hence three and four wakes, respectively, can be found in the plots. The three wakes of the stator are clearly visible at plane B. At plane C this fact can be used to understand which structure is triggered by the rotor or stator. At the lower left corner of Figure 4.35 these structures are marked. Four blue structures (low pressure) at the shroud (4x TLV), four blue structures at the hub (4x LPV) and three red structures at the mid of the channel. The three red

spots of higher pressure are caused by the stator, and are superimposed by the UPV, since the UPV leads to a higher p_{tot}. The correlation between the structures (TLV, UPV, LPV) and the pressure distributions have already been discussed in Chapter 4.1 and is illustrated in Figure 4.1.

Figure 4.36 shows again the three wakes of the vane blades at plane B. At plane C the mixing and shifting caused by the high pressure rotor is visible. The structures caused by the HP stator which are visible are turned by the rotor and interact with the secondary effects of the HP rotor. At plane C four and a half wake zones are visible. An interesting change can be observed at the hub: While plane B shows clockwise rotating structures (blue), plane C shows counter-clockwise rotating structures (red) close to the hub. A similar change can be found at the shroud. These changes are likely induced by the pressure gradient at the endwalls caused by the pressure gradient suction to pressure side.

To illustrate the unsteady influences of the flow on the low pressure rotor the flow behaviour at plane E is discussed. Figure 4.37 shows the contour plot of the entropy. This plot shows the loss core generated by the flow separation at the hub-strut SS corner as analysed in Chapter 4.1. Also differences of the losses between the channels can be observed. These differences are also visible at the blade to blade plot in Figure 4.33 and have already been discussed.

At plane E the streamwise vorticity is also illustrated in Figure 4.38. Again, the flow separation at the strut suction side is clearly visible and also differences between the channels can be observed.
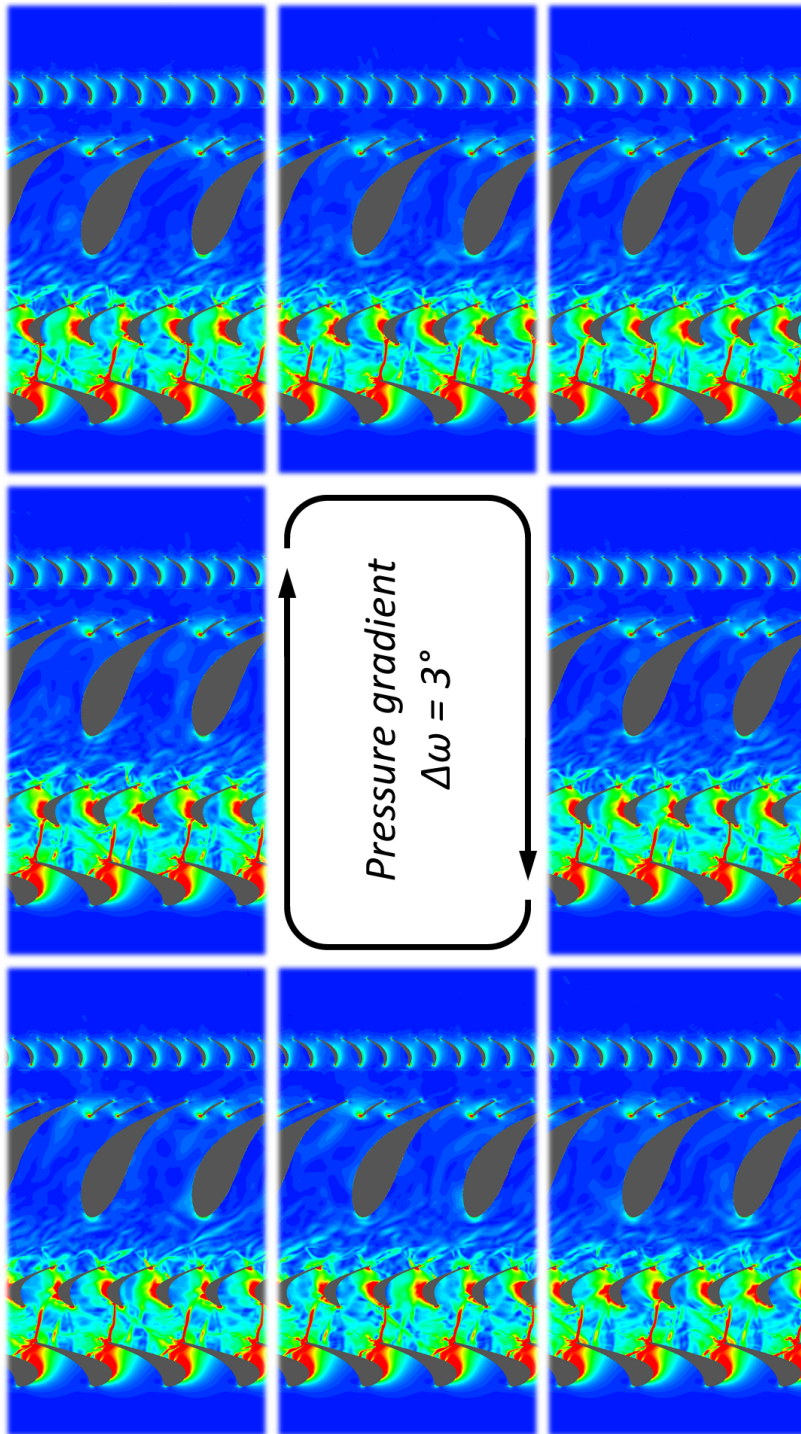
Figure 4.28: Blade to Blade contour plot of the pressure gradient at 50% span.
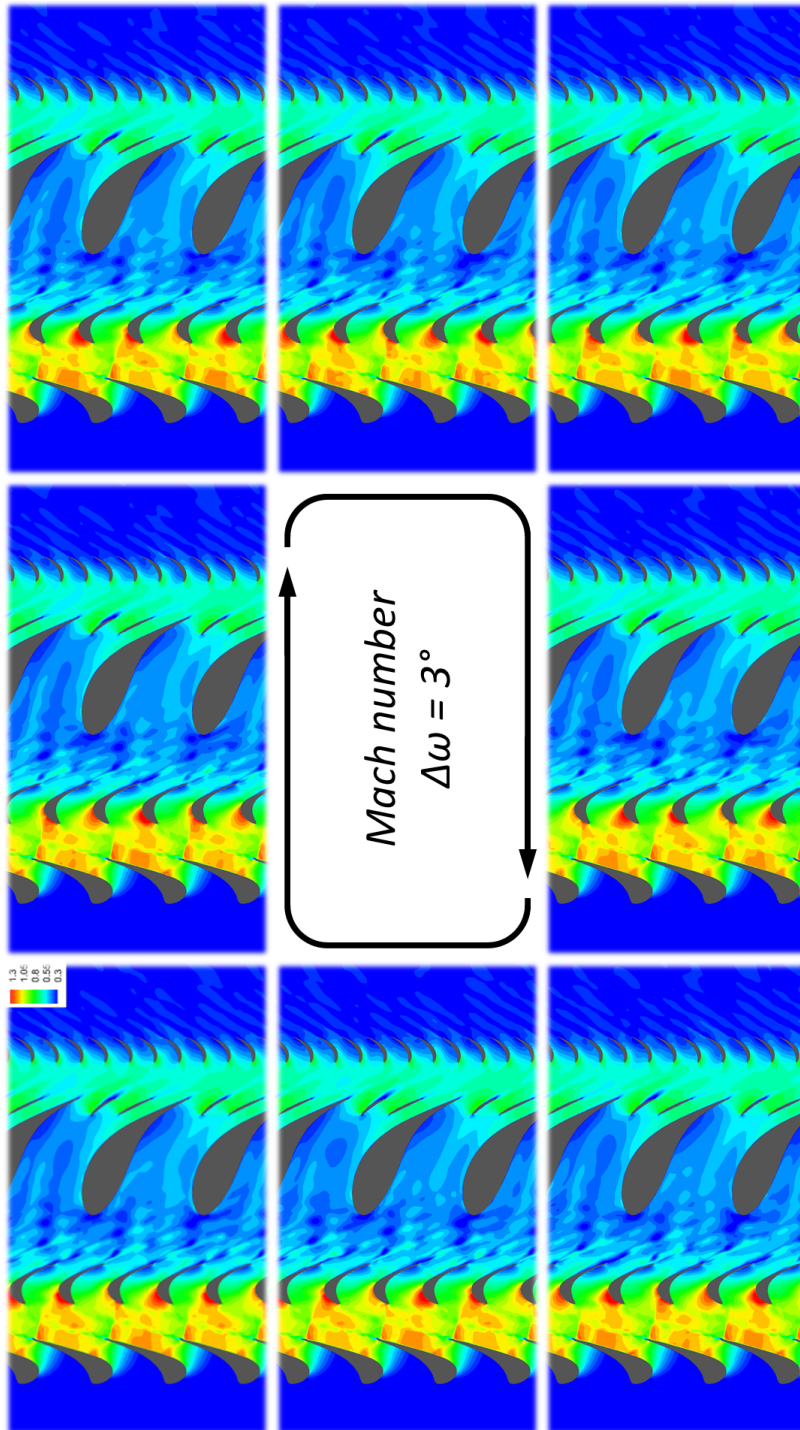
Figure 4.29: Blade to Blade contour plot of Mach number at 50% span.
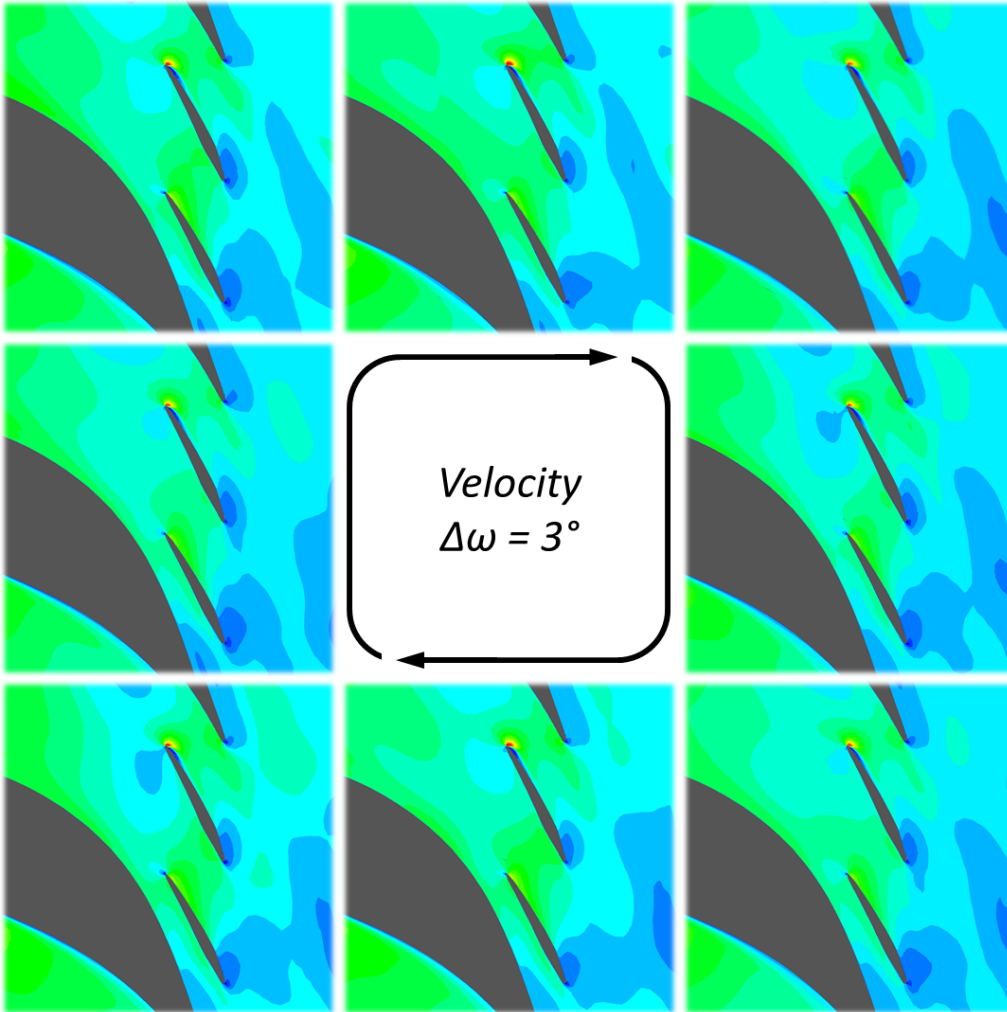
Figure 4.30: Blade to Blade section of the splitters - velocity contour plots.
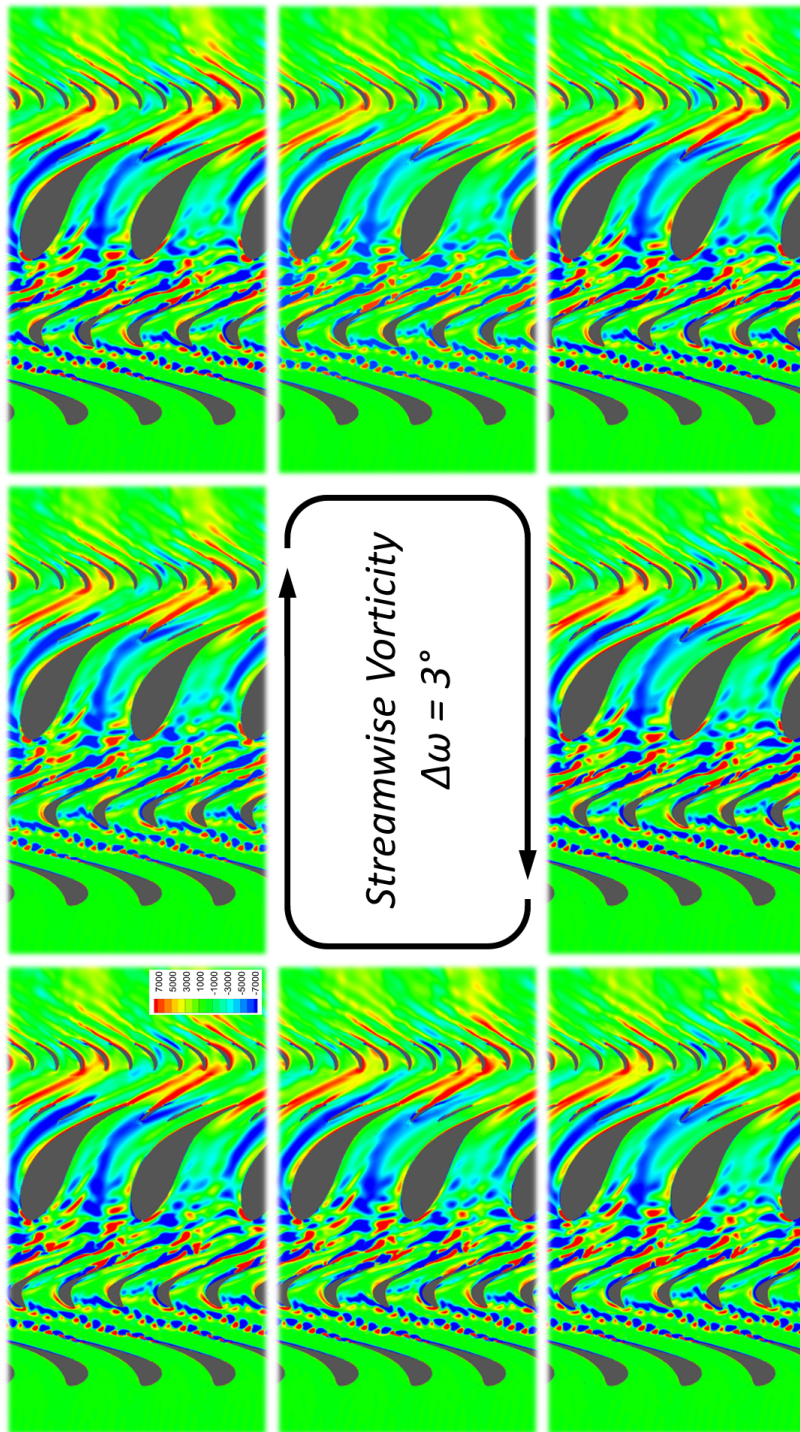
Figure 4.31: Unsteady Blade to Blade contour plots of the streamwise vorticity at 50% span.
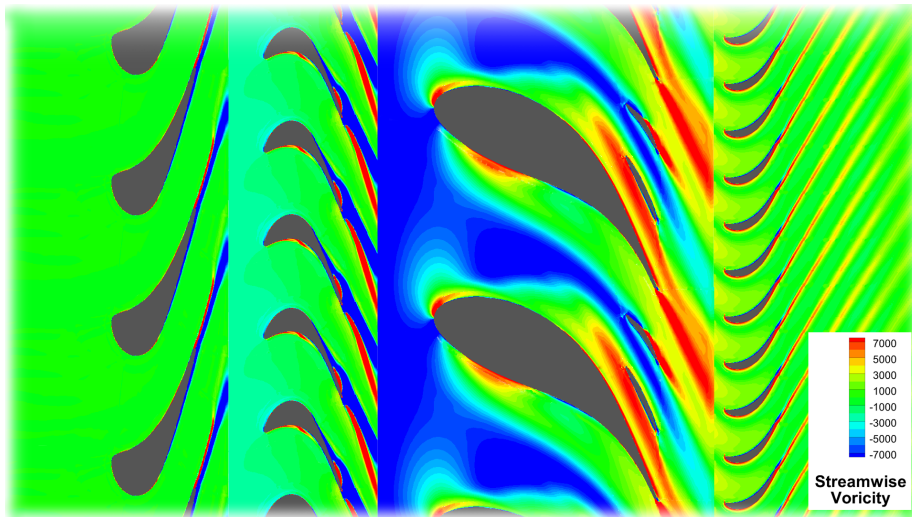
Figure 4.32: Steady Blade to Blade contour plot of the streamwise vorticity at 50% span.
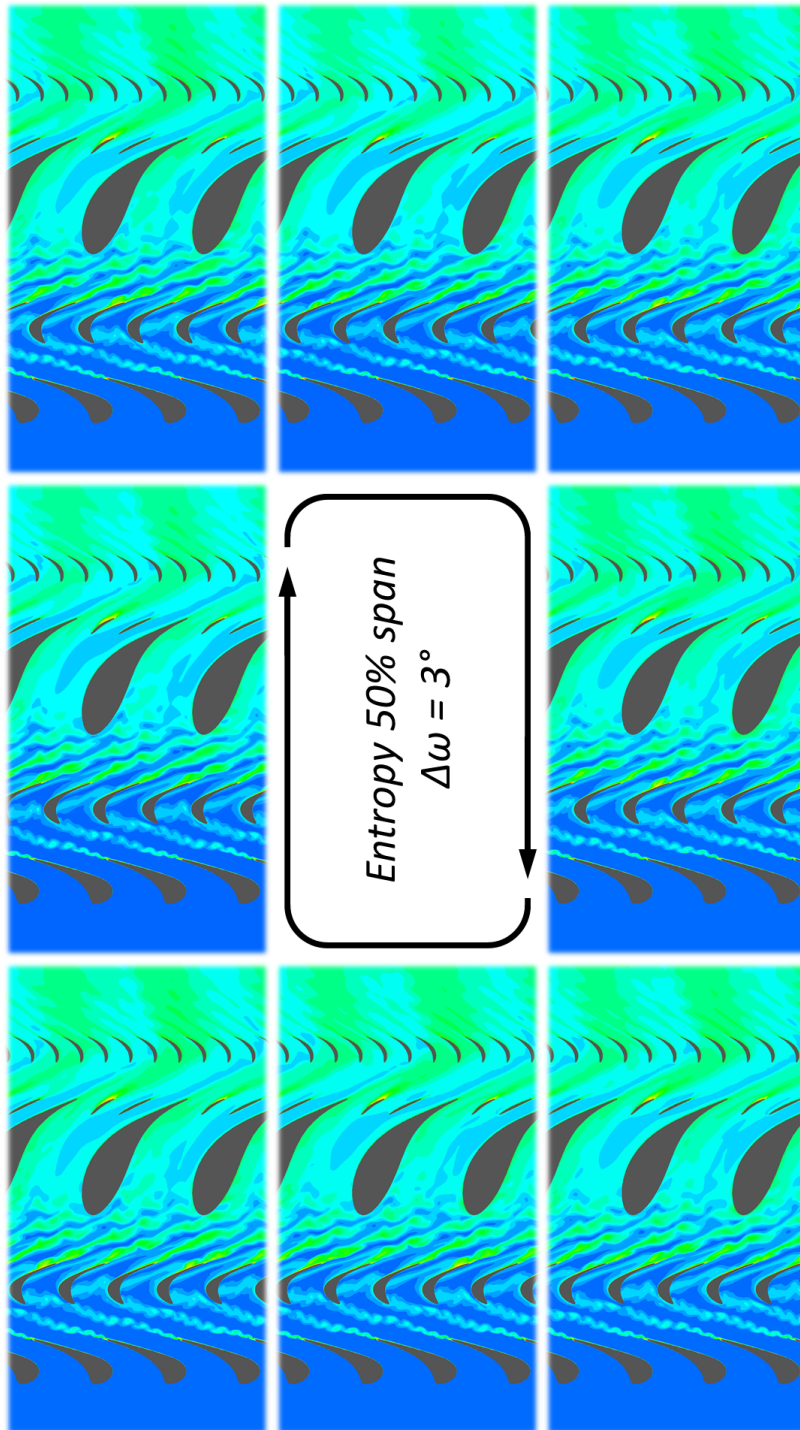
Figure 4.33: Unsteady Blade to Blade contour plots of entropy at 50% span.
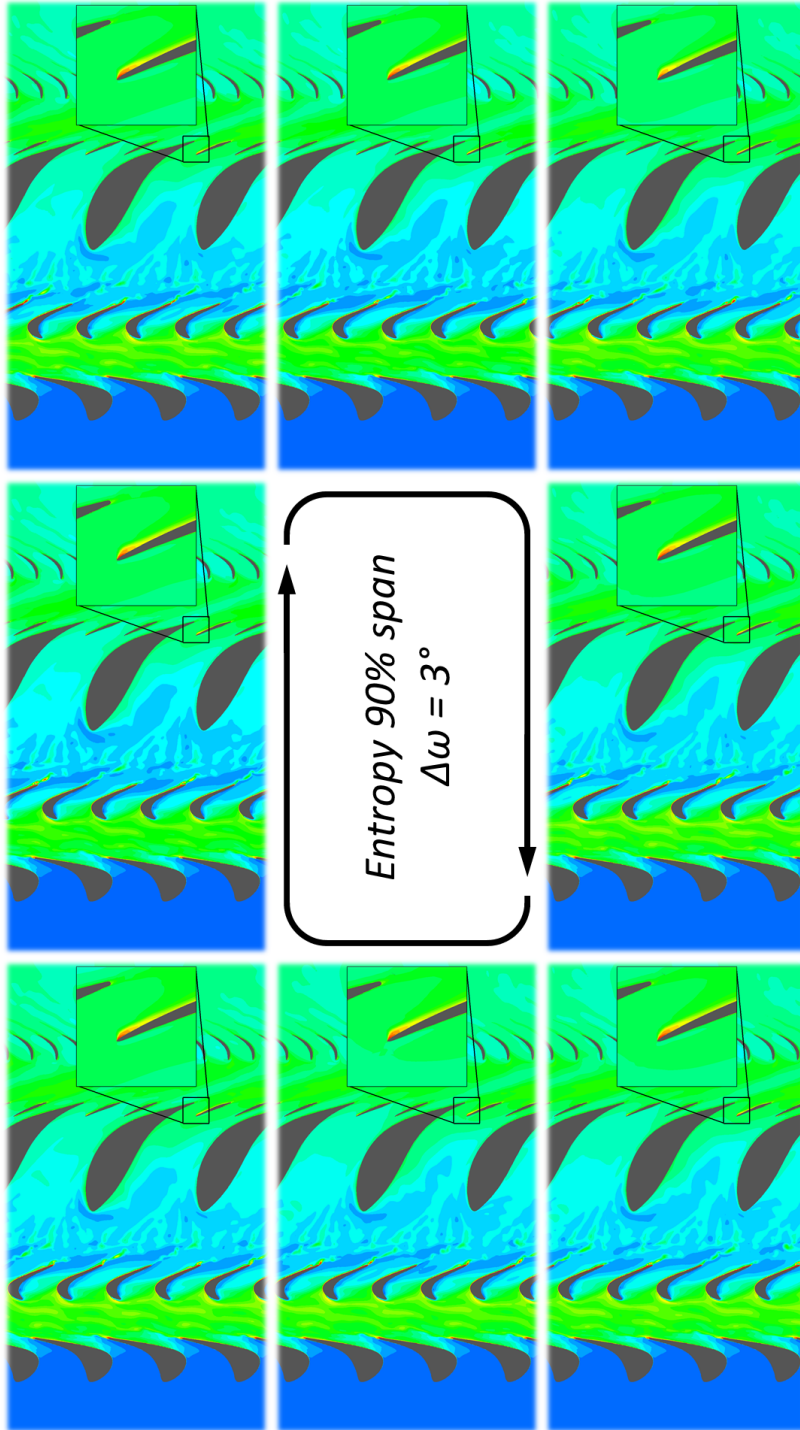
Figure 4.34: Unsteady Blade to Blade contour plots of entropy at 90% span.
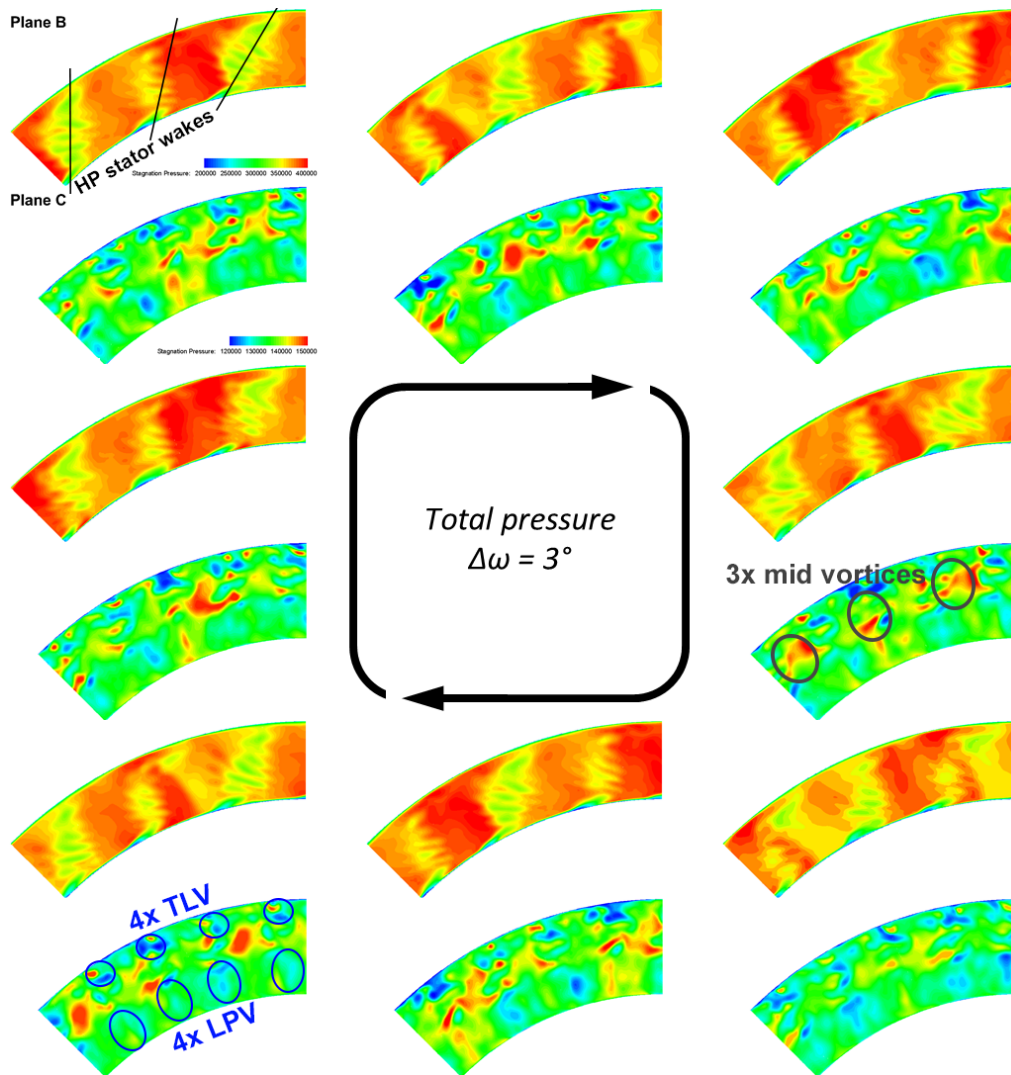
Figure 4.35: Unsteady contour plots at planes B and C of total pressure.
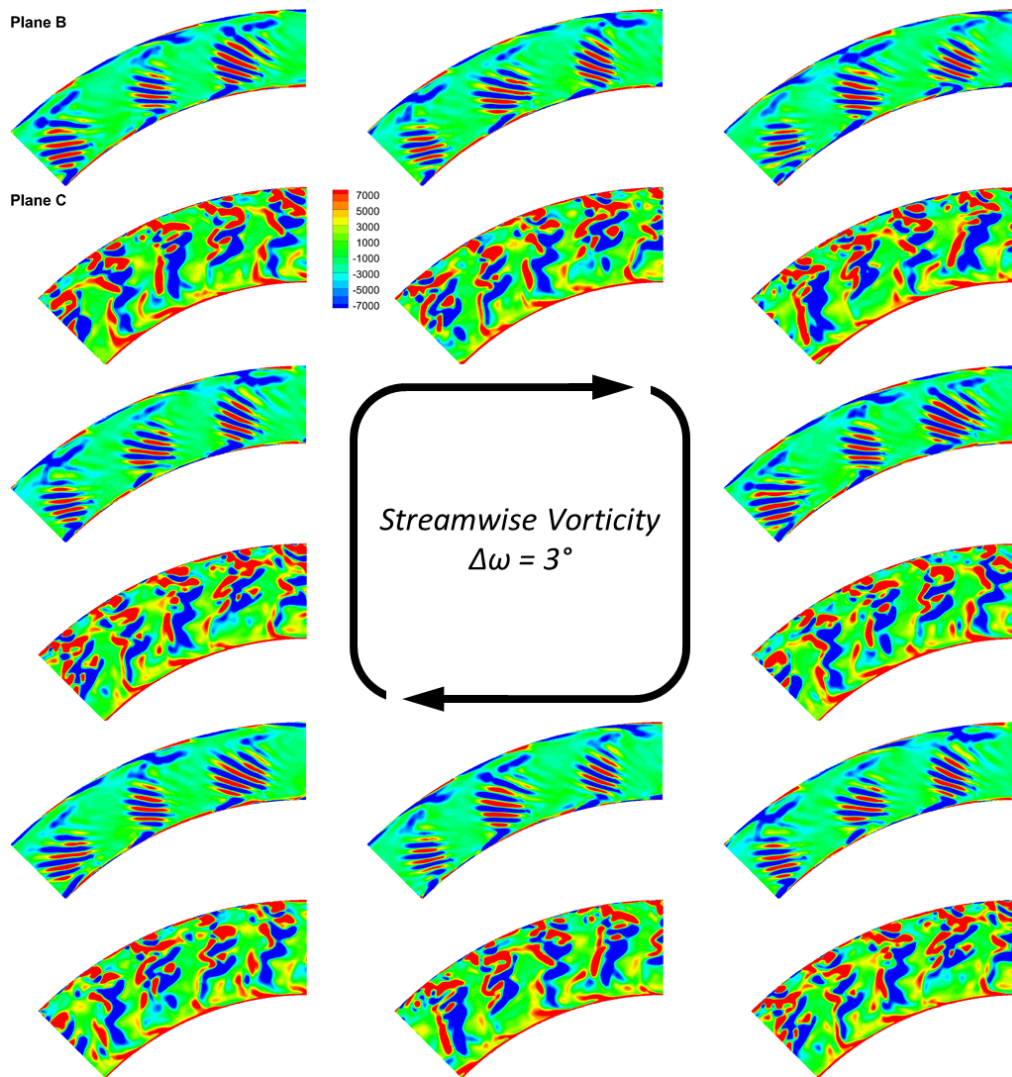
Figure 4.36: Unsteady contour plots at planes B and C of streamwise vorticity.
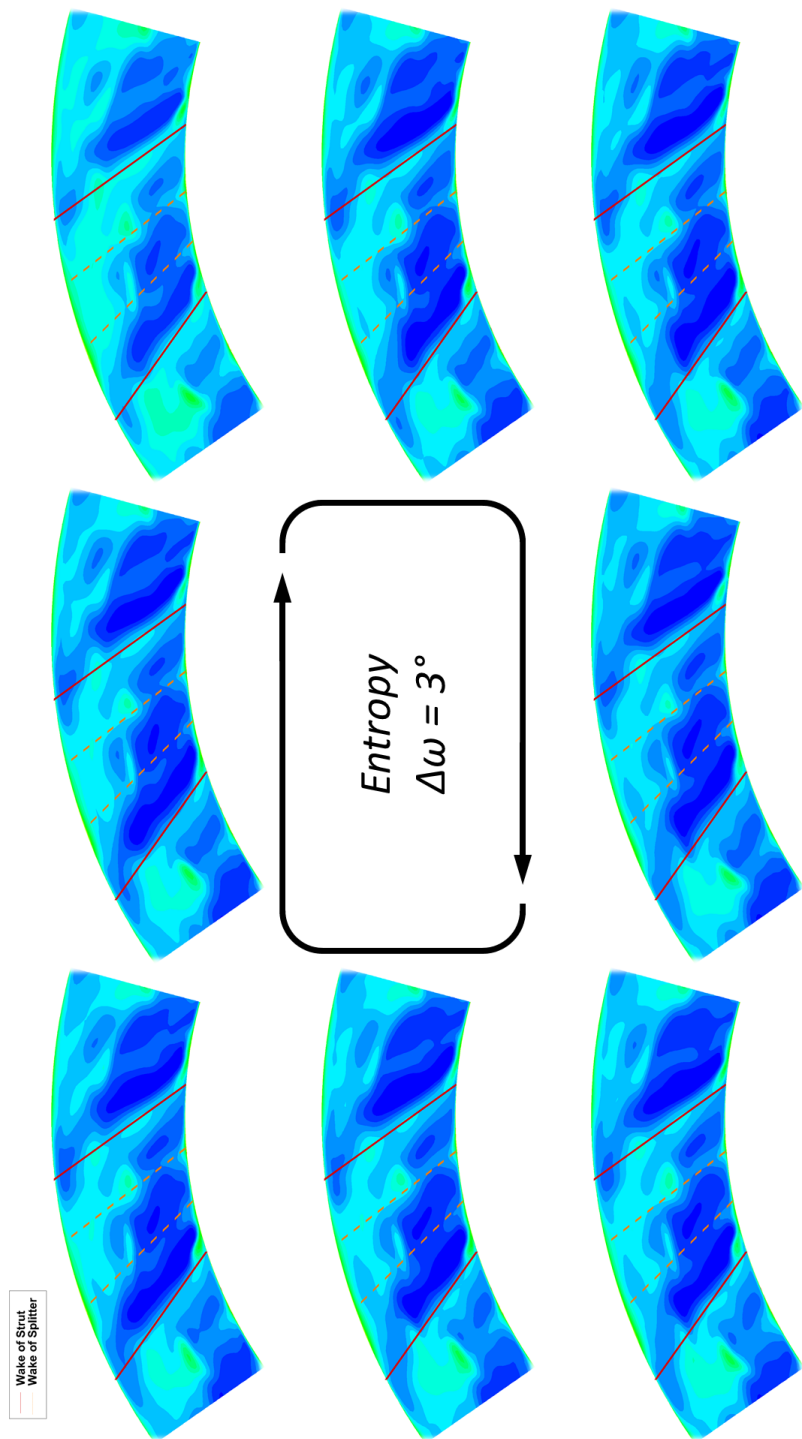
Figure 4.37: Unsteady contour plots at plane E of entropy.
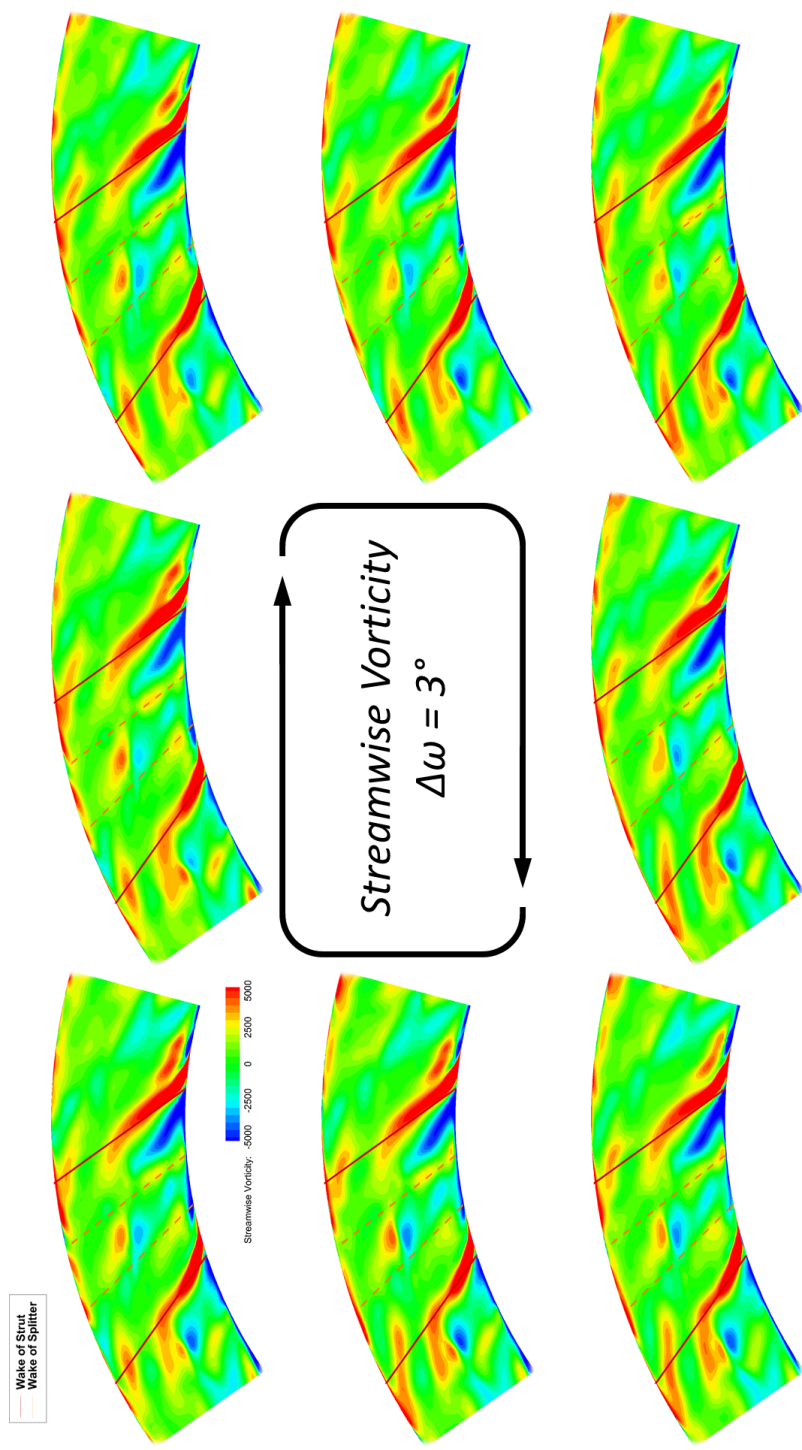
Figure 4.38: Unsteady contour plots at plane E of streamwise vorticity.

CHAPTER 5

Summary And Conclusion

5.1 Summary

The importance of the improvement in efficiency and reduction in noise emission and weight of jet engines is self-evident. Therefore alternative designs such as a **t**urning **m**id **t**urbine **f**rame (TMTF) is discussed in this master thesis are crucial. A numerical simulation was performed to understand, what the flow features through such a design are. To validate the CFD calculation, the computed result was compared to measurement data.

The first step was to find the correct boundary conditions to assure comparability between the simulation and the measurement. The inlet condition for the low pressure stage calculation was taken from the experiment. Thus, it was only necessary to find the right outlet pressure for the calculation by assuring the right strut blade loading.

After finding the best boundary conditions, the simulation was set up for two different CFD codes: Ansys CFX® and Linars. Both codes were used to solve a steady-state simulation of the low pressure stage only and of the whole two-stage turbine rig. The point of interest was the turning mid turbine frame of the rig. An unsteady calculation was also performed by Linars in order to get a time resolved solution. The result of these simulation showed the key flow features as well as important design considerations, which should be taken into account when designing such an TMTF.

Besides the simulation to see the features of the new embedded design, also some key parameters of flow modelling were compared with each other. This comparison shows the impact of a variation of these properties on the flow.

5.2 Conclusion

The flow through a mid turbine frame with turning struts and an S-shaped duct has a high impact on the efficiency of the downstream low pressure rotor. Fluctuations and highly unsteady conditions lead to vibrations at the subsequent blade row, and hence to noise emissions as well as structural stress on the LP blade row. To reduce these negative influences the design with the split blades promises a relatively easy and efficient solution.

The simulation done in this thesis showed, that the target of flow-homogenization was fulfilled by the design. The influence of large vortexes transported from the HP stage as well as the vane passage vortex induced by the TMTF, are homogenized by the splitters and the flow shows less fluctuations. On the other hand, new flow features were developed: smaller lower and upper passage vortices developed by the strut and splitter blades as well as flow separations by the splitters. Also additional wakes are generated by the split blades, which leads to losses as well as higher turbulence behind the duct. An important outcome is also, that endwall shaping to reduce the blockage effect is vital in order to increase the efficiency of the embedded design.

The comparison of some key parameters of the flow showed, that it is important to use the right boundary conditions for the simulation. When the simulation is set up, the simulator should be aware of the influences of such parameters. This is even more important in commercial codes, which automatizes such parameters, where the correctness and applicability should at least be critically questioned.

When comparing the two codes CFX® and LINARS, at first it is important to mention that the Ansys code is a commercial code, which aim is to reach fast convergence and where user friendliness is a major objective. Thus, many switches and triggers are used to run the calculation as stable as possible, with the disadvantage that the solver may get a result although the boundary conditions are not set properly. LINARS on the other hand is a non-commercial, in-house solver without a GUI or other concessions to usability. LINARS is more sensitive on bad input parameters, hence it is more difficult to get a "fast solution". So the disadvantage is that it may take a while to get a stable calculation, but when reaching a solution it is almost certainly a physically meaningful result which fulfils the boundary conditions.

Generally, both codes perform quite similar. Although differences can be observed, the calculations shows nearly the same results. A comparison to measurement results shows, that the simulation picture the reality quite

well.

The unsteady simulation showed that the flow in this two-stage rig is highly fluctuating. The periodic influences of the high pressure rotor as well as the HP stator influence the downstream flow in the TMTF and the low pressure rotor.

List of Figures

List of Tables

Bibliography

[1]   I. C. A. Organization. *State of Global Aviation Safety 2011*. Yearly report. 2011.

[2]   *2011 World Airport Traffic Report*. Airports Council International, 2012.

[3]   U.S. Department of Energy. 2013. URL: http://energy.gov (visited on 28/05/2013).

[4]   International air transport association. 2013. URL: http://www.iata.org (visited on 28/05/2013).

[5]   M. L. Wald. *A Cleaner, Leaner Jet Age Has Arrived*. The New York Times. URL: http://www.nytimes.com/2008/04/09/technology/techspecial/09jets.html (visited on 09/04/2008).

[6]   OpenFlights. OpenFlights. 2013. URL: http://openflights.org (visited on 28/05/2013).

[7]   F. Heitmeir. *Flugantriebe, Vorlesungsskriptum 2013*. Institute for Thermal Turbomachinery and Machine Dynamics, TU Graz. 2013.

[8]   *Are we measuring the right efficiency in aviation?* Asselin, Inc. URL: http://www.asselininc.com/performance/are-we-measuring-the-right-efficiency-in-aviation/ (visited on 22/11/2013).

[9]   J. Dahl. *Diagram of a typical gas turbine jet engine (in English)*. Wikimedia Foundation Inc. URL: http://en.wikipedia.org/wiki/Turbojet (visited on 28/11/2013).

[10]   J. Kurzke. *Fundamental differences between conventional and geared turbofans*. ASME paper GT2009-59745. 2009.

[11]   H. Eichlseder. *Thermodynamik, Vorlesungsskriptum 2010*. Institute for Internal Combustion Engines and Thermodynamics, TU Graz. 2010.

[12]   H. Rietschel. *Raumluftklimatechnik. Band 2: Raumluft- und Raumkühltechnik*. Klaus Fitzner, Springer Berlin Heidelberg New York, 2008.

[13] F. Heitmeir. *Thermische Turbomaschinen - Grundlagen und Vertiefung, Vorlesungsskriptum 2012*. Institute for Thermal Turbomachinery and Machine Dynamics, TU Graz. 2012.

[14] J. F. Seda. *Aircraft engine with inter-turbine engine frame*. Mar. 2004. URL: http://www.freepatentsonline.com/6708482.html.

[15] Pratt and Whitney. Pratt & Whitney. 2013. URL: http://www.pw.utc.com (visited on 06/07/2013).

[16] E. Göttlich. *Research on the aerodynamics of intermediate turbine diffusers*. Progress in Aerospace Sciences 47. 2011.

[17] S. Lavagnoli, T. Yasa, G. Paniagua, L. Castillon and S. Duni. *Aerodynamic Analysis of an Innovative Low Pressure Vane Placed in an S-shaped Duct*. Journal of Turbomachinery, ASME. 2011. 134(1). 13p. 2012.

[18] R. Spataro, E. Göttlich, D. Lengani, C. Faustmann and F. Heitmeir. *Developement of a turning mid turbine frame with embedded design - Part II: Unsteady measurements*. In Proceedings of ASME 2013 Turbo EXPO, June 3-7, 2013, San Antonio Convention Center, San Antonio, Texas, USA. 2013.

[19] R. Spataro, E. Göttlich, D. Lengani, C. Faustmann and F. Heitmeir. *Developement of a turning mid turbine frame with embedded design - Part I: Design and steady measurements*. In Proceedings of ASME 2013 Turbo EXPO, June 3-7, San Antonio Convention Center, San Antonio, Texas, USA. 2013.

[20] P. Bader, W. Sanz, R. Spataro and E. Göttlich. *Flow evolution through a turning mid turbine frame with embedded design for next generation engines*. In Proceedings of ASME 2014 Turbo EXPO, June 16-20. 2014, Düsseldorf, Germany. 2013.

[21] J. Erhard and A. Gehrer. *Design and construction of a transonic test turbine facility*. In proceedings of ASME Turbo Expo 2000, May 8-11, Munich, Germany, GT-48. 2000.

[22] J. Hubinka, C. Santer, B. Paradiso, F. Malzacher and E. Göttlich. *Design and construction of a two shaft test turbine for investigation of mid turbine frame flows*. In Proceedings of ISABE 2009, Montreal, Quebec, Canada, ASME paper No. ISABE-2009-1293. 2009.

[23] J. Hubinkan, B. Paradiso, C. Santer, H. P. Pirker and E. Göttlich. *Design and operation of a two spool high pressure test turbine facility*. In Proceedings of the 9th ETC conference, Istanbul, Turkey. pp 1531-1540. 2011.

[24] R. Spataro, C. Santner, D. Lengani and E. Göttlich. *On the flow evolution through a LP turbine with wide-chord vanes in an S-shaped channel.* In Proceedings of ASME 2012 Turbo EXPO, June 11-15. 2012, Copenhagen, Denmark. 2012.

[25] R. G. Dominy, D. A. Kirkham and A. D. Smith. *Flow Development Through Inter-Turbine Diffusers.* ASME Journal of Turbomachinery 120. p.298-304. 1998.

[26] G. Norris, R. G. Dominy and A. D. Smith. *Flow Instabilities Within a Diffusing Annular S-Shaped Duct.* ASME Paper 99-GT-70. 1999.

[27] F. Wallin, C. Arroyo Osso and G. Johansson. *Experimental and Numerical Investigation of an Aggressive Intermediate Turbine Duct: Part 1 - Flowfield at Design Inlet Conditions.* 26th AIAA Applied Aerodynamics Conference, AIAA-2008-7056. 2008.

[28] C. Arroyo Osso, F. Wallin and G. Johansson. *Experimental and Numerical Investigation of an Aggressive Intermediate turbine duct - Part 2: Flowfield under Off-design Inlet Conditions.* 26th AIAA Applied Aerodynamics Conference, AIAA-2008-7055. 2008.

[29] C. Santner, E. Göttlich, F. Wallin and M. Hoeger. *Experimental Investigation of Turning Mid Turbine Frame designs.* ISABE-2011-1710. 2011.

[30] G. Pullan, J. Denton and E. Curtis. *Improving the Performance of a Turbine with Low Aspect Ratio Stators by Aft-Loading.* Journal of Turbomachinery 128. pp. 492. 2005.

[31] G. Pullan, J. Denton and M. Dunkley. *An Experimental and Computational Study of the Formation of a Streamwise Shed Vortex in a Turbine Stage.* Journal of Turbomachinery 125. pp. 291. 2003.

[32] A. Marn, E. Göttlich, D. Cadrecha and H. P. Pirker. *Shorten the Intermediate Turbine Duct Length by Applying an Integrated Concept.* Journal of Turbomachinery 131. Issue 4. 2009.

[33] R. J. Miller, R. W. Moss, R. W. Ainsworth and N. W. Harvey. *The Effect of an Upstream Turbine on a Low-Aspect Ratio vane.* ASME paper GT2004-54017. 2004.

[34] N. W. Harvey, G. Brennan, D. A. Newman and M. G. Rose. *Improving Turbine Efficiency Using Non-Axisymmetric End Walls: Validation in the Multi-Row Environment and with Low Aspect Ratio Blading.* ASME paper GT-2002-30337. 2002.

[35] F. Wallin and L. E. Ericsson. *Non-axisymmetric Endwall Shape Optimization of an Intermediate Turbine Duct.* 17th ISABE conference, ISABE-2007-1300. 2007.

[36] F. Wallin, S. Ore, F. Malzacher, E. Göttlich and C. Santner. *Design of turning mid turbine frames.* 19th ISABE conference, Göteborg, ISABE-2011-1713. 2011.

[37] R. Schwarze. *CFD-Modellierung: Grundlagen und Anwendungen bei Strömungsprozessen.* Springer Verlag, 2013.

[38] F. R. Lewis. *Weather prediction by numerical process.* Cambridge, The University press, 1922.

[39] B. J. Copeland. *Colossus: The Secrets of Bletchley Park's Codebreaking Computers.* Oxford University Press, 2006.

[40] ANSYS Inc. 2013. URL: `http://www.ansys.com/Products/Simulation+Technology/Fluid+Dynamics/Fluid+Dynamics+Products/ANSYS+CFX` (visited on 14/03/2013).

[41] ANSYS Inc. 2013. URL: `http://www.ansys.com/staticassets/ANSYS/staticassets/resourcelibrary/brochure/ansys-cfx-tech-specs.pdf` (visited on 14/03/2013).

[42] Institute for Thermal Turbomachinery and Machine Dynamics, TU Graz. 2013. URL: `http://ttm.tugraz.at/?seite=facilities/numerical/CFD` (visited on 20/03/2013).

[43] F. R. Menter. *Two-Equation Eddy-Viscosity Turbulence Models for Engineering Applications.* AIAA Journal, vol. 32, no 8. pp. 1598-1605. 1994.

[44] F. R. Menter. *Zonal Two Equation k-omega Turbulence Models for Aerodynamic Flows.* AIAA Paper 93-2906. 1993.

[45] W. Sanz. *Computational Fluid Dynamics, Vorlesungsskriptum 2012, ITTM, TU Graz.* Institute for Thermal Turbomachinery and Machine Dynamics, TU Graz. 2011.

[46] P. R. Spalart and S. R. Allmaras. *A One-Equation Turbulence Model for Aerodynamic Flows.* La Recherche Aerospatiale n 1. 1994.

[47] H. JR. Oertel and E. Laurien. *Numerische Strömungsmechanik.* Vieweg, Braunschweig / Wiesbaden, 2003.

[48] B. Lakshminarayana. *Fluid Dynamics and Heat Transfer of Turbomachinery.* Wiley-Interscience, John Wiley & Sons Inc., 1996.

[49] J. Denton and U. Singh. *Time Marching Methods for Turbomachinery Flow Calculations*. VKI Lecture Series 1979-7, von Karman Institute. 1979.

[50] Jola. *Best practice guidelines for turbomachinery CFD*. CFD Online. URL: http://www.cfd-online.com/Wiki/Best_practice_guidelines_for_turbomachinery_CFD#Frozen_rotor_simulations (visited on 14/11/2013).

[51] *ANSYS CFX-Solver Modelling Guide*. ANSYS. ANSYS Inc., 2010.

[52] M. Giles. *Non-reflecting boundary conditions for Euler equation calculations*. AIAA Journal, Vol. 28, No. 12. 1990.

[53] Nedtheprotist and Materialscientist. *Mixing length model*. Wikimedia Foundation Inc. URL: http://en.wikipedia.org/wiki/Mixing_length_model (visited on 19/08/2013).

[54] Cortana Company. 2013. URL: http://www.cortana.com/Drag_Description.htm (visited on 09/08/2013).

[55] P. Moin and J. Kim. *Tackling Turbulence with Supercomputers, Drag on a Golf Ball*. Stanford University. URL: http://ctr.stanford.edu/articles/tackle_illustration2.html (visited on 14/11/2013).

[56] K.-H. Grote and J. Feldhusen, eds. *DUBBEL: Taschenbuch für den Maschinenbau*. 22nd ed. Springer, 2007.

[57] R. Dominy and D. Kirkham. *The influence of blade wakes on the performance of inter-turbine diffusers*. ASME Journal Turbomachinery 1996. Vol. 118. pp. 347-352. 1996.

[58] R. Dominy and D. Kirkham. *The influence of swirl on the performance of inter-turbine diffusers*. VDI Berichte 1186, 1995. pp. 107-122. 1995.

[59] R. Dominy, D. Kirkham and A. Smith. *Flow development through inter-turbine diffusers*. ASME Journal Turbomachinery 1998. Vol. 120. pp. 298-304. 1998.

[60] G. Norris and R. Dominy. *Diffusion rate influences in inter-turbine diffusers*. IMechE Journal PowerEnergy 1997. Vol. 211 (PartA). pp. 235-242.

[61] G. Norris, R. Dominy and A. Smith. *Flow instability within a diffusing, annular S-shaped duct*. ASME paper 99-GT-70, 1999. 1999.

[62] G. Norris, R. Dominy and A. Smith. *Strut influences within a diffusing annular S-shaped duct*. ASME paper 98-GT-425, 1998. 1998.

[63] R. Spataro, E. Göttlich, C. Santner and F. Heitmeir. *A numerical comparison on the aerodynamic performance of a two-stage two-spool turbine facility predicted by steady and unsteady simulations.* In Proceedings of 10th European Turbomachinery Conference, April 21-25, Lappenranta, Finland, Paper No. 39. 2012.

[64] R. Spataro. „Aerodynamic Design and Investigation of an Embedded Concept for Turning Mid Turbine Frames". PhD thesis. Technical University of Graz, Austria, 2013.

[65] P. Pieringer. *Implementieren von nichtreflektierenden Randbedingungen in Finite-Volumen-Strömungsrechenverfahren.* Diplomarbeit, Technische Universität Graz. 1999.

[66] R. J. Miller, R. W. Moss, R. Ainsworth and N. W. Harvey. *The development of turbine exit flow in a swan-necked inter-stage diffuser.* In Proceedings of ASME Turbo Expo 2003, June 16-19, Atlanta, Georgia, USA, ASME Paper No. GT-2003-38174. 2003.